

## ABSTRACT

Title of Thesis:

THERMAL AND HYDRAULIC  
PERFORMANCE OF SPINE FIN TUBE  
HEAT EXCHANGERS AT LOW  
REYNOLDS NUMBER CONDITIONS

Carlos Herrera, Master of Science, 2017

Directed By:

Research Professor Yunho Hwang, Ph.D.  
Department of Mechanical Engineering

The goal of this work is to present the air-side thermal and hydraulic performance of heat exchangers with spine-fin surface augmentation. Although not as common as plain / plate fin, spine-fin heat exchangers have been used for decades in household refrigeration evaporators and in the outdoor coils of household air-conditioning systems. Of particular interest in this study, was the performance at low air-side Reynolds numbers (500 – 900). Heat transfer coefficients for this geometry were evaluated for samples of varying fin pitch, fin height and tube diameter in both parallel and angled bank arrangements. Water was selected as the hot fluid operating in the turbulent regime with mass flow rates varying at each airflow rate test point. Static cold and hot stream temperatures were maintained for all tests. Air-side heat transfer coefficient (AHTC) is highest for the lower diameter tube heat exchangers and increases in fin pitch lowered the AHTC. This behavior is not seen in plain fin, microchannel and other heat exchangers.

THERMAL AND HYDRAULIC PERFORMANCE OF SPINE FIN TUBE HEAT  
EXCHANGERS AT LOW REYNOLDS NUMBER CONDITIONS

By

Carlos Herrera

Thesis submitted to the Faculty of the Graduate School of the  
University of Maryland, College Park, in partial fulfillment  
Of the requirements for the degree of  
Master of Science  
2017

Advisory Committee:  
Research Professor Yunho Hwang, Chair  
Professor Jungho Kim  
Professor Bao Yang

© Copyright by  
Carlos Herrera  
2017

## **Dedication**

To my wife, best friend and encourager.

## **Acknowledgements**

As with everything worth pursuing, the work completed in this study presented a number of challenges and at times apparently unsurmountable obstacles. Completion of this work could not have been possible without the support and expertise of several individuals.

I would like to thank Dr. Reinhard Radermacher for opening so many doors for me. I believe that the phrase a “gentleman and a scholar” was thought of with him in mind.

My gratitude goes also to Dr. Yunho Hwang. Most of my real understanding of vapor compression cycles is derived from his excellent teaching and insights. This work would have been impossible without his consistent push for excellence and clarity.

The support, advice and insight of my colleague and mentor Dr. Andrea Kelecny were of critical importance. I am also grateful for her wonderful teaching in the area of heat exchanger design.

Most importantly I thank my God for putting so many kind and brilliant people in my path. Thank you Lord.

# Table of Contents

1. Introduction.....	1
1.1. Spine Fin-tube heat exchanger .....	4
1.2. Literature Review .....	7
1.3. Objectives of the Study .....	12
2. Experimental Work .....	14
2.1. Test Facility.....	14
2.1.1. Air flow system .....	15
2.1.2. Water flow system .....	21
2.1.3. Vapor compression system .....	23
2.1.4. Measurements, data acquisition and controls system .....	23
2.2. Test Conditions and Operating Procedure .....	26
2.3. Uncertainty Analysis.....	30
2.3.1. Calculation procedure.....	31
3. Data Reduction.....	36
3.1. Energy Balance.....	36
3.2. Air-side Heat Transfer Performance .....	38
3.2.1. Air-side surface area .....	43
3.2.2. Spine fin-tube hydraulic diameter calculation .....	45
3.3. Water-side Heat Transfer Performance .....	48

3.4. Air-side Pressure Drop.....	49
4. Data Analysis.....	50
4.1. Tube and Fin Pitch Dependence.....	51
4.1.1. Parallel configuration short fin .....	54
4.1.2. Parallel configuration long fin .....	58
4.1.3. Angled configuration short fin .....	61
4.1.4. Angled configuration long fin .....	64
4.2. Fin Length Dependence.....	67
4.2.1. 3/8 inch diameter tube, parallel configuration .....	67
4.2.2. 5/16 inch diameter tube, parallel configuration .....	70
4.2.3. 3/8 inch diameter tube, angled configuration.....	74
4.2.4. 5/16 inch diameter tube, angled configuration.....	77
4.3. Overall Performance .....	80
4.3.1. 7 fpi.....	80
4.3.2. 10 fpi.....	83
4.3.3. 12 fpi.....	86
5. Performance Correlations.....	89
5.1. Correlation Coefficient Summary .....	93
6. Summary .....	94
7. Conclusions and Future Work .....	97

7.1. Conclusions .....	97
7.2. Future Work .....	97
8. References .....	99



## List of Figures

Figure 1: Frost accumulation (left) and calrod (right) on side-by-side plain fin-tube freezer evaporator .....	2
Figure 2: Spine fin-tube evaporator on top freezer refrigerator.....	3
Figure 3: Spine fin-tube fabrication detail .....	4
Figure 4: Fin wrapping around tube .....	5
Figure 5: Air flow direction .....	6
Figure 6: Coil orientation .....	6
Figure 7: Calorimeter schematic.....	14
Figure 8: Calorimeter side view .....	15
Figure 9: VFDs and SCRs in 480 VAC control cabinet.....	16
Figure 10: Evaporator and first revision of duct heater .....	16
Figure 11: Static mixer and active mixing chamber .....	18
Figure 12: Top view unit under test with pressure taps indicated .....	19
Figure 13: Side view and cross section of unit under test.....	19
Figure 14: Outlet static mixer.....	20
Figure 15: Unit under test with contraction and expansion sections .....	20
Figure 16: Volumetric flow chamber .....	21
Figure 17: Mass flow meter, pump, water tank and heater .....	22
Figure 18: Mixing head .....	22
Figure 19: Vapor compression system .....	23
Figure 20: Low voltage (left) and high voltage (right) cabinets .....	24
Figure 21: RTD calibration bath.....	25

Figure 22: Uncertainty propagation table in EES.....	32
Figure 23: Distribution of data for heat load, 10 fpi, 3/8 in tube, short fin.....	35
Figure 24: Energy balance error sources .....	36
Figure 25: Test section top view .....	41
Figure 26: Parallel banks cross section view .....	41
Figure 27: Tubes in duct.....	42
Figure 28: Finned tube segment.....	43
Figure 29: Free flow area normalization .....	45
Figure 30: Flow leakage .....	52
Figure 31: Dimensions detail in samples .....	53
Figure 32: AHTC, parallel banks, short fin.....	55
Figure 33: 5/16 in 7fpi fin-tip to fin-tip gap .....	55
Figure 34: Pressure drop, parallel banks, short fin .....	56
Figure 35: $j$ -factor and $f$ -factor 3/8 in (top) and 5/16 in (bottom) tube, short fin, parallel.....	57
Figure 36: AHTC, parallel banks, long fin .....	58
Figure 37: Pressure drop, parallel banks, long fin .....	59
Figure 38: $j$ -factor and $f$ -factor 3/8 in (top) and 5/16 in (bottom) tube, long fin, parallel.....	60
Figure 39: AHTC, angled banks, short fin.....	61
Figure 40: Pressure drop, angled banks, short fin .....	62
Figure 41: $j$ -factor and $f$ -factor 3/8 in (top) and 5/16 in (bottom) tube, short fin, angled.....	63

Figure 42: AHTC, angled banks, long fin .....	64
Figure 43: Pressure drop, angled banks, long fin .....	65
Figure 44: $j$ -factor and $f$ -factor 3/8 in (top) and 5/16 in (bottom) tube, long fin, angled.....	66
Figure 45: Fin efficiency short Versus Long fin, parallel configuration.....	67
Figure 46: AHTC, parallel banks, short and long fin, 3/8 in .....	68
Figure 47: Pressure drop, parallel banks, short and long fin, 3/8 in.....	68
Figure 48: $j$ -factor and $f$ -factor 3/8 in short (top) and long (bottom) fin, parallel ..	69
Figure 49: AHTC, parallel banks, short and long fin, 5/16 in .....	70
Figure 50: Fin efficiency short Versus Long fin, parallel configuration.....	71
Figure 51: Pressure drop, parallel banks, short and long fin, 5/16 in.....	72
Figure 52: $j$ -factor and $f$ -factor 5/16 in short (top) and long (bottom) fin, parallel	73
Figure 53: AHTC, angled banks, short and long fin, 3/8 in .....	74
Figure 54: Pressure drop, angled banks, short and long fin, 3/8 in.....	75
Figure 55: $j$ -factor and $f$ -factor 3/8 in short (top) and long (bottom) fin, angled ...	76
Figure 56: AHTC, parallel banks, short and long fin, 5/16 in .....	77
Figure 57: Pressure drop, parallel banks, short and long fin, 5/16 in.....	78
Figure 58: $j$ -factor and $f$ -factor 5/16 in short (top) and long (bottom) fin, angled .	79
Figure 59: AHTC, 7 fpi.....	80
Figure 60: Pressure drop, 7 fpi .....	81
Figure 61: 7 fpi $j$ -factor (top) and $f$ -factor (bottom).....	82
Figure 62: AHTC, 10 fpi.....	83
Figure 63: Pressure drop, 10 fpi .....	84

Figure 64: 10 fpi $j$ -factor (top) and $f$ -factor (bottom) .....	85
Figure 65: AHTC, 12 fpi .....	86
Figure 66: Pressure drop, 12 fpi .....	87
Figure 67: 12 fpi $j$ -factor (left) and $f$ -factor (right) .....	88
Figure 68: Colburn $j$ -factor summary based on fin length and bank orientation ..	94
Figure 69: Colburn $j$ -factor summary by fin density .....	95

## List of Tables

Table 1: Summary of fin types in literature review .....	11
Table 2: NI modules list and usage .....	25
Table 3: Test geometric variables.....	26
Table 4: Sample Test conditions .....	27
Table 5: Randomized test sequence parameters .....	29
Table 6: Instrument uncertainties .....	31
Table 7: Uncertainty output example EES .....	33
Table 8: Sample calculated error values .....	34
Table 9: Typical heat load and energy balance values.....	37
Table 10: Sample dimensions 3/8 in and 5/16 in .....	53
Table 11: Regression summary, parallel coils .....	90
Table 12: Regression summary, angled coils.....	90
Table 13: Best fit, regression.....	91
Table 14: Worst fit, regression.....	92
Table 15: Coefficient summary .....	93

## List of Abbreviations

$A$	Area [ $\text{m}^2$ ]
$AHTC$	Air-side Heat Transfer Coefficient [ $\text{W}/\text{m}^2\text{-K}$ ]
$\beta$	Systematic error
$\dot{C}$	Heat capacity [ $\text{W}/\text{K}$ ]
$\varepsilon$	Effectiveness
$\epsilon$	Random error
$f$	Fin
$h$	Heat transfer coefficient [ $\text{W}/\text{m}^2\text{-K}$ ]
$k$	Thermal conductivity [ $\text{W}/\text{m-K}$ ]
$L$	Length [ $\text{m}$ ]
$m$	Fin parameter [ $1/\text{m}$ ]
$N$	Number
$\eta$	Efficiency
$NTU$	Number of Transfer Units
$PI$	Proportional Integral control
$PID$	Proportional Integral Derivative control
$Q$	Heat load [ $\text{W}$ ]
$R$	Thermal resistance [ $\text{K}/\text{W}$ ]
$r$	Radius [ $\text{m}$ ]
$RSS$	Root Sum of Squares
$RTD$	Resistive Temperature Device

$s$	Measurement error
$SCR$	Silicone Controlled Rectifier
$TC$	Thermocouple
$U$	Overall heat transfer coefficient [W/m <sup>2</sup> -K]
$u$	Measurement uncertainty
$v$	Volume [m <sup>3</sup> ]
$UA$	Overall conductance [W/K]
$x$	Spacing between helix turns [m]

## Subscripts

$a$	Air
$by$	Bypass
$ch$	Characteristic
$f$	Finned
$fr$	Frontal, used in face area
$free$	Free flow
$i$	Inside
$o$	Outside
$r$	Ratio
$s$	Surface
$sp$	Spine, used in area projection into airflow
$T$	Total
$t$	Tube
$w$	Water
$w$	Width [m]

## Greek

$\alpha$	Surface area to heat exchanger volume ratio
$\sigma$	Free flow to frontal area ratio



# 1. Introduction

The goal of any heat exchanger manufacturer is to have a product that meets targets for performance, reliability and cost. This is particularly true in household refrigeration. The quality of food items is very dependent on controlled temperature zones within the refrigerator and in the performance of the freezer compartment. Reliability is particularly important in a system that will easily see more than two decades of continuous service in the home. In terms of cost, fierce competition between manufacturers drives a constant search for lower cost materials, more economic designs and manufacturing processes.

All but one of all household refrigeration manufactures uses plain fin-tube heat exchangers. The wide spread use of plain fin-tube heat exchangers, has promoted a lot of optimization work in terms of tube diameter, tube thickness and fin thickness.

Plain fin-tube heat exchangers do well in terms of frost tolerance and frost management. Fins are easily spaced at lower fin densities at the heat exchanger inlet in order to avoid frost accumulation and the resulting increase in pressure drop.

Defrosting of evaporators is most commonly done with heater elements. The continuous nature of the fins in plain fin-tube heat exchangers allow for defrosting of the coil through conduction as well as convection. It is because of this, that defrosting for plain fin-tube heat exchangers is done with tubular heating elements “Calrods”, as seen in Figure 1.



**Figure 1: Frost accumulation (left) and calrod (right) on side-by-side plain fin-tube freezer evaporator**

Plain fin-tube heat exchangers have been studied extensively and there are many published works examining the air-side thermal and hydraulic performance of this geometry; conversely spine fin-tube heat exchangers are only used in the United States by one household refrigerator appliance manufacturer at the time of this study. This almost exclusive use has kept the spine fin-tube heat exchanger from being the target of studies that would improve the design and lower production costs to the extent seen by the plain fin-tube heat exchanger.

Unlike plain fin-tube heat exchangers, the manufacturing process for spine fin-tube prevents the current designs from allowing the manufacturer to control fin pitch. Unlike in plain fin-tube, spine fin-tube heat exchangers manage frost accumulation at the inlet by increasing the face area of the heat exchangers while maintaining fin density constant on the tubes. One way this is

accomplished is by creating an “A-coil” geometry in which the base of the triangle is the air inlet and the apex is the outlet. The apex tight geometry prevents air-bypass. Defrosting in these systems is typically accomplished via radiation and convective heat transfer with the use of a metal wire element covered with a quartz cylinder. The heaters are mounted horizontally between the bottom tubes of the heat exchanger. This practice has two effects; minimizing heating coil sag and reducing bypass at the heat exchanger inlet. The operating temperatures for these heaters are between 1300 to 1800°F for the coil while the quartz tube is about 1200°F, ASHRAE (2008). While these heaters are susceptible to vibration and impact damage they do well with thermal shock and the exposure to water that comes with the defrost process. Efficiency for these types of heaters is above 80%, ASHRAE (2008).

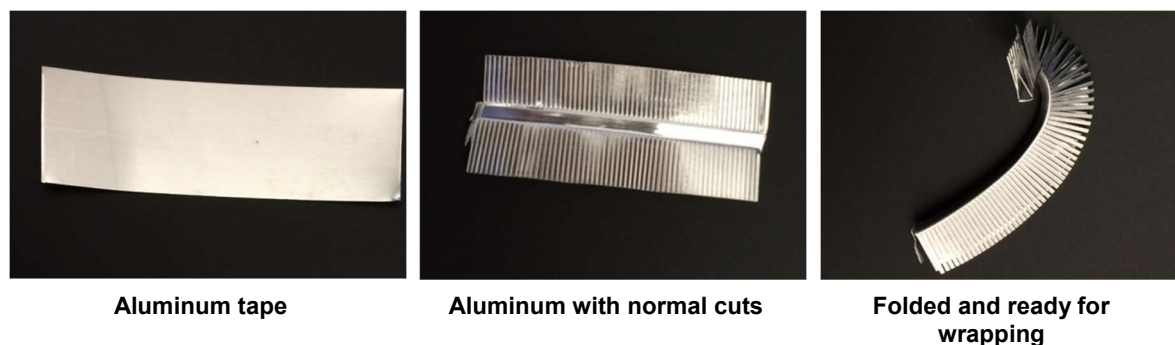


**Figure 2: Spine fin-tube evaporator on top freezer refrigerator**

## 1.1. Spine Fin-tube heat exchanger

Spine fin-tube heat exchangers such as the one in Figure 2 are made from a continuous length of finned tube where the fins are formed from a thin strip of aluminum that is cut in the direction normal to its edges and then folded in half, along its length. The resulting u-shaped strip is helically wound along the length of a tube; Figure 3 shows three different steps in the manufacturing process.

Fin pitch is set by controlling the speed of the tube feed as it moves through the fin wrapping machine, a view of the spine fin machine is shown in Figure 4 . Fin height and thickness are a function of the dimensions of the aluminum strip used in the fin production process. The thickness of the material and the width of the material are of importance in terms of thermal performance as they will drive fin efficiency. But the main consideration is cost; a thicker and wider aluminum ribbon will increase the price of a heat exchanger assembly.

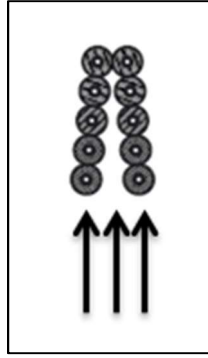


**Figure 3: Spine fin-tube fabrication detail**

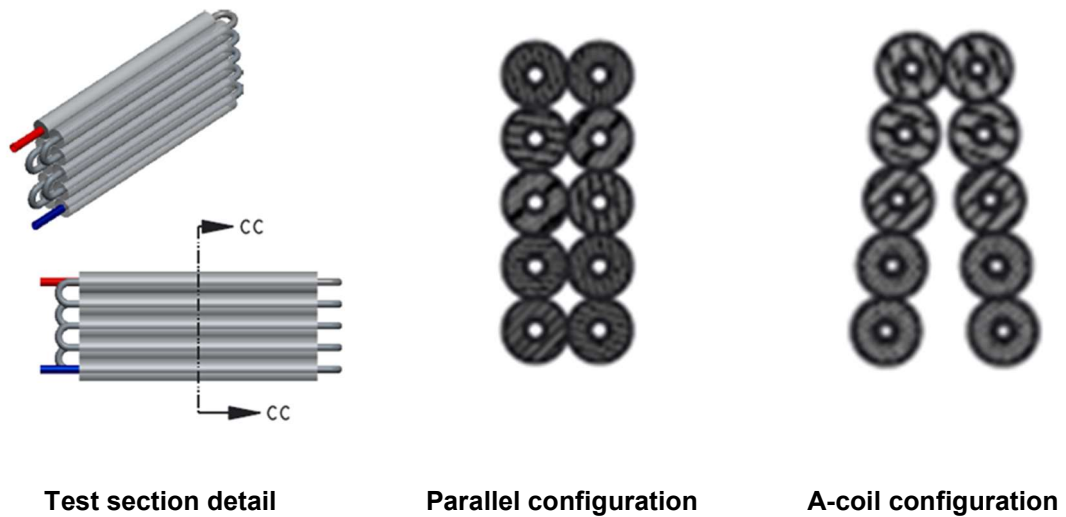


**Figure 4: Fin wrapping around tube**

Tubes, like in all heat exchangers, can be arranged in a variety of ways with respect to the direction of the incoming airflow. However, in household refrigeration applications the flow of air into the heat exchanger does not occur through the largest face of the heat exchanger but rather through the bottom face of the coil as seen in Figure 5. As mentioned previously, in application, air-side blockage due to frost accumulation on the face of the coil is managed by opening the banks of coils so there is more face area to accumulate frost and avoid a complete blockage on the first tubes on the face of the coil. Therefore, performance in this study is evaluated with parallel bank coils and coils with an inscribed angle with flow in the direction shown in Figure 5 and Figure 6.



**Figure 5: Air flow direction**



**Figure 6: Coil orientation**

Additional details on the geometry of the coils as well as the different geometric parameters used in the different calculations are given in section 3.2.1.

## 1.2. Literature Review

Perhaps due to its non-mainstream use, spine fin-tube has not been widely studied. Holtzapple and Carranza (1990) presented a correlation for “Spined Pipe” in cross flow. The spine fin geometry was an integral part of the pipe itself. The fin material was shaved from the surface of the pipe and the fin cross section was pyramidal instead of rectangular, as in the case of the spine fin-tube. This study was divided into two parts. Part one dealt with the pressure drop study and the definition of a hydraulic diameter. Part two was focused on the heat transfer performance. Two features of interest in the tests performed by Holtzapple and Carranza were that only one bank of tubes was tested and that it was tested in perfect cross-flow. These selections ensured a Log-Mean temperature correction factor of unity since it can be reasonably assumed that there was negligible heating of the air as it passed over the heat exchanger bank. Second, there were no parallel or counter-flow effects. In contrast, in the tests samples evaluated in the present study there was substantial heating of the air as it moved through the heat exchanger core. Additionally, there was a counter/cross-flow combination due to the circuitry of the heat exchangers. These characteristics had an impact on air-side heat transfer coefficient (AHTC) calculations that will be discussed in the analysis portion of this study.

Comparison of the thermal performance of single samples of plain fin-tube heat exchangers from different manufacturers and spine fin-tube from General Electric was completed by Lee et al. (2002). Since only one sample was evaluated, the effect of fin density, tube diameter and fin length cannot be discerned. The

authors proposed a Nusselt number correlation for each of the three heat exchanger types tested. Their test showed that the air-side heat transfer performance of the spine fin-tube heat exchanger was higher than that of the plain fin-tube samples under dry conditions. A similar exercise was carried out by Davis et al. (1996) for the purposes of developing a facility to evaluate thermal performance of heat exchangers. Their results also showed that the performance of the spine fin-tube samples was higher than that of the plain fin-tube. The UA of the spine fin-tube was about twice that of the plain fin-tube.

Another integral spine fin-tube was evaluated by Kedzierski and Kim (1994). However, the geometry was housed within an annulus and liquid flows were the focus of the study.

An experimental evaluation of the thermal and hydraulic performance of serrated-fin surface augmentation was performed by Naess (2010). Helically wound serrated fins are commonly used in heat recovery applications from high temperature flue gases. The author speculated that the reduction in surface area seen in serrated fins when compared to helically wound solid fin geometries should be offset by the increase in AHTC seen from the disruption of the air boundary layer due to the cut geometry of serrated fins. This disruption could potentially also produce better flow penetration to the fin base. The author proposed a correlation for Nusselt number where the constant  $C_1$  was established by regression analysis fitting the data to an equation of the form shown in equation (1).



$$Nu = C_1 Re^n Pr^{1/3} \quad (1)$$

The constant  $n$  for the Reynolds number ( $Re$ ) was empirically selected from a range of generally accepted values in the range of 0.63 to 0.68.

The experimental data showed that increasing fin pitch reduced AHTC. Increases in fin height, increased ATHC.

Kawaguchi et al. (2005) compared the thermal performance of spiral and serrated fins used in thermal power generation and proposed equations for each. The two geometries were made from a continuous rectangular section of fin material that was welded to the tube by high-frequency resistance welding. The tube samples were arranged in staggered geometry. Airflow velocities tested were in the 5 – 35 m/s range which is more than 30 times higher than what is seen in household refrigeration applications. Test data showed that the serrated samples had a higher thermal performance than the solid fin. Their explanation matches that proposed by Naess (2010), suggesting that the serrated fin tubes restrict the growth of the temperature boundary layer and that the generated turbulence around the tubes enhances heat transfer. Unlike Naess (2010), their results show that increasing the fin pitch increases AHTC. Kawaguchi also reported that AHTC gains after increases in fin pitch were comparatively lower on serrated fins reasoning that smaller fin pitch restricted flow through the fin-to-fin gap due to the generated turbulence. In the spiral, solid fin, it has the effect of restricting the growth of the temperature boundary layer. The author proposed a Nusselt ( $Nu$ ) number correlation of the form shown in equation (2).


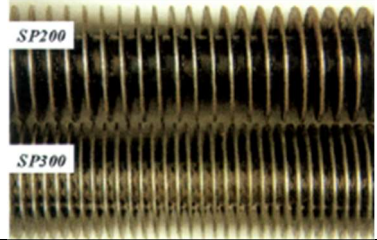

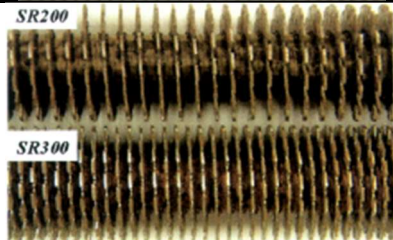
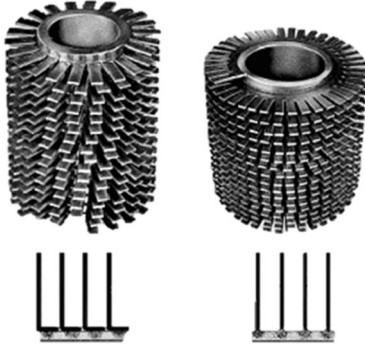
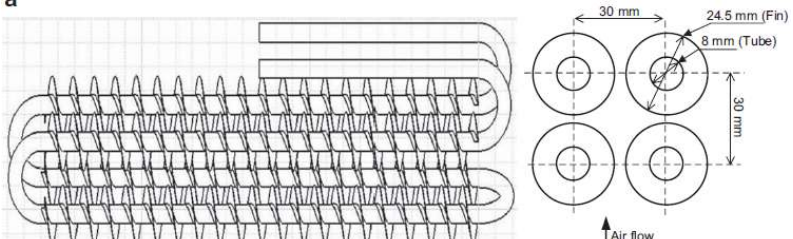


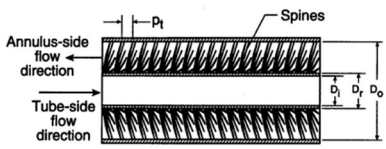
$$Nu = C_1 Re^n Pr^{1/3} \left( \frac{s_f}{d_v} \right)^{-0.0620} \quad (2)$$

Where  $s_f$  is fin gap (mm) and  $d_v$  is equivalent diameter in volume (mm) and the constant  $n$  for the Reynolds number ( $Re$ ) was empirically selected as 0.787 and 0.784 for spiral and serrated fin tubes respectively.

Mooyeon et al. (2010) investigated the air-side performance of “spiral-type circular fin-tube” heat exchangers for use in household refrigerators. The samples investigated varied in fin pitch, number of tube rows, and fin alignment. Two empirical correlations were presented for the inline and staggered fin alignment versions as a function of Reynolds number and number of tube rows and fin pitch normalized by hydraulic diameter.

Table 1 presents a summary of fin types in the literature referenced in this section. Absent from the table is the three sided pyramidal fin of equilateral sides studied by Holtzapple and Carranza (1990).

**Table 1: Summary of fin types in literature review**

Fin Type	Study	Picture	
Spiral	Kawaguchi et al. (2005)		
Serrated	Kawaguchi et al. (2005)		
Serrated	Naess (2010)		
Spiral	Mooyeon et al. (2010)		
Spine	Lee et al. (2002)		
Spine	Kedzierski et al. (1994)		

### 1.3. Objectives of the Study

As with any compact heat exchanger, performance in spine fin-tube heat exchangers is limited by the air-side. It was then the goal of this study to test, analyze and document the thermal and hydraulic performance of spine fin-tube heat exchangers. Pressure drop was of secondary importance in the context of household refrigerators. In household refrigerators the system airflow resistance is dominated by the ducting, diffusers and other ancillary components in the system. The heat exchanger's contribution to pressure drop in the system is so low that in certain instances it is difficult to measure.

Another goal was to provide a heat exchanger calorimeter that could be used on a regular basis to test the thermal performance of different heat exchangers and in benchmarking. The system had to use a fluid that would be easy to work with and environmentally friendly. Avoidance of refrigerant recovery between tests was a priority. Because the system would be running on an almost continuous basis, system reliability and durability were also important.

In the experiments that were run, water-side heat transfer coefficient in the case of the 3/8 in finned tube for example, ranged between 5,600 - 6,300 W/m<sup>2</sup>-K and air-side heat transfer coefficient was about 54 W/m<sup>2</sup>-K at the highest air velocities. The water-side heat transfer coefficient is about 2 orders of magnitude higher than the air-side heat transfer coefficient. In real world application, refrigerant-side heat transfer coefficient is at least an order of magnitude higher than the air-side heat transfer coefficient. Therefore, air is the dominant resistance to heat transfer. Air-side is the main concern in terms of

heat transfer performance. It is also noted that all these experiments are in forced convection air-flow. In other words, it is assumed that the direction of heat-flow is not of primary importance. The tube-side fluid was chosen to meet usability and durability requirements and its flow regime selected to ensure accuracy in the convective heat transfer calculation.

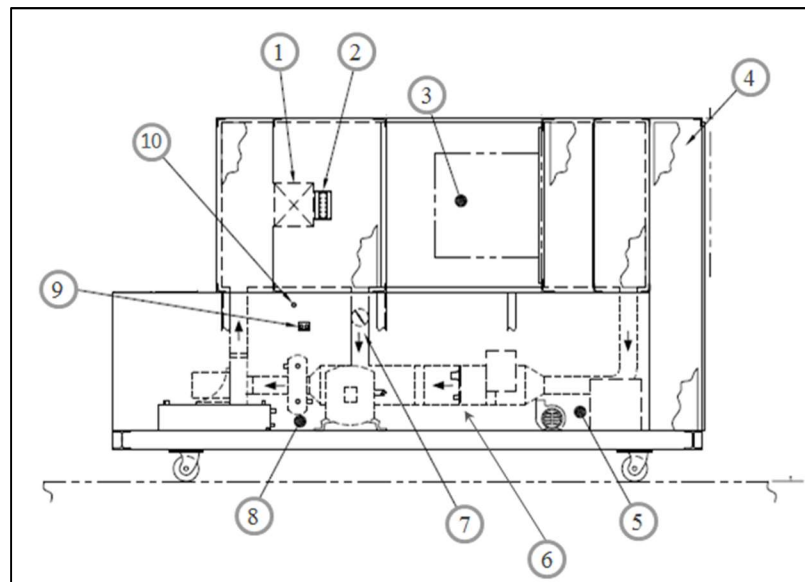
Water was selected as the hot fluid in the experiments. Ethylene and propylene glycol were considered initially, but their high viscosities created very high pressure drops that were detrimental to the calorimeter fluid pump and made it difficult to run the water-side in the turbulent regime.

Each heat exchanger configuration was tested at five different air velocities that were in the range of operation of a household refrigerator, 0.5-1.4 m/s, 500-900 Reynolds number. Each of these air velocity points was tested at five different water mass flows, all high enough to ensure Reynolds numbers upwards of 10,000 on the water-side. While spine fin-tube heat exchangers are used as evaporators they were tested as condensers, that is the hot fluid is the water, kept at a constant temperature of 57°C. This temperature kept water viscosity low in order to reduce water-side pressure drop and keep Reynolds number high. Air inlet temperature was kept constant at 10°C. This air inlet temperature provided a good temperature drop across the heat exchanger.

## 2. Experimental Work

### 2.1. Test Facility

The heat exchanger calorimeter built for this experiment has four main subsystems; an air flow system, a water flow system, a cooling system and a measurement, data acquisition and controls system. The cooling system is based on a vapor compression cycle that provides refrigeration for air and water systems. The system is shown in Figure 7. A side view of the calorimeter is shown in Figure 8. Their operation is described below.



1 Air-side evaporator	6 Air flow nozzle array
2 Air-side heater	7 Air by-pass control valve
3 Unit under test	8 Centrifugal blower
4 Electrical/Controls enclosure	9 Liquid-side brazed-plate evaporator
5 Water pump and tank-heater assembly	10 Electronic expansion valves

**Figure 7: Calorimeter schematic**

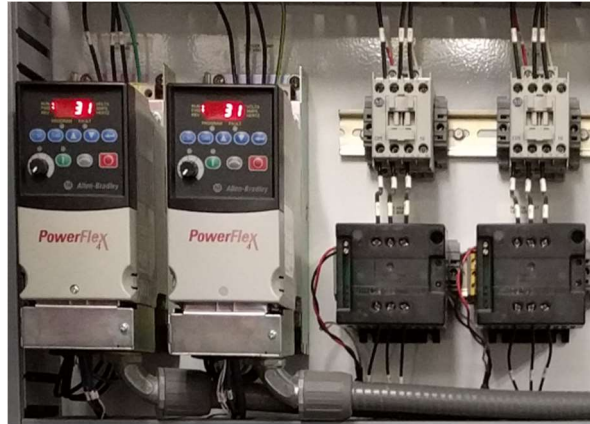


**Figure 8: Calorimeter side view**

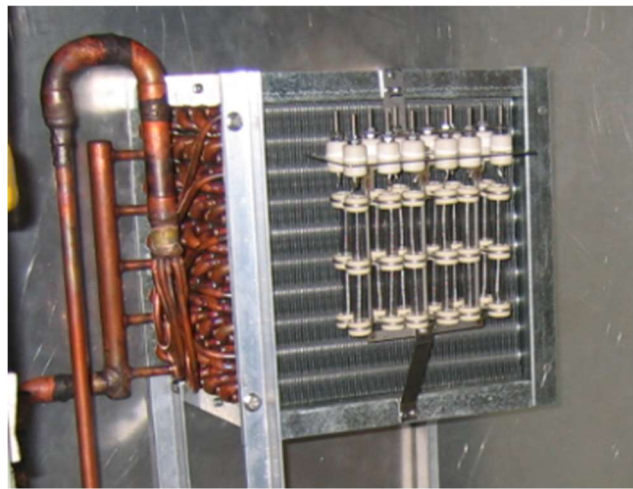
#### 2.1.1. Air flow system

The airflow system is a closed loop in which air is moved by a centrifugal blower. The blower is controlled by a variable frequency drive (VFD), see Figure 9.

The air from the blower moves through a large plain fin-tube heat exchanger that cools the air in the system. This is a large heat exchanger with a volume of  $0.028 \text{ m}^3$  ( $1\text{ft}^3$ ), see Figure 10. Refrigerant flow from the vapor compression system into this heat exchanger is controlled by a stepper motor based expansion valve.



**Figure 9: VFDs and SCRs in 480 VAC control cabinet**



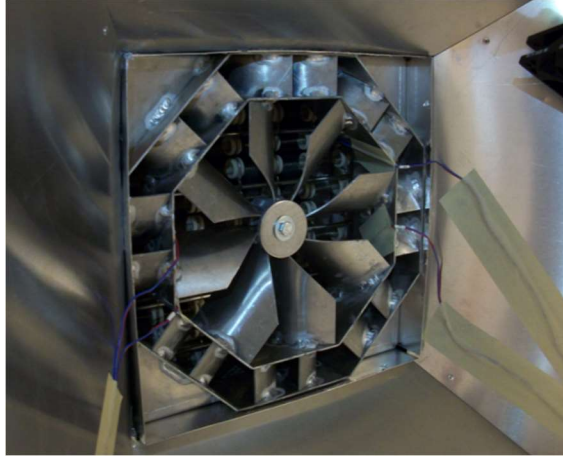
**Figure 10: Evaporator and first revision of duct heater**

In order to be able to handle testing of different heat exchanger capacity ranges two expansion valves piped in parallel were installed (one and two ton capacity each). For the experiments conducted in this study the one ton valve was exclusively used. The unused valve was left closed and with no input signal.



Mounted immediately after the heat exchanger was a 480 VAC, 3 kW exposed coil duct heater, Figure 10. Power to this heater was delivered via a silicon controlled rectifier (SCR) power controller, see Figure 9. Due to the low flows at which the system operates, temperature stratification of the flow became a persistent issue. To correct it and provide the heat exchanger under test an even inlet air temperature profile, a series of perforations, static mixers and mixing fans were positioned after the evaporator and heating assemblies described previously. Air moved through a static mixer after going through the evaporator and heater. Four small DC fans provided additional mixing immediately after the static mixer. The pressure front of the flow was then equalized with a perforation before moving into an inlet contraction before the unit under test. Figure 11 shows the static mixer and part of one of the mixing fans at the top right corner. An even pressure front with reduced turbulence was generated once the flow went through the two sets of perforations following the fans. The final revision of the duct heater can be seen behind the static mixer in Figure 11. The original heater was replaced with one that matched the face area of the evaporator.

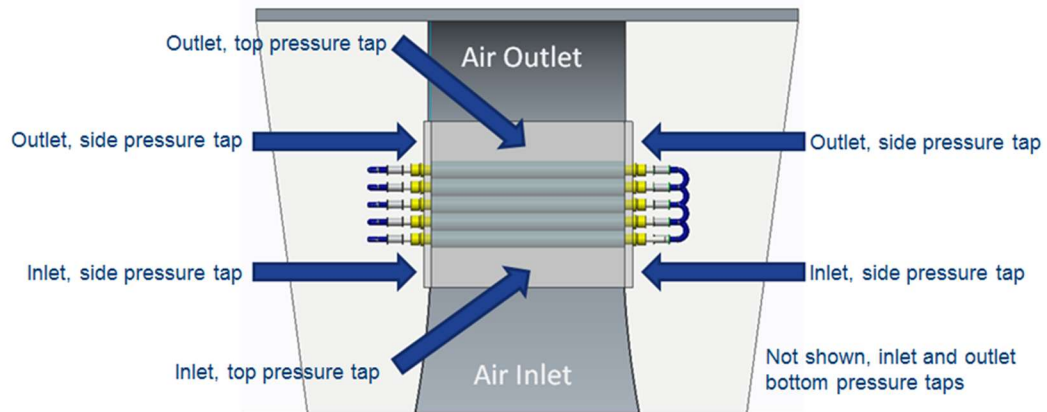
Once the air went through the perforations it moved into a contraction that matched the test section face area at its outlet. This contraction also held four Resistance Temperature Detectors (RTDs) and one relative humidity measurement probe.



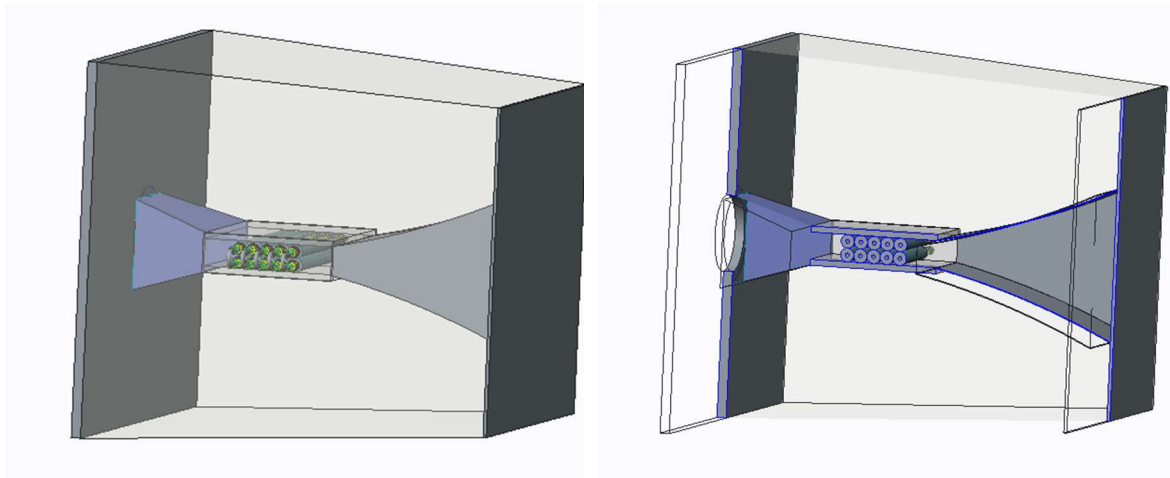
**Figure 11: Static mixer and active mixing chamber**

These sensors measured and provided the process variable for the inlet air temperature control. Located on each test section were four inlet and four outlet pressure tap orifices that were connected to the high and low ports of a differential pressure transducer. This transducer was used to measure air-side pressure drop across the heat exchanger under test. Figure 12 shows the location of the pressure taps on the heat exchanger under test.

Both the inlet contraction and the outlet expansion were sized based on visual experiments conducted with prototype geometries outfitted with clear polycarbonate sides. The flow was visualized with a neutrally buoyant helium bubble generator. The angles for the contraction and expansion were adjusted and dimensions finalized based on the experiment that yielded the lowest number of flow eddies on the walls of the contraction and expansion. The flows were maintained at the range of interest with the use of a volumetric air-flow measurement chamber. Figure 13 presents a view of the full heat exchanger and expansion/contraction assembly on the left and its cross-section on the right.

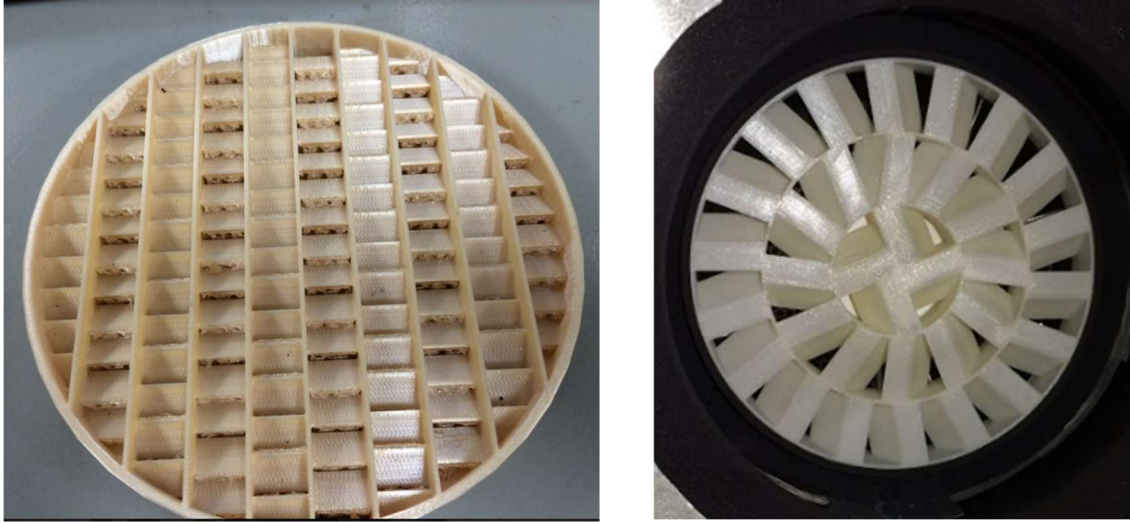


**Figure 12: Top view unit under test with pressure taps indicated**



**Figure 13: Side view and cross section of unit under test**

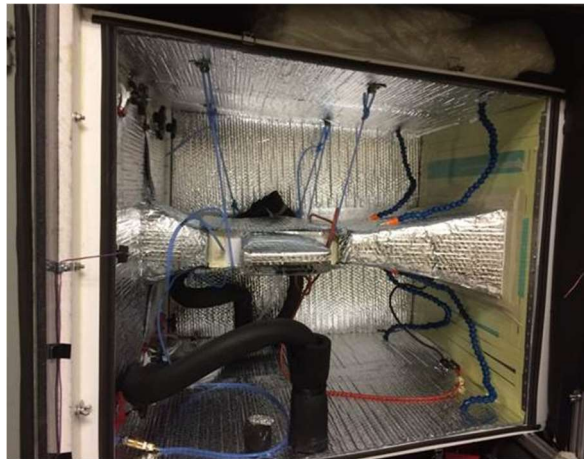
The outlet of the heat exchanger under test is connected to an expansion that is connected to an outlet static mixer. The outlet static mixer was designed based on ASHRAE (1992) and printed on a FDM machine. A view of the mixer with residual support material can be seen in Figure 14, left image. A previous revision of the static mixer based on another model from ASHRAE (1992) showed to be less effective at mixing the outlet air stream, see right side of Figure 14.



**Figure 14: Outlet static mixer**

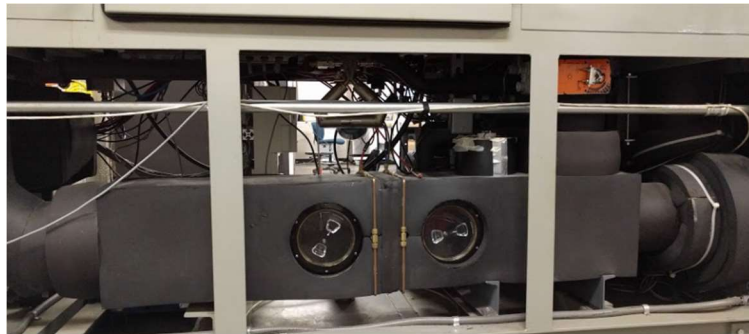
Outlet air temperature was measured with eight RTDs installed radially, immediately after the outlet static air mixer.

Figure 15 shows the unit under test with the inlet RTDs, relative humidity sensor, and pressure taps tubing. It also shows the insulation used to reduce heat losses due to radiation.



**Figure 15: Unit under test with contraction and expansion sections**

Following the unit under test, air moved to a square cross-section air flow chamber where the volumetric flow was measured based on pressure drop across a nozzle or combination of nozzles, see Figure 16. Relative humidity and temperature of the air into the nozzles was also measured here. Air was forced through the system by a centrifugal blower run by a 3-phase motor that was controlled by a VFD. This blower can be seen to the right side of Figure 16.

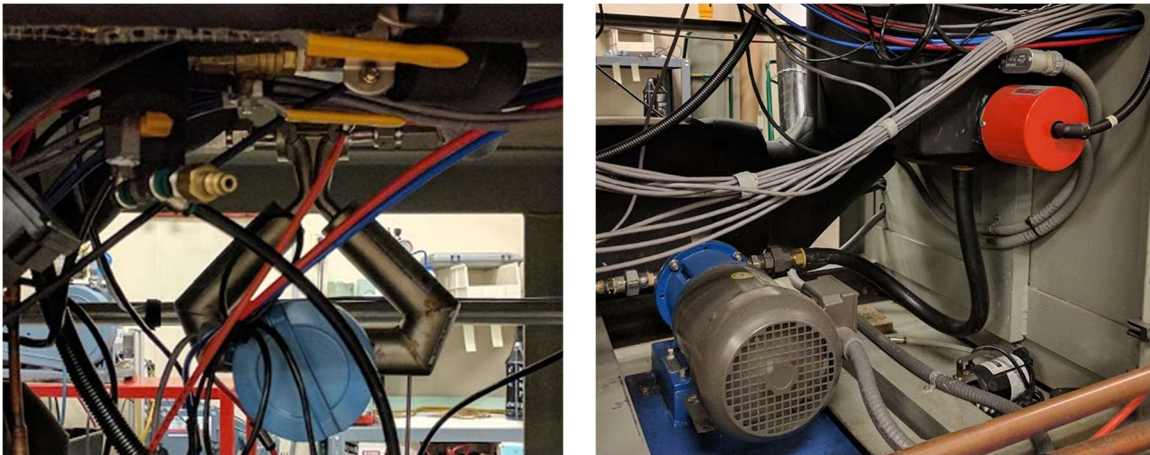


**Figure 16: Volumetric flow chamber**

### 2.1.2. Water flow system

Water was the hot fluid in all calculations in the heat exchanger calorimeter. Water treated with corrosion and bacteria inhibitor was stored in an open to atmosphere tank. A 480 VAC, 3 kW immersion heater was installed in this tank, see Figure 17, right picture. Power to the heater was delivered via a SCR power controller. Water was moved through the system by a magnetic drive-stainless steel pump with a three-phase motor controlled via a VFD. Water was moved through a high temperature filter before moving into a brazed plate heat exchanger that provided cooling for the water system. The cold fluid in this heat exchanger was R404A from the vapor compression subsystem. A second,

stepper motor controlled, expansion valve regulated flow of refrigerant through the brazed plate heat exchanger. Water then moved to a very precise Coriolis effect mass flow meter before going into a mixing head mounted at the inlet to the heat exchanger, see Figure 17 left picture. A mixing head was also installed at the outlet of the heat exchanger under test. Both mixing heads held two RTDs. Figure 18 shows the inlet head. The outlet head is a copy of the inlet head.



**Figure 17: Mass flow meter, pump, water tank and heater**



**Figure 18: Mixing head**



### 2.1.3. Vapor compression system

A R404A vapor compression system was used as the source of cooling for both the water and air subsystems. It was merely a support system; the working fluid for the heat exchangers under test was water. The R404A system ran on a bypass loop until either air or water subsystems required cooling. Flow into each system was controlled via stepper motor electronic expansion valves. The system's shell and tube condenser used tower water to manage the waste heat, see bottom right of Figure 19.



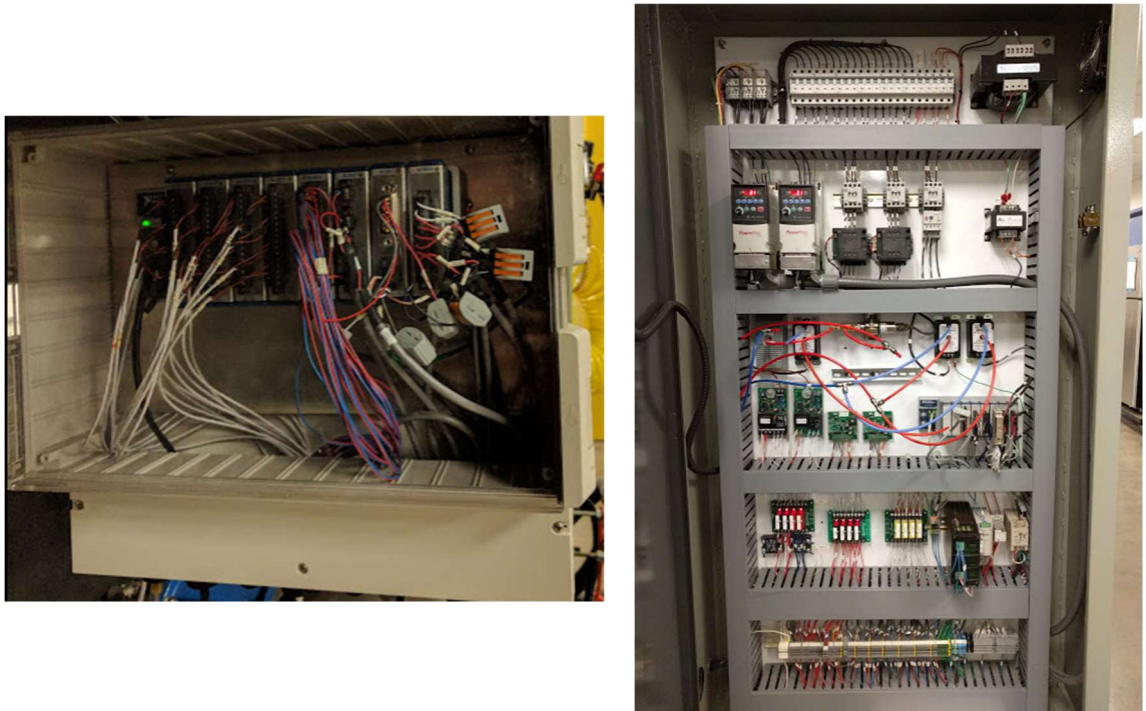
**Figure 19: Vapor compression system**

### 2.1.4. Measurements, data acquisition and controls system

The program that ran the system was written in LabView. Six individual PI control loops ran the air cooling/heating, air flow, water flow and water cooling/heating. Air cooling and water heating proved to be the most difficult systems to control due to the very large lag in response in this systems (dead time). In order to deal with this issue a cascade style control was implemented. Both air cooling and water heating employed a primary control that used temperature

measurements right at the water heater or air evaporator and a secondary (inner) control with temperatures measured at the inlet to the heat exchanger. The work of Cooper (2006) was extremely valuable in setting this control loops within the software and achieving tight control margins.

Since heaters and compressor ran on 480 VAC, a cabinet, with high voltage components and items that did not have to be accessed on a daily basis, was setup on one end of the calorimeter. A secondary smaller controls box was setup in a part of the system that was easier to access and more importantly without exposure to the 480 VAC bus as shown in Figure 20.



**Figure 20: Low voltage (left) and high voltage (right) cabinets**



Table 2 shows what National Instruments modules were used and their location in the system. Figure 21 shows the RTD calibration bath used for calibration of the inlet and outlet RTDs.

**Table 2: NI modules list and usage**

Module	Quantity	Usage	Location
9217	4	RTD inputs	External control box
9213	1	TC inputs	External control box
9227	1	Air-side pressure input	External control box
9411	1	Mass flow counter input	External control box
9203	1	RH and pressure input	External control box
9485	1	Mixing fans control	480 VAC box
9203	1	R404A system pressures input	480 VAC box
9211	1	R404A system temperatures	480 VAC box
9403	1	Relay control	480 VAC box
9265	2	VFD and SCR control	480 VAC box



**Figure 21: RTD calibration bath**

## 2.2. Test Conditions and Operating Procedure

Tube diameter, fin pitch, fin length and bank-bank angle were the geometric parameters controlled, see Table 4. Fin thickness was dependent on fin length. The fin thickness was determined by the width of the aluminum tape used in the manufacture of the fins and this was driven by commercial demand.

**Table 3: Test geometric variables**

Sample	Description	Tube OD [m]	Fin Pitch [m]	Fin Length [m]	Fin Thickness [m]	Bank-Bank angle [°]
Box1	3/8 in 7fpi Parallel S	9.53E-03	3.63E-03	<b>9.22E-03</b>	1.91E-04	0
Box2	3/8 in 10fpi Parallel S	9.53E-03	2.54E-03	1.01E-02	1.91E-04	0
Box3	3/8 in 12fpi Parallel S	9.53E-03	2.12E-03	1.01E-02	1.91E-04	0
Box4	5/16 in 7fpi Parallel S	8.03E-03	3.63E-03	1.01E-02	1.91E-04	0
Box5	5/16 in 10fpi Parallel S	8.03E-03	2.54E-03	1.01E-02	1.91E-04	0
Box6	5/16 in 12fpi Parallel S	8.03E-03	2.12E-03	1.01E-02	1.91E-04	0
Box19	3/8 in 7fpi Parallel L	9.53E-03	3.63E-03	1.17E-02	1.40E-04	0
Box20	3/8 in 10fpi Parallel L	9.53E-03	2.54E-03	1.17E-02	1.40E-04	0
Box21	3/8 in 12fpi Parallel L	9.53E-03	2.12E-03	1.17E-02	1.40E-04	0
Box22	5/16 in 7fpi Parallel L	8.03E-03	3.63E-03	1.17E-02	1.40E-04	0
Box23	5/16 in 10fpi Parallel L	8.03E-03	2.54E-03	1.17E-02	1.40E-04	0
Box24	5/16 in 12fpi Parallel L	8.03E-03	2.12E-03	1.17E-02	1.40E-04	0
Box1A	3/8 in 7fpi Angle S	9.53E-03	3.63E-03	<b>9.22E-03</b>	1.91E-04	11
Box2A	3/8 in 10fpi Angle S	9.53E-03	2.54E-03	1.01E-02	1.91E-04	11
Box3A	3/8 in 12fpi Angle S	9.53E-03	2.12E-03	1.01E-02	1.91E-04	11
Box4A	5/16 in 7fpi Angle S	8.03E-03	3.63E-03	1.01E-02	1.91E-04	11
Box5A	5/16 in 10fpi Angle S	8.03E-03	2.54E-03	1.01E-02	1.91E-04	11
Box6A	5/16 in 12fpi Angle S	8.03E-03	2.12E-03	1.01E-02	1.91E-04	11
Box19A	3/8 in 7fpi Angle L	9.53E-03	3.63E-03	1.17E-02	1.40E-04	11
Box20A	3/8 in 10fpi Angle L	9.53E-03	2.54E-03	1.17E-02	1.40E-04	11
Box21A	3/8 in 12fpi Angle L	9.53E-03	2.12E-03	1.17E-02	1.40E-04	11
Box22A	5/16 in 7fpi Angle L	8.03E-03	3.63E-03	1.17E-02	1.40E-04	11
Box23A	5/16 in 10fpi Angle L	8.03E-03	2.54E-03	1.17E-02	1.40E-04	11
Box24A	5/16 in 12fpi Angle L	8.03E-03	2.12E-03	1.17E-02	1.40E-04	11

In order to evaluate the air-side performance of the heat exchangers under different air-flow velocities a randomized test matrix was established in which

each air flow was tested at five different water mass flow rates. Air and water inlet temperature were kept constant. The different conditions are presented in Table 4.

**Table 4: Sample Test conditions**

Air velocity [m/s]	Air-flow Reynolds number	Water-flow [kg/s]	Water-flow Reynolds number	Air inlet Temp [°C]	Water inlet Temp [°C]
0.8	588	0.040	10690	10	57.2
0.9	687	0.043	11358		
1.0	780	0.045	12026		
1.2	873	0.048	12694		
1.3	980	0.050	13362		

A LabView application that automated the process of testing all these points was created. Limits were established for judging what variation was to be accepted for each measured parameter and once all parameters were within the given limits for an also provided stabilization time, data was saved for 5 minutes. If stability was not established after a given “Max Test Time”, the application would move on to the next test point. Defrost cycles were set after a fixed number of tests. The defrost cycles are highlighted in gray in Table 5.

The experiment was self-verifiable by virtue of a real-time heat load calculation on the air-side, equation 3 and water-side, equation 4.

$$\dot{Q}_a = \dot{m}_a \cdot C_p \cdot (T_{a\_out} - T_{a\_in}) \quad (3)$$

$$\dot{Q}_w = \dot{m}_w \cdot C_p \cdot (T_{w\_in} - T_{w\_out}) \quad (4)$$

An energy balance was calculated and displayed at all times in the user interface along with other information. The energy balance calculation is shown in equation 5.

$$\epsilon = \left(1 - \frac{\dot{Q}_a}{\dot{Q}_w}\right) \cdot 100\% \quad (5)$$

Table 5 shows a randomized test sequence. Columns 2, 4, 6, and 8 have the stability limit criteria for each subsystem. Columns 9, 10 and 11 specify how long each test point will be saved for once stability is achieved (save time), how long stability should be evaluated for (stabilization time) and finally what should the timeout be for each test point. If time out (max test time) was reached the system would proceed to the next test point. There were five, evenly spaced, test points in the test sequence where the target air temperature was increased to 26.7 °C. These were the defrost cycles. They removed ice accumulation in the large evaporator that cools the air before it moves into the heat exchanger under test. This air cooling system, as previously explained, is run by a R404A vapor compression cycle.

**Table 5: Randomized test sequence parameters**

Air-flow vel. [m/s]	Variation [± m/s]	Air inlet [°C]	Variation [± °C]	Water Flow [kg/s]	Variation [± kg/s]	Water inlet [°C]	Variation [± °C]	Save Time [min]	Stabilization time [min]	Max Test Time [min]
0.780	0.0260	10.0	0.6	0.043	0.0001	57.2	0.6	5	40	60
0.910	0.0260	26.7	0.6	0.043	0.0001	57.2	0.6	0	20	20
1.300	0.0780	10.0	0.6	0.050	0.0004	57.2	1.1	5	30	120
0.650	0.0780	10.0	0.6	0.050	0.0004	57.2	1.1	5	30	120
1.170	0.0780	10.0	0.6	0.050	0.0004	57.2	1.1	5	30	120
1.040	0.0780	10.0	0.6	0.048	0.0004	57.2	1.1	5	30	120
0.780	0.0780	10.0	0.6	0.040	0.0004	57.2	1.1	5	30	120
1.300	0.0780	10.0	0.6	0.043	0.0004	57.2	1.1	5	30	120
0.910	0.0780	10.0	0.6	0.040	0.0004	57.2	1.1	5	30	120
0.910	0.0260	26.7	0.6	0.043	0.0001	57.2	0.6	0	20	20
1.300	0.0780	10.0	0.6	0.045	0.0004	57.2	1.1	5	30	120
0.780	0.0780	10.0	0.6	0.048	0.0004	57.2	1.1	5	30	120
1.040	0.0780	10.0	0.6	0.043	0.0004	57.2	1.1	5	30	120
1.040	0.0780	10.0	0.6	0.050	0.0004	57.2	1.1	5	30	120
0.780	0.0780	10.0	0.6	0.045	0.0004	57.2	1.1	5	30	120
0.650	0.0780	10.0	0.6	0.040	0.0004	57.2	1.1	5	30	120
1.040	0.0780	10.0	0.6	0.040	0.0004	57.2	1.1	5	30	120
0.910	0.0260	26.7	0.6	0.043	0.0001	57.2	0.6	0	20	20
1.170	0.0780	10.0	0.6	0.043	0.0004	57.2	1.1	5	30	120
0.780	0.0780	10.0	0.6	0.043	0.0004	57.2	1.1	5	30	120
0.650	0.0780	10.0	0.6	0.045	0.0004	57.2	1.1	5	30	120
0.910	0.0780	10.0	0.6	0.043	0.0004	57.2	1.1	5	30	120
1.040	0.0780	10.0	0.6	0.045	0.0004	57.2	1.1	5	30	120
0.650	0.0780	10.0	0.6	0.048	0.0004	57.2	1.1	5	30	120
1.300	0.0780	10.0	0.6	0.040	0.0004	57.2	1.1	5	30	120
0.910	0.0260	26.7	0.6	0.043	0.0001	57.2	0.6	0	20	20
0.650	0.0780	10.0	0.6	0.043	0.0004	57.2	1.1	5	30	120
1.170	0.0780	10.0	0.6	0.045	0.0004	57.2	1.1	5	30	120
0.910	0.0780	10.0	0.6	0.050	0.0004	57.2	1.1	5	30	120
1.300	0.0780	10.0	0.6	0.048	0.0004	57.2	1.1	5	30	120
0.910	0.0780	10.0	0.6	0.045	0.0004	57.2	1.1	5	30	120
1.170	0.0780	10.0	0.6	0.048	0.0004	57.2	1.1	5	30	120
1.170	0.0780	10.0	0.6	0.040	0.0004	57.2	1.1	5	30	120
0.910	0.0260	26.7	0.6	0.043	0.0001	57.2	0.6	0	20	20
0.910	0.0780	10.0	0.6	0.048	0.0004	57.2	1.1	5	30	120
0.780	0.0780	10.0	0.6	0.050	0.0004	57.2	1.1	5	30	120

### 2.3. Uncertainty Analysis

The very low flows at which the heat transfer surfaces being evaluated operate at present one of the main challenges in the experiments conducted. Achieving energy balance at these very low flows can be problematic. The question of whether the measurement system selected provides sufficient resolution is answered with an uncertainty analysis.

The goal was to capture the true value of the measurement being made knowing that the measured value would be the sum of a systematic error ( $\beta$ ) and a random error ( $\epsilon$ ) in the measurement system.

The systematic error is the component that will stay constant throughout our measurement. This error is normally provided by the manufacturer of the device used in terms of an absolute value, such as with thermocouples (TCs). It may also be found as a percentage of a reading or a percentage of the full scale of the instrument as is the case with pressure transducers.

The random error is the error that varies due to causes, normally out of our control, during the experiment, Coleman and Steele (2009).

The distribution of the measurements in a given test period ( $s_x$ ) is the root sum of squares (RSS) of the individual random errors on that given measurement. The total uncertainty for a given measurement will be the RSS of the systematic error uncertainties ( $b_x$ ) plus the contributions from the variable errors for the given measurement ( $s_x$ ).

The total uncertainty for a given measurement is:

$$u_x = \sqrt{(b_{x,B}^2 + s_{x,A}^2)} \quad (6)$$

The subscripts A and B represent uncertainty type. 'A' being an uncertainty obtained by "statistical analysis of a series of observations" and type 'B' by "other than statistical analysis of a series of observations", in this case they were obtained from manufacturer specifications.

The systematic uncertainties are detailed in Table 6.

**Table 6: Instrument uncertainties**

Instrument	Units	Accuracy
RTD inlets and outlets	°C	0.05
Pressure transducer (barometric)	Pa	1016
Pressure transducer (nozzles)	Pa	12.45
Mass flow meter (Coriolis)	g/s	0.025% of reading
Relative Humidity	-	0.6% of reading

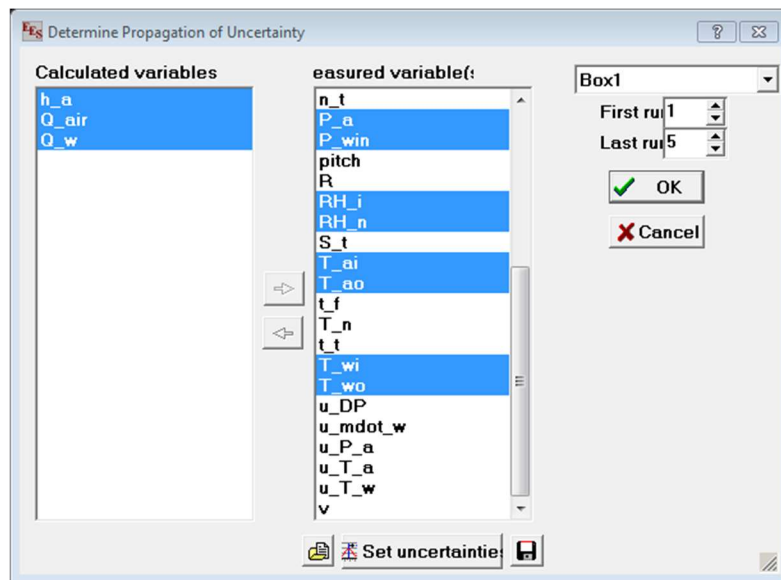
A significant investment was made in purchasing a mass flow meter and transmitter with the lowest available uncertainty.

### 2.3.1. Calculation procedure

#### ***Systematic Uncertainty***

Systematic uncertainty was calculated with the RSS technique using Engineering Equation Solver (EES). As a first step, a lumped analysis of the heat exchanger is programmed in EES and data for each of the 24 samples being evaluated is

input into a parametric table. The uncertainties from Table 6 are assigned to variables in the program. Uncertainties for each of the 24 cases are calculated individually via the “Uncertainty Propagation Table” under the calculate menu in EES, see Figure 22.



**Figure 22: Uncertainty propagation table in EES**

EES parametric table output is shown in Table 7. The systematic uncertainty for all 24 samples is saved as a matrix that will then be imported by Matlab. The uncertainties are saved for Air-side heat transfer coefficient ( $AHTC$ ), heat load air-side ( $Q_a$ ), heat load water-side ( $Q_w$ ) and overall heat transfer coefficient ( $U_o$ ).



**Table 7: Uncertainty output example EES**

Parametric Table				
EESdata				
1	2	3	4	
1.608	$h_a$ [W/m <sup>2</sup> -K]	$Q_{air}$ [W]	$Q_w$ [W]	$U_o$ [W/m <sup>2</sup> -K]
Run 1	48.144±2.2391	677.14±6.9487	692.34±13.414	42.51±1.749
Run 2	55.270±1.9137	804.64±8.2880	822.27±12.669	47.82±1.436
Run 3	44.426±2.5653	607.20±6.2441	622.69±14.159	39.68±2.05
Run 4	44.861±2.3598	605.23±6.2265	619.84±12.668	39.82±1.862
Run 5	52.315±1.9450	737.82±7.6040	755.35±11.924	45.43±1.47
Run 6	49.109±2.0866	673.86±6.9424	692.97±11.923	42.99±1.602
Run 7	51.176±2.2807	747.52±7.6959	760.83±14.904	45.1±1.775
Run 8	57.702±2.0824	869.89±8.9581	883.06±14.904	50.09±1.573
Run 9	48.298±2.3555	681.88±7.0163	698.77±14.159	42.74±1.848
Run 10	54.834±2.0933	807.01±8.3161	822.90±14.159	47.79±1.594
Run 11	55.092±2.0095	805.59±8.3026	823.21±13.414	47.84±1.519
Run 12	45.149±2.2666	603.27±6.2037	617.10±11.923	39.93±1.775

## Random Error

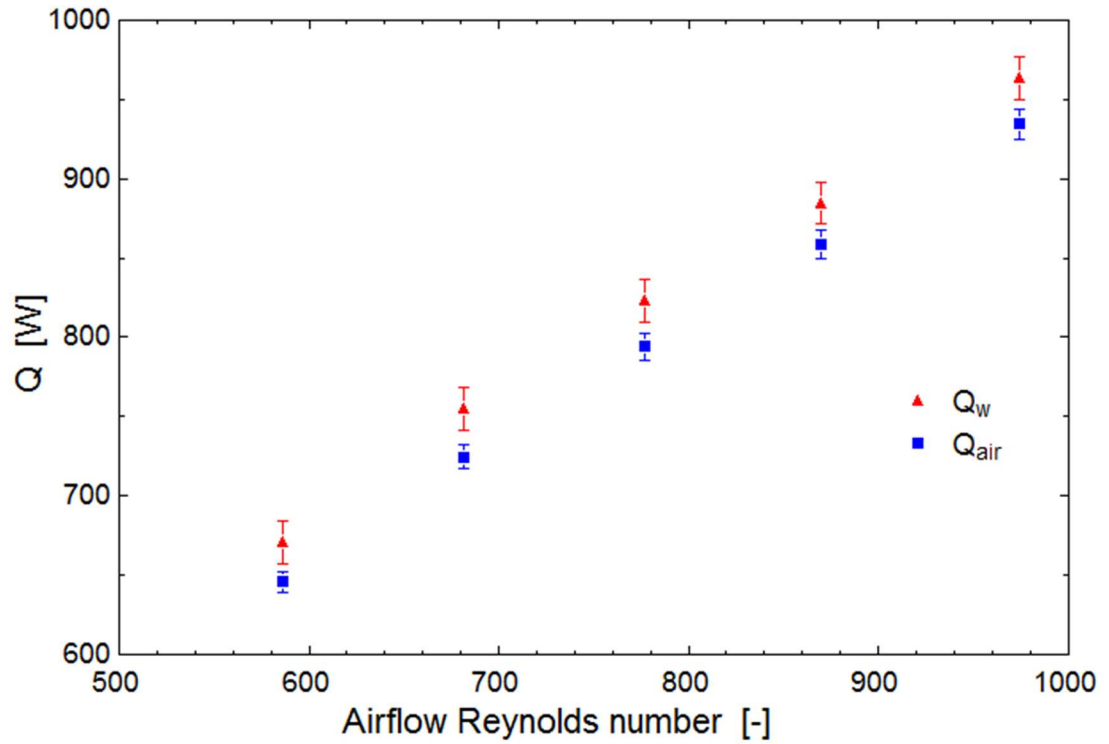
The contributions from variable errors  $s_x$  were calculated from the standard deviation of all the test points collected at each test point. These values were calculated using a program written in Matlab. Matlab was selected as the program that would consolidate all data because Matlab is better suited to deal with very large data sets and due to its flexible plotting capabilities.

As mentioned previously, EES Systematic Error uncertainty was imported to Matlab and the total uncertainty was calculated in Matlab using equation 6.

**Table 8: Sample calculated error values**

Variable	Unit	Measured Value	Systematic Error $b_{x,B}$	Random Error $s_{x,A}$	Total Error $u_x$	Relative Error
Water MFR	$kg/s$	0.045	1.1E-5	1.45E-4	1.5E-4	0.32%
Air flow	$m^3/s$	0.014	3.9E-4	1.1E-5	7.4E-5	2.75%
$T_{w, in}$	$K$	330.4	0.05	7.2E-2	8.7E-2	0.03%
$T_{w, out}$	$K$	327.0	0.05	6.3E-2	8E-2	0.02%
$T_{a, in}$	$K$	283.1	0.05	7.26E-3	5.1E-2	0.02%
$T_{a, out}$	$K$	317.4	0.05	2.9E-2	5.8E-2	0.02%
$Q_{water}$	$W$	621.2	13.29	5.9	15	2.4%
$Q_{air}$	$W$	607.4	16.24	2.8	16.6	2.7%
$h_{air}$	$W/m^2K$	43.64	1.2	0.45	1.3	3%

Experiments ran showed an energy balance error between the water-side and air-side of about 3%. Thanks to the high quality sensors used in the experiment, relative errors for all measured variables are below 1%. It was not surprising to find that airflow had a larger relative error than water mass flow. What was surprising was that even though the systematic error for water-side heat capacity was lower; the random error was consistently higher, much higher than that of the air-side. Therefore the side that I always suspected would give me the most difficulty in the experiment, turned out to be the side with the tightest distributions in heat load. An example of the aforementioned can be seen in



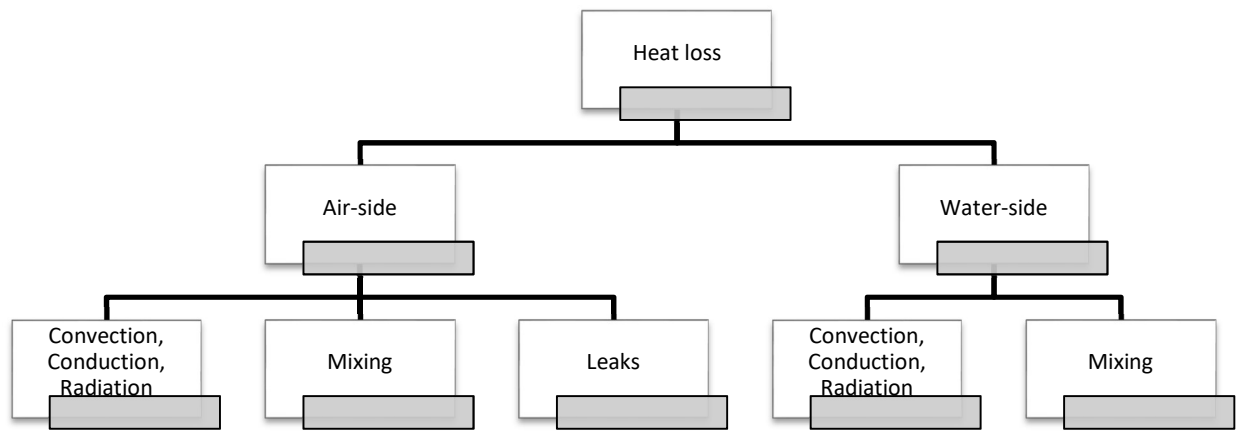
**Figure 23: Distribution of data for heat load, 10 fpi, 3/8 in tube, short fin**

The higher variable error ( $s_{x,A}$ ) in the water mass flow measurement can be attributed to the constant corrections made by the PI controller for the pump's variable frequency drive. This is something that can be improved in the tuning of the control but it was never even considered as an issue since energy balance error was very low.

### 3. Data Reduction

#### 3.1. Energy Balance

In an ideal heat exchanger calorimetry experiment all of the heat lost by the hot fluid (water) would be captured by the cold fluid (air). However, the unit under test compartment in the calorimeter is not an adiabatic box and the system is far from ideal. Despite this, energy balances of around 3% and better were achieved by managing heat loss in its three modes; convective, conductive and radiative. Figure 24 presents a summary of all energy balance error sources.



**Figure 24: Energy balance error sources**

The air-side presented the biggest challenge in terms of achieving an accurate temperature measurement. Starting with heat losses to the ambient, convective heat transfer was found to have the greatest impact. The error increased at lower air flows. At this low flows a layering of the temperatures started to become more apparent. To solve this issue, active mixing of the inlet air was done before the settling screens prior to the unit under test section of the

calorimeter. At the outlet of the heat exchanger and prior to the eight outlet RTDs a static mixer was installed. These approaches along with large amounts of fiberglass insulation were sufficient to manage convective heat transfer losses.

It was also very important that no air flow was lost within the system or to the atmosphere. Any air that was measured at the airflow chamber and did not make it through the unit under test would decrease the capacity of the heat exchanger and show up in the form of poor energy balance. Typical heat load and energy balance values are presented in Table 9.

**Table 9: Typical heat load and energy balance values**

	Face Velocity [m/s]	Air-flow Reynolds number	Q <sub>air</sub> [W]	Q <sub>water</sub> [W]	Energy Balance Error [%]
7fpi short, Parallel, 3/8in tube	0.83	816	606.8	621.3	2.3
	0.97	953	678.7	695.6	2.4
	1.10	1087	742.7	759.2	2.2
	1.24	1224	804.7	823.4	2.3
	1.38	1361	863.0	881.1	2.1
12fpi short, Parallel, 5/16in tube	0.82	561	671.0	686.5	2.3
	0.96	655	760.3	776.3	2.1
	1.10	749	840.1	854.8	1.7
	1.23	844	918.9	932.5	1.5
	1.37	939	991.4	1001.6	1.0
10fpi long, Angle, 3/8in tube	0.51	517	553.8	568.2	2.5
	0.59	604	623.7	639.0	2.4
	0.68	691	691.8	703.7	1.7
	0.76	778	753.3	764.6	1.5
	0.85	865	811.8	824.1	1.5

The capacity ranges observed in the experiment are higher than what is seen in a household refrigerator. The high capacity in the experiment is driven by the

large temperature differences between the air and the water. Experiment's temperatures were selected to reduce measurement uncertainty.

### 3.2. Air-side Heat Transfer Performance

The overall conductance ( $UA$ ) of the coil is the results of the sum of the individual resistances in a thermal network as shown in equation (7). Tube side thermal resistance ( $R_t$ ) is less than 1% of the total thermal resistance ( $R_T$ ).

$$UA = \frac{1}{R_T} = \frac{1}{R_a + R_t + R_w} = \frac{1}{\frac{1}{\eta_s h_a A_a} + \frac{\ln(r_o/r_i)}{2\pi k_t L_t N_t} + \frac{1}{h_w A_w}} \quad (7)$$

The next low contributor is the water-side thermal resistance ( $R_w$ ) at about 6.5% of the total thermal resistance in the thermal network. Thus  $R_T$  is driven mainly by the air-side thermal resistance ( $R_a$ ). As in all compact heat exchangers, air-side performance is the limiting factor.

Surface efficiency is a function of surface area and fin efficiency and it is calculated as shown in equation (8)

$$\eta_s = \frac{A_p + \eta_f \cdot A_s}{A_T} \quad (8)$$

Where fin efficiency is calculated per Shah and Sekulic (2003) as shown in equations (9 - 11).

$$\eta_f = \frac{\tanh(m \cdot L_{ch})}{m \cdot L_{ch}} \quad (9)$$

$$m = \sqrt{\frac{2 h_a}{k_{fin} t_f} \left[ 1 + \frac{t_f}{f_w} \right]} \quad (10)$$

The characteristic length is the length of the fin plus the one half of the tip:

$$L_{ch} = l_f + \frac{t_f}{2} \quad (11)$$

Since air-side heat transfer coefficient was used in the calculation of fin efficiency and fin efficiency was used to calculate surface efficiency, a component of air-side thermal resistance ( $R_a$ ), an iterative calculation had to be implemented.

I solved for the unknown air-side heat transfer coefficient ( $h_a$ ) in equation (7) after calculating  $UA$  based on equation (12).

$$UA = NTU \cdot \dot{C}_{min} \quad (12)$$

The minimum heat capacity ( $\dot{C}_{min}$ ) corresponds to the heat capacity of the air ( $\dot{C}_a$ ) and it is a property readily available.

The number of transfer units ( $NTU$ ) is defined by equation (13) found in Nellis and Klein (2009).

$$NTU = - \left[ \frac{\ln(\dot{C}_r \cdot \ln(1 - \varepsilon) + 1)}{\dot{C}_r} \right] \quad (13)$$

The  $\varepsilon - NTU$  formulas available deal with crossflow or counterflow heat exchangers with streams mixed and/or unmixed. The heat exchangers tested had flows that are cross-counter flow. While calculations were still completed using the lumped analysis approach a better approximation was sought by applying a finite volume calculation. The software CoilDesigner, Jiang et al. (2006), was used to solve for a heat transfer coefficient value on the air-side. Within CoilDesigner, the “Coil Data Reduction Tool” takes all the inlet and outlet stream parameters for a given heat exchanger test and then using the input geometry performs a finite volume analysis, iteratively guessing an air-side heat transfer coefficient ( $h_a$ ) that will produce outlet conditions as tested, based on the inlet conditions given.

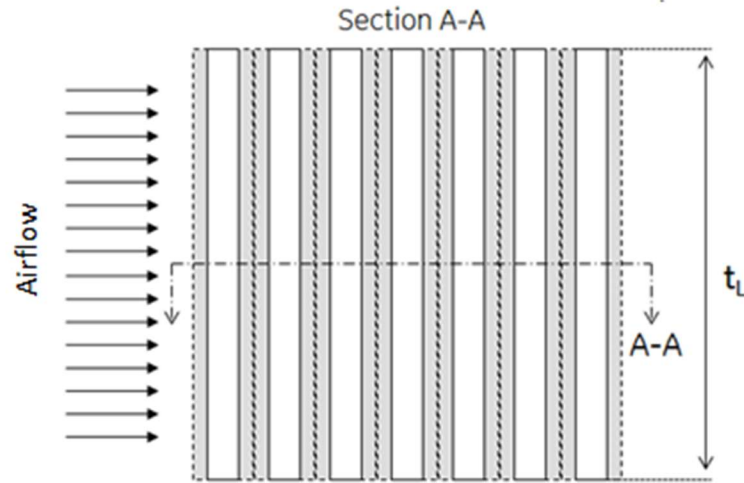
Finally, calculation of the tube-side resistance ( $R_t$ ) is easily done with geometry data and material properties from the sample coils. See equation 14.

$$R_t = \frac{\ln \left[ \frac{D_o}{D_i} \right]}{k_{Al} \cdot 2 \cdot \pi \cdot t_L} \quad (14)$$

As shown in equations (7) and (8), primary surface area calculations are very straight forward. However, secondary area calculations, due to the fin geometry, require some care. The following section details these calculations and the definition of hydraulic diameter for this geometry.

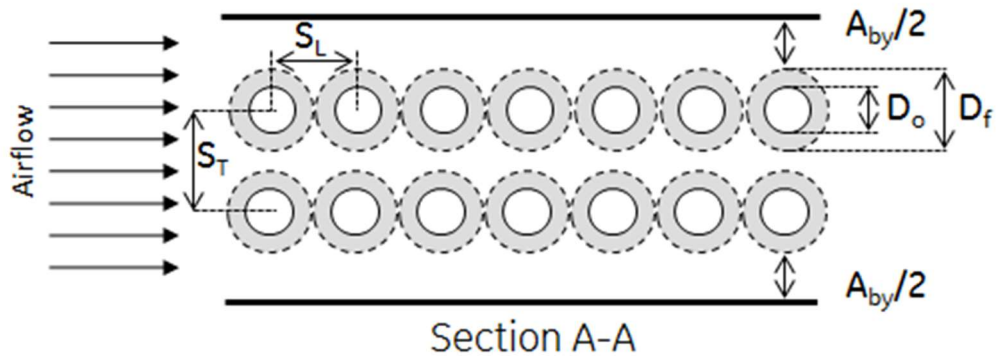


The geometry definitions for the test sections are detailed in Figure 25 and Figure 26. The arrows on the left side of the figure show the direction of the airflow. Figure 25 shows a top view of a heat exchanger with  $t_L$  being the length of each finned-tube.



**Figure 25: Test section top view**

Figure 26 is a view of the cross section A-A shown in Figure 25.  $D_o$  and  $D_f$  are tube outer diameter and finned-diameter, respectively. Finned-diameter ( $D_f$ ) is the fin-tip to fin-tip distance on a finned-tube.

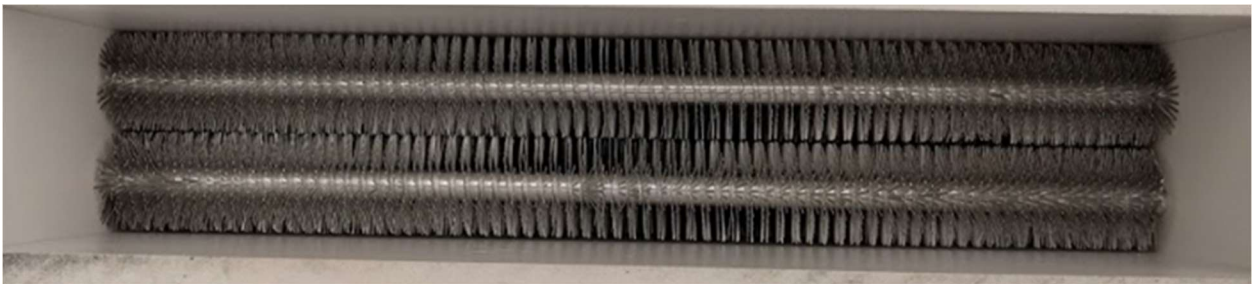


**Figure 26: Parallel banks cross section view**

Tube-to-tube distance transversal to air flow into the heat exchanger is  $S_T$ . Longitudinal distance with respect to the flow of air into the heat exchanger is  $S_L$ . The  $S_T$  parameter is particularly important because it indicates if the heat exchanger under test is a parallel or angled configuration heat exchanger.

$A_{by}$  is bypass area. Air bypass happens in application in a refrigerator due to process variation and manufacturing control issues. Because of this variation, small gaps between the heat exchanger and the evaporator cover and the back wall of the refrigerated space are generated. These gaps allow small quantities of air to bypass the heat exchanger.

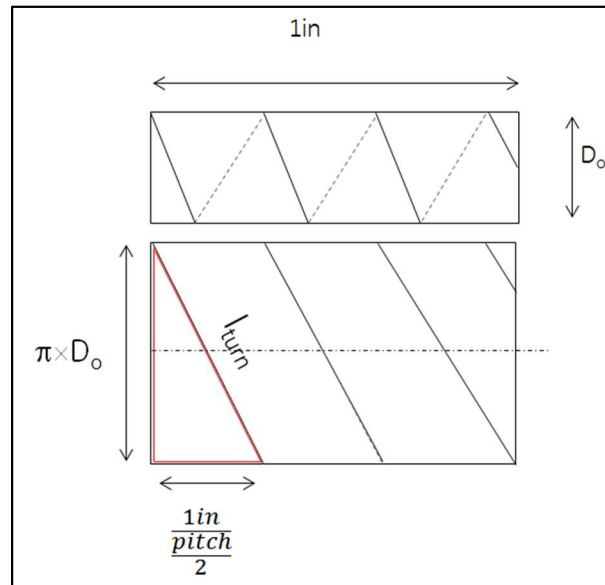
Bypass area was eliminated in this study by having the tubes in close contact with the top and bottom of the heat exchanger box. The decision to eliminate bypass was driven by the randomness of this gap in application and in an effort to minimize the number of variables tested. Figure 27 shows how close this gap is controlled.



**Figure 27: Tubes in duct**

### 3.2.1. Air-side surface area

Consider a 25.4 mm (1 in) tube segment with 3.5 wraps of fin material. A double row of fins is applied to the tube with each wrap of the material, as shown in Figure 3. Therefore, 3.5 wraps of material around the 25.4mm (1in) segment is equal to 7 fins per inch (fpi). Next, imagine cutting the segment lengthwise and flattening the segment as show in Figure 28. The new flattened section will have a series of right triangles formed by the wrapped fin material. The hypotenuse of the triangles will be each turn of the fin material around the tube, the length of the other two legs of the triangle are defined by the circumference of the original tube segment and the shortest leg by the length of the segment of tube divided by the number of wraps or by half of the pitch.



**Figure 28: Finned tube segment**

In order to calculate the total secondary area (fin area), the first step is to calculate the length of one turn of the helix that the fins follow on as they are wrapped around the tube. In the manufacturing of our spine fin-tube, there are 2 rows of fins on each helix turn.

Equation (15) calculates the length of a single turn of the helix (hypotenuse of the triangle in Figure 28). The stretch ratio is accounted for as well. The stretch ratio ( $s_r$ ) is the mechanical stretching applied to the fin material as it is wrapped around the tube.

$$l_{turn} = \sqrt{(\pi \cdot D_o)^2 + \left(\frac{2}{pitch}\right)^2} \cdot (1 - s_r) \quad (15)$$

The number of fins per turn of the helix is calculated in equation (16); it is multiplied times two because there are two fins per fin material turn around the tube.

$$n_f = \frac{l_{turn}}{w_f} \cdot 2 \quad (16)$$

The total number of turns of fin material or helix loops is:

$$turns_t = L_t \cdot \frac{pitch}{2} \quad (17)$$

$L_t$  is the length of each tube.

The fin area per turn of the helix around the tube is calculated as:

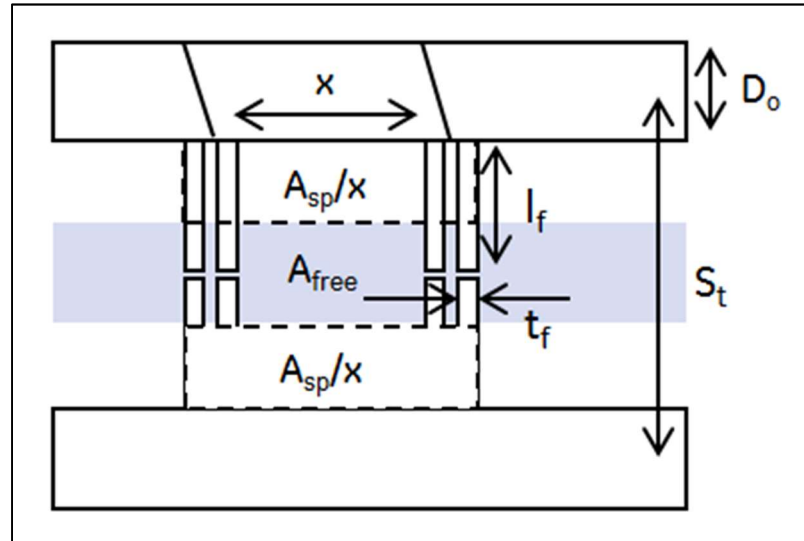
$$A_{turn} = n_f \cdot A_f \quad (18)$$

Finally, the total secondary area is the product of the area per turn of the helix around the tube and the fin area per turn.

$$A_s = turns_t \cdot A_{turn} \quad (19)$$

### 3.2.2. Spine fin-tube hydraulic diameter calculation

A method for calculating the air-side hydraulic diameter had to be derived. This was accomplished by visualizing the many individual fins in the air flow as one equivalent solid section as shown in Figure 29.



**Figure 29: Free flow area normalization**

The free flow area of the coil, the gray area in Figure 29, is calculated as shown in equation (25). Where  $D_f$ ,  $n_t$  and  $x$  are finned diameter, number of tubes in the face of the heat exchanger and helix turn distance, respectively.

Face area of coil is calculated as:

$$A_{fr} = [s_T \cdot (n_t - 1) + D_f + A_{by}] \cdot t_L \quad (20)$$

Volume of the heat exchanger is:

$$v = A_{fr} \cdot [s_L \cdot (n_b - 1) + D_f] \quad (21)$$

Spacing between helix turns is:

$$x = \frac{2}{pitch} \quad (22)$$

Surface area to heat exchanger to volume ratio is:

$$\alpha = \frac{A_T}{v} \quad (23)$$

The area that the fin projects into the airflow is:

$$A_{sp} = t_f \cdot l_f \cdot 4 \quad (24)$$

Free flow area is:

$$A_{free} = \left[ (s_T \cdot D_f) - (n_t - 1) + \left( D_f - D_o - \frac{A_{sp}}{x} \right) \cdot A_{by} \right] \cdot t_L \quad (25)$$

Ratio of free flow area to frontal area as defined by Kays and London (1984) is:

$$\sigma = \frac{A_{free}}{A_{fr}} \quad (26)$$

Hydraulic radius and diameter per Kays and London (1984) are:

$$r_h = \frac{\sigma}{\alpha} \quad (27)$$

$$D_h = 4 \cdot r_h \quad (28)$$

Mass flux of air and Reynolds number are:

$$G_a = \frac{\rho_a \cdot q_a}{A_{free}} \quad (29)$$

$$Re_a = \frac{D_h \cdot G_a}{\mu_a} \quad (30)$$

In addition to AHTC and heat exchanger pressure drop versus face velocity, performance is evaluated and presented with the Colburn *j-factor* and the non-dimensional friction factor, *f*. Both plotted versus air-side Reynolds number.

The Colburn *j-factor* is defined as:

$$j = St \cdot Pr^{2/3} \quad (31)$$

Where the Stanton number (*St*) is calculated as:

$$St = \frac{h_a}{G_a C p_a} \quad (32)$$

The friction factor ( $f$ ) in terms of pressure drop as shown below:

$$f = \frac{r_h}{L} \frac{1}{\left(\frac{1}{\rho_m}\right)} \left[ \frac{2 g_c \Delta P}{G^2} - \frac{1}{\rho_i} (1 - \sigma^2 + K_c) - 2 \left( \frac{1}{\rho_o} - \frac{1}{\rho_i} \right) + \frac{1}{\rho_o} (1 - \sigma^2 + K_e) \right] \quad (33)$$

$L$  in equation 33 is the heat exchanger core length and  $K_c$  and  $K_e$  are sudden contraction and expansion pressure drop coefficients at  $\sigma = 0.6$  per equation (26) the values (0.3 and 0.2, respectively) were obtained from data developed by Kays and London found in Shah and Sekulic (2003).

The fluid axial velocity at the minimum free flow area is:

$$u_m = \frac{\dot{m}_a}{\rho_{ai} A_{free}} \quad (34)$$

### 3.3. Water-side Heat Transfer Performance

For the calculation of the thermal resistance of the water ( $R_w$ ), it is assumed that the efficiency is unity, the tubes are not enhanced with micro grooves. Area on the water-side is easily calculated from geometry data of the samples tested. Water-side heat transfer coefficient is calculated using the Gnielinski (1976) correlation.

$$h_w = k_w \cdot \frac{Nu_w}{D_i} \quad (35)$$

Where Nusselt number for water is defined by equation (36)



$$Nu_w = \frac{0.5 \cdot f \cdot (Re_w - 1000) \cdot Pr}{1 + 1.27 \cdot \sqrt{0.5 \cdot f} \cdot (Pr^{0.667} - 1)} \quad (36)$$

$$f = \frac{1}{(1.58 \cdot \ln(Re_w) - 3.28)^2} \quad (37)$$

Mixing issues were a problem initially when the system was run at flows that were not above 10,000 Reynolds number. RTDs in a mixing head that were separated by no more than 5mm would read different temperatures ( $>0.5^\circ\text{C}$ ). Another issue was that at low Reynolds numbers air natural convection on the coil would have a measurable impact on water temperature when comparing inlet to outlet temperatures. Implementing higher mass flows that produced above 10,000 Reynolds numbers had two favorable effects. Better mixing at the inlet and outlet heads and natural convection had no impact on water temperatures. While leaks are a problematic issue on the water-side, they were easier to spot than air leaks and once issues were corrected, easier to avoid in general.

### 3.4. Air-side Pressure Drop

Air-side pressure drop was measured directly with a differential pressure transducer. Each heat exchanger was housed in an extruded PVC box that had inlet and outlet pressure measurement taps. Four inlet and four outlet taps were machined and each set was interconnected with silicone tubing and then connected to the differential pressure transducer. Each tube segment interconnecting individual taps was cut at the same length as show in ASHRAE (1992).

## 4. Data Analysis

This section covers the data analysis of all coils tested. Graphical comparisons of heat transfer coefficient and air-side pressure drop are particularly helpful in understanding the performance difference of the different geometries.

Since all tests were conducted at the same set of inlet stream temperatures a comparison of heat loads would have been accurate. However, the different test sections have different surface areas. Therefore, normalization in terms of surface area was necessary for a fair comparison of all the coils. Since air-side is the performance limiting factor for our heat exchangers, the comparison of air-side heat transfer coefficient ( $h_a$ ) is then an informative way of comparing the performance of all the coils. While air-side heat transfer coefficient ( $h_a$ ) was calculated with a lumped analysis of the coil, the data presented in the following comparisons will be the heat transfer coefficient derived by a finite volume analysis as calculated in CoilDesigner.

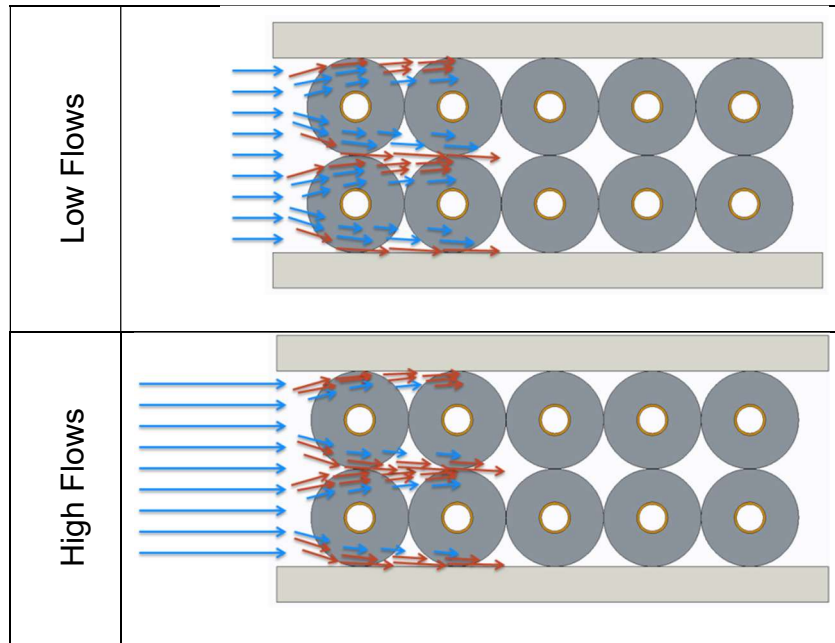
Performance dependence based on bank-to-bank angle was not explicitly graphed because for all tests completed; face velocities, capacities, heat transfer coefficients and pressure drops were lower in angled configurations than in parallel configurations. In short, a parallel coil is a better performer, always, but has higher pressure drop and in application would be particularly susceptible to air-side blockage due to frost accumulation further increasing pressure drop.

#### 4.1. Tube and Fin Pitch Dependence

On most heat exchangers, for example micro-channel, plain or spiral fin-tube, there is a clear passage or channel through which the air will flow. There are exceptions, such as staggered fin arrangements, however, the concept of an uninterrupted passage holds true in between the fin staggering. Therefore, as fin density increases, velocity increases and with it pressure drop. The increased velocity brings about an increase in AHTC.

In contrast, spine fin-tube heat exchangers offer such a plurality of obstacles to flow that friction forces a leakage condition. This leakage is seen at the fin-tip to fin-tip interface between tubes and at the fin-tip to duct interface. The flow closest to the tube is restricted and while there is an increase in pressure drop there is no gain in AHTC. The increase in pressure drop is generated by the small leakage cross section. Because the high velocities are concentrated at the fin tips there is no performance gain.

Figure 30 shows in blue the incoming productive flow into the heat exchanger. The red arrows show the leakage flow. At higher flows more of the total flow becomes leakage flow. Leakage flow is less productive in terms of heat transfer. Notice that in the bottom image in Figure 30 (“High Flows”), the cross-section that the air moves through is reduced when compared to the “Low Flows” image, this reduction in flow path contributes to the increase in pressure drop mentioned before.



**Figure 30: Flow leakage**

Figure 32 through Figure 43; show the impact of tube diameter on heat transfer and also pressure drop performance of the coils. In general it can be seen that heat exchangers with 5/16 in diameter tubing have higher air-side heat transfer coefficient and lower air-side pressure drop than their 3/8 in tube counterparts at the same fin density.

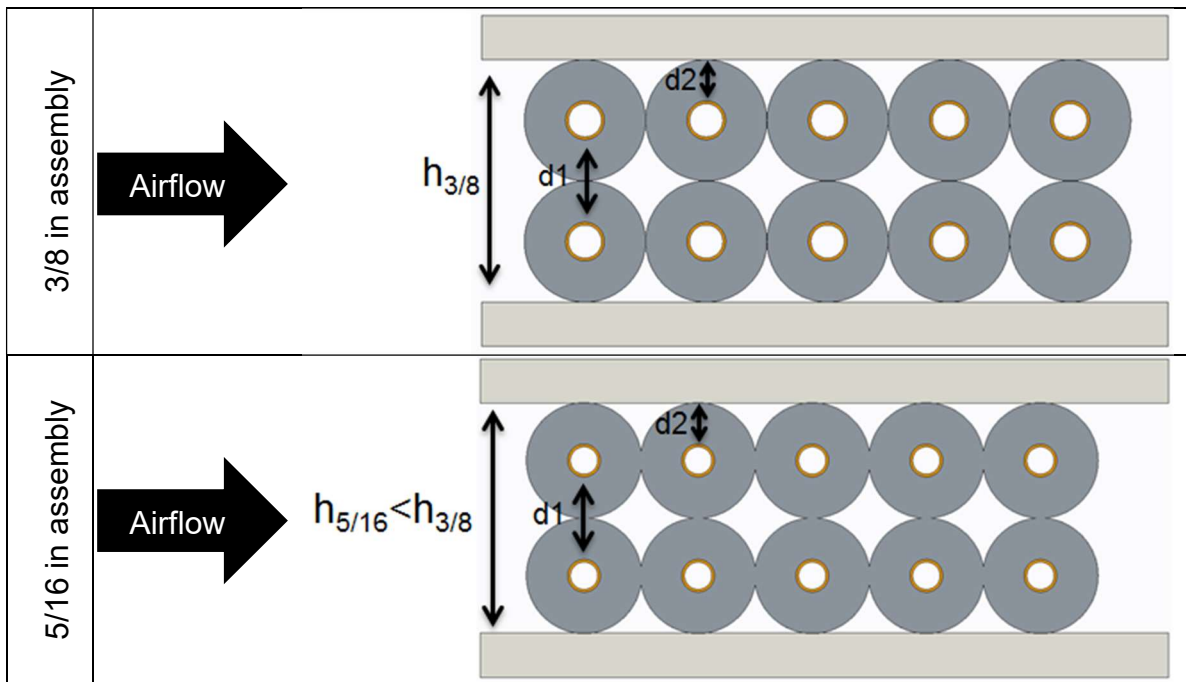
The data also shows that 5/16 in tube assemblies have lower pressure drop than their 3/8 in counterparts at a given airflow velocity. The reasoning behind this is that by reducing the diameter of the tubes, we effectively reduce the size of the restriction in the direction of the flow.

The higher AHTC on 5/16 in tubes can be explained by considering the tube-to-tube and tube-to-duct dimensions for a 3/8 in and 5/16 in assembly.

Table 10 shows a set of typical dimensions from two heat exchangers and Figure 31 details these dimensions.

**Table 10: Sample dimensions 3/8 in and 5/16 in**

Geometry	3/8 in	5/16 in
Tube OD [mm]	9.5	8.0
Fin length [mm]	10.13	10.13
Fin thickness [mm]	0.19	0.19
Fin pitch [mm]	3.63	3.63
Face height, h [mm]	59.69	55.88
Tube-tube, d1 [mm]	20.27	20.27
Tube-duct, d2 [mm]	10.13	10.13
Face area [mm <sup>2</sup> ]	18154.8	17187.1



**Figure 31: Dimensions detail in samples**

Based on the dimensions and samples presented above; for a given heat exchanger face velocity a 5/16 in assembly will see a lower tube velocity and based on the ideas presented at the beginning of this section and in Figure 30, the 5/16 in assembly will experience lower flow leakage and therefore a higher AHTC.

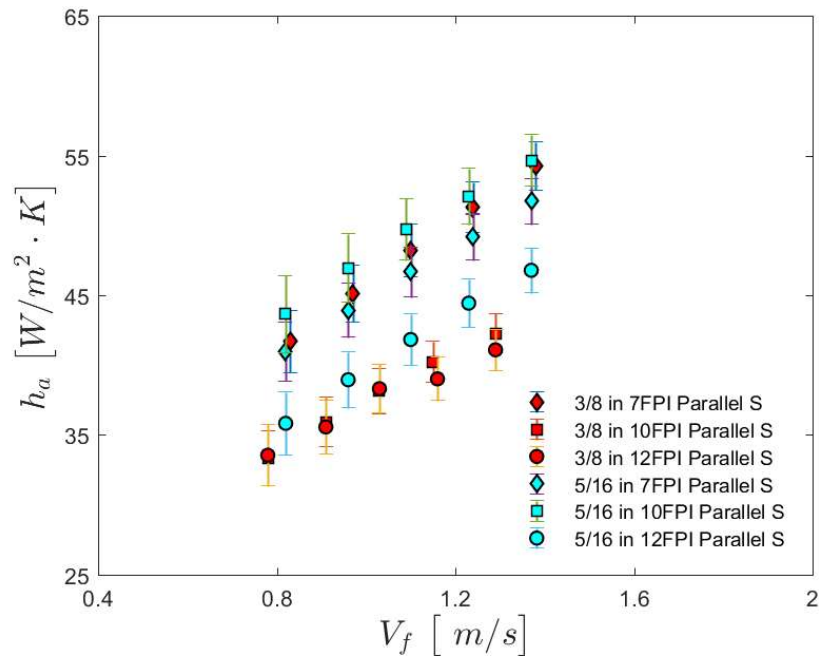
#### 4.1.1. Parallel configuration short fin

In terms of AHTC, the 10 fpi, 5/16 in diameter tube performs better than the 7fpi, see Figure 32. This is a reversal in trends from all other heat exchangers with the exception of the parallel, long fin configuration. Heat load for the 10 fpi, 5/16 in heat exchanger matched the heat load for the 12 fpi, 5/16 in sample, a larger surface area heat exchanger. In this case there is no capacity gain derived from an increase in surface area and this is driven by the large difference in  $h_a$ .

One possible explanation for the 5/16 in 10 fpi having a higher AHTC might be bypass between tubes on the 7 fpi sample. As seen in Figure 33, the 7fpi sample has a large gap between fin tips that is not seen on the 10 fpi, this gap could be driving the AHTC deficiency on the 7fpi sample in both the long and short fin configurations. Another explanation might be unusually high contact resistance from relaxation of the fin material (helix) around the tube on the 7 fpi sample, however this would have had to happen on both short and long fin samples.

In 3/8 in diameter there is a clear performance lead by the 7 fpi sample. The size of the lead might be related to the fact that these samples came from a machine

that applied a hem to the fin. The hem reduced the fin height by 0.9 mm. The fin height reduction created a smaller face area on this coil which increased pressure drop. Figure 34 shows that 3/8in tube in 7 fpi and 10 fpi and in 5/16 in 10 fpi and 12 fpi are very close in terms of pressure drop.

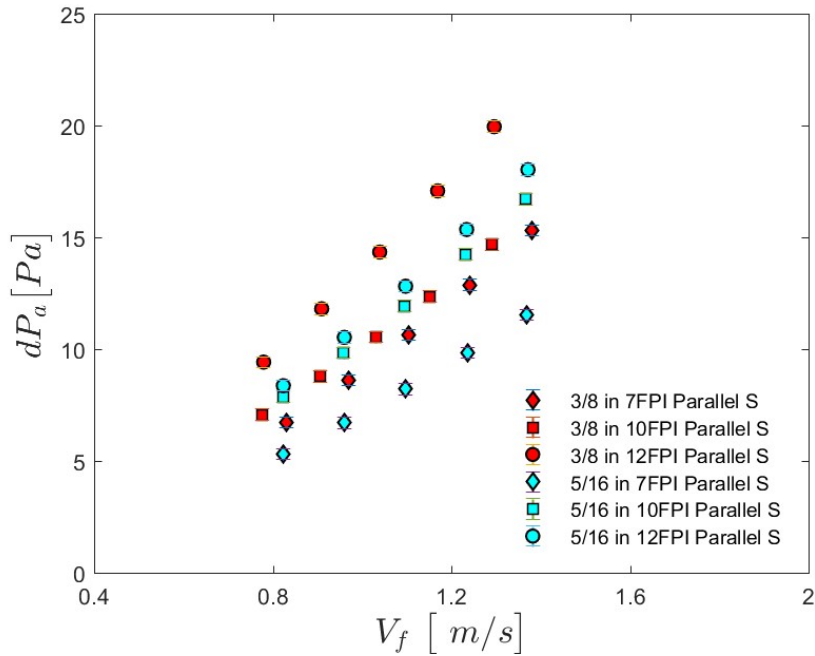


**Figure 32: AHTC, parallel banks, short fin**



**Figure 33: 5/16 in 7fpi fin-tip to fin-tip gap**

The AHTC of the 7 fpi samples are not dependent on tube diameter at lower flows, however, as velocity increases there is a difference in performance favoring the 3/8 in sample.



**Figure 34: Pressure drop, parallel banks, short fin**

The reduced face area on the 7 fpi, 3/8 in tube heat exchanger can be seen in the air-side pressure drop which is almost on par with the 10 fpi, 3/8 in tube heat exchanger as seen in Figure 34.

The  $j$ -factor and  $f$ -factor plots show trends expected in spine fin; friction factor,  $f$  could predict  $j$ -factor for every heat exchanger as seen Figure 35.



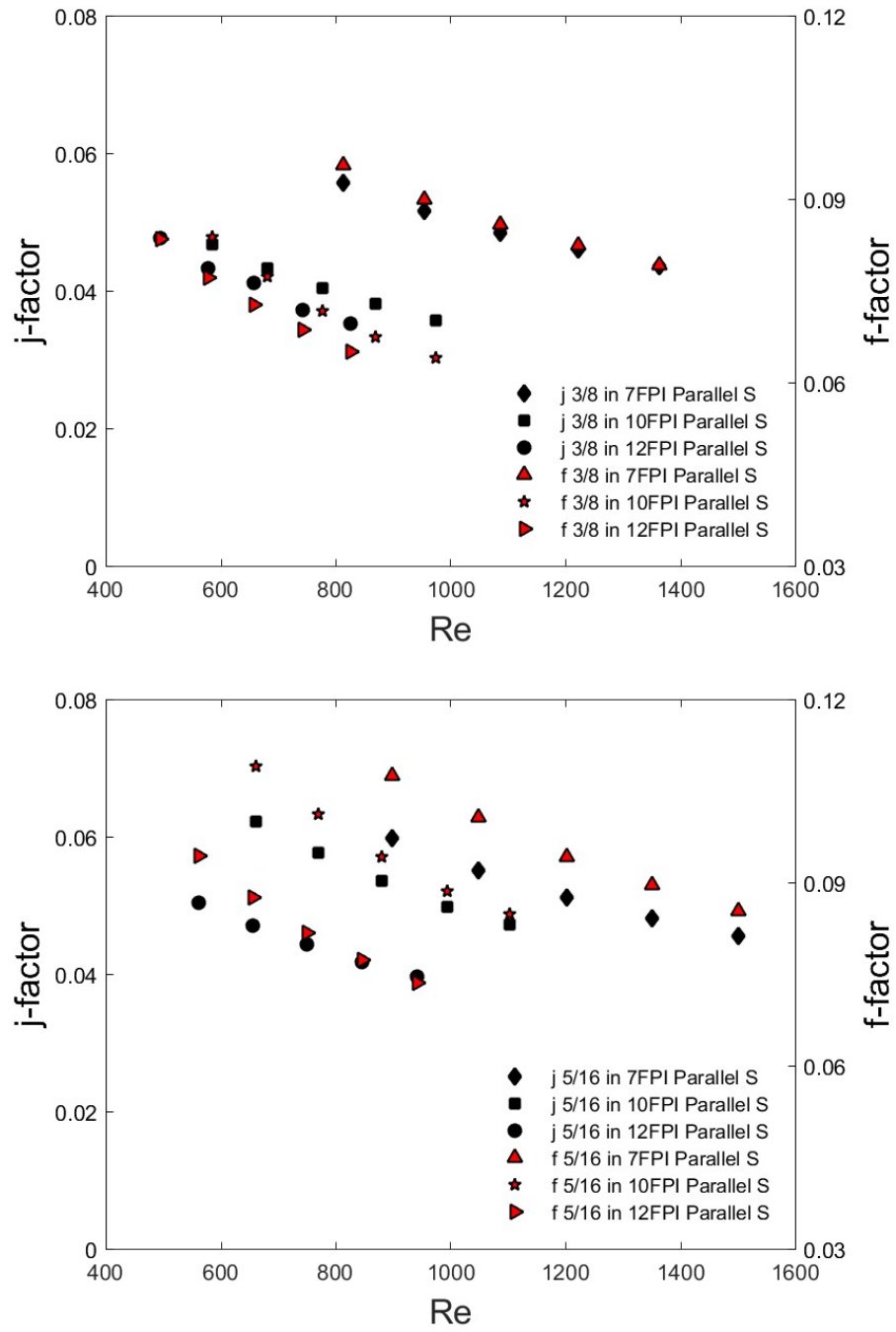
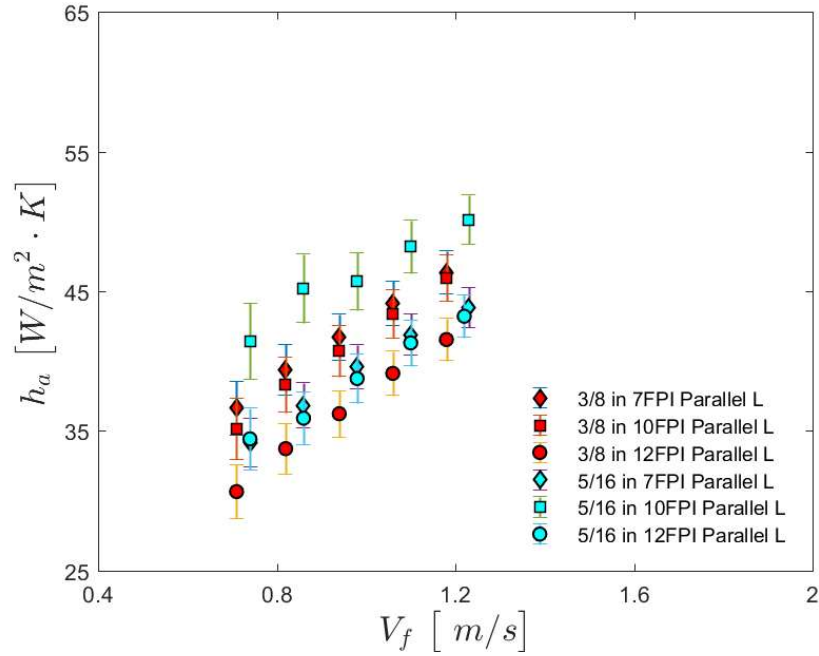


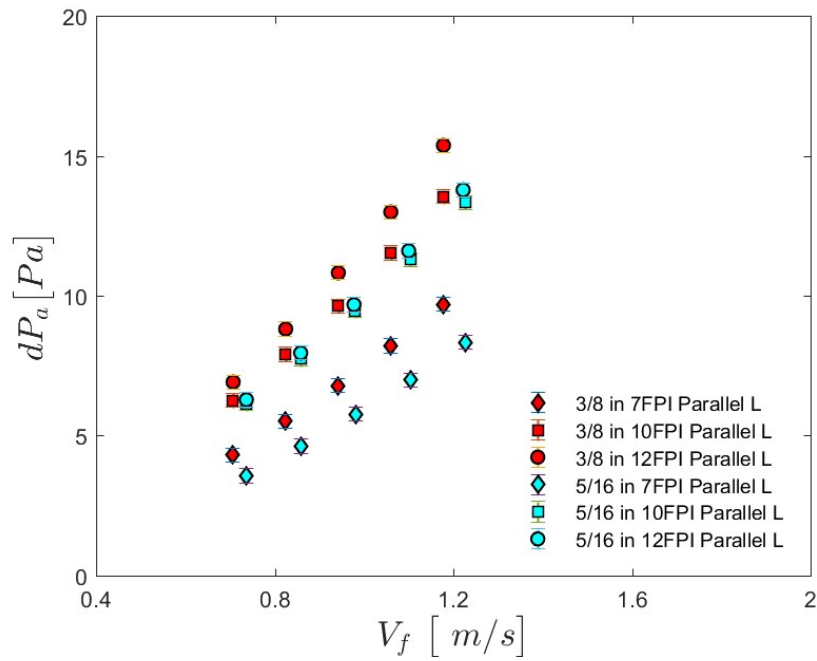
Figure 35:  $j$ -factor and  $f$ -factor 3/8 in (top) and 5/16 in (bottom) tube, short fin, parallel

#### 4.1.2. Parallel configuration long fin

The 10 fpi, 5/16 in tube heat exchanger has an even higher lead in heat transfer performance with respect to the other 5/16 in samples. It is unclear why the 7 fpi, 5/16 in tube heat exchanger performance is lower than the 10 fpi, 5/16 in, the trend is not seen in the 3/8 in tube heat exchangers. The 3/8 in heat exchangers follow the trends of all other spine fin samples with AHTC inversely proportional to fin density as seen in Figure 36.



**Figure 36: AHTC, parallel banks, long fin**



**Figure 37: Pressure drop, parallel banks, long fin**

The pressure drop data for these heat exchangers, as seen in Figure 37, shows a direct correlation between fin density and pressure drop. There is no measurable pressure drop difference between 10 and 12 fpi, 5/16 in tube. At 10 fpi there is little dependence on tube diameter. Figure 38 show typical trends on the 3/8 in samples. However, there is an almost indistinguishable behavior on the 5/16 in samples in 7 fpi and 10 fpi in terms of  $j$ -factor and  $f$ -factor. Explanation for this behavior might be as suggested in section 4.1.1.

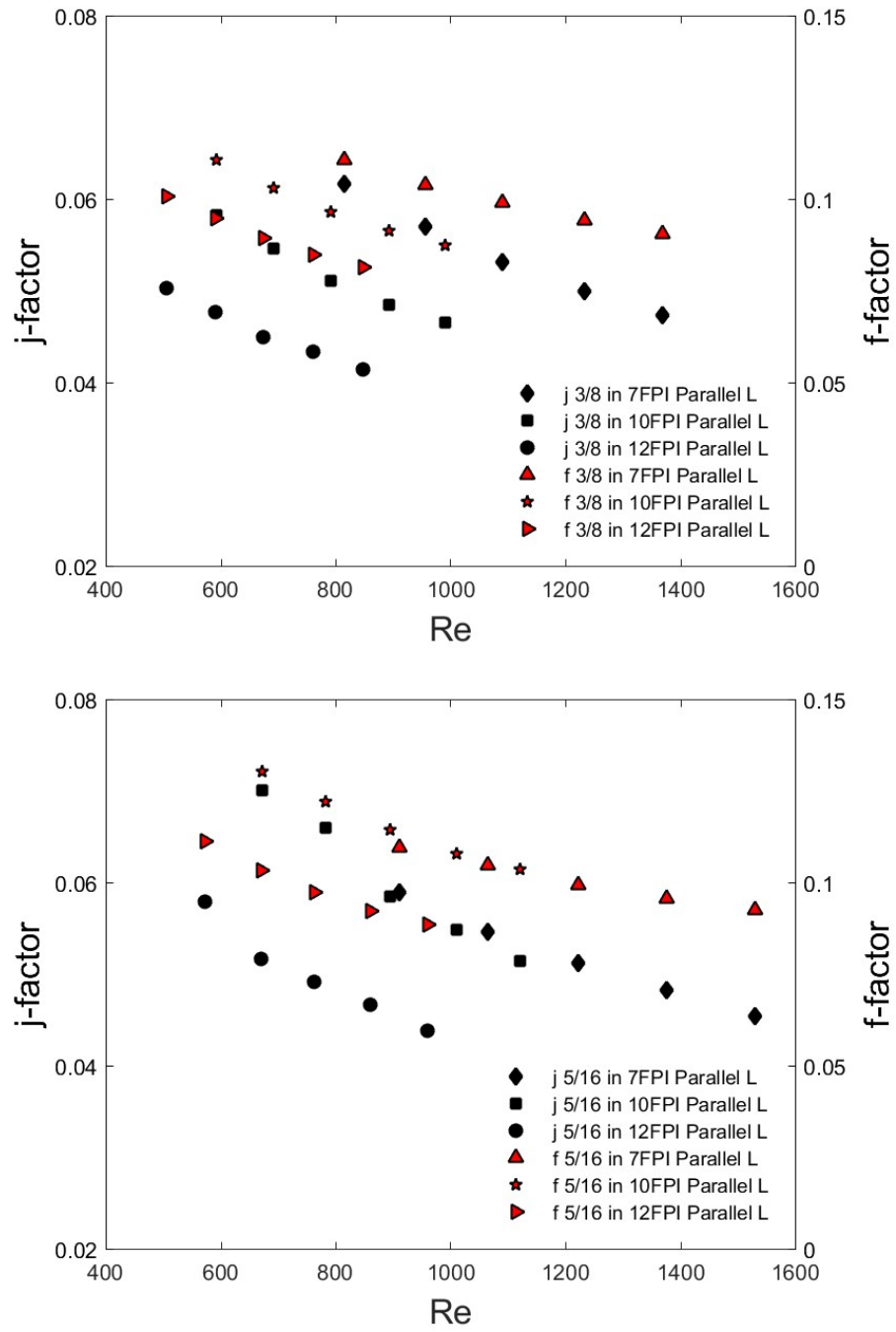
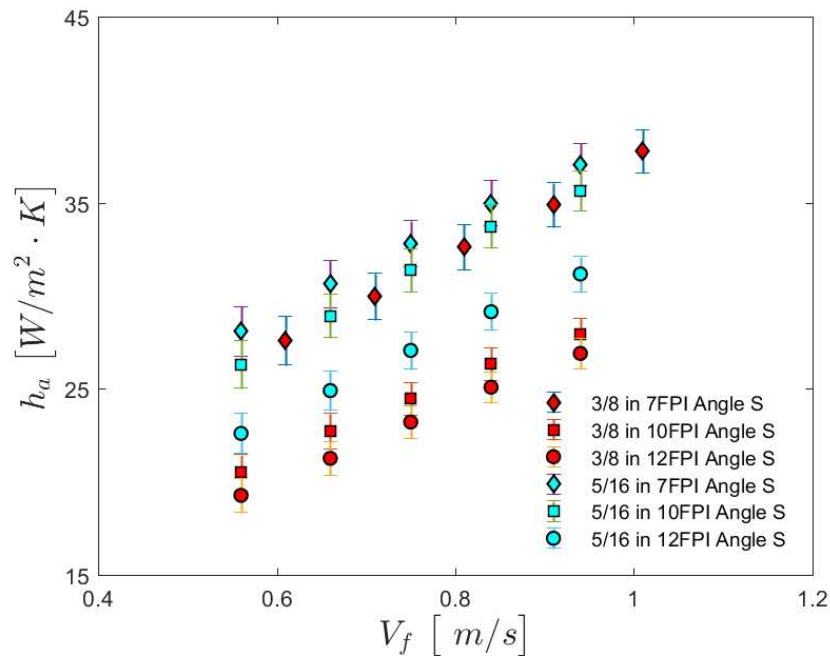


Figure 38: *j*-factor and *f*-factor 3/8 in (top) and 5/16 in (bottom) tube, long fin, parallel

#### 4.1.3. Angled configuration short fin

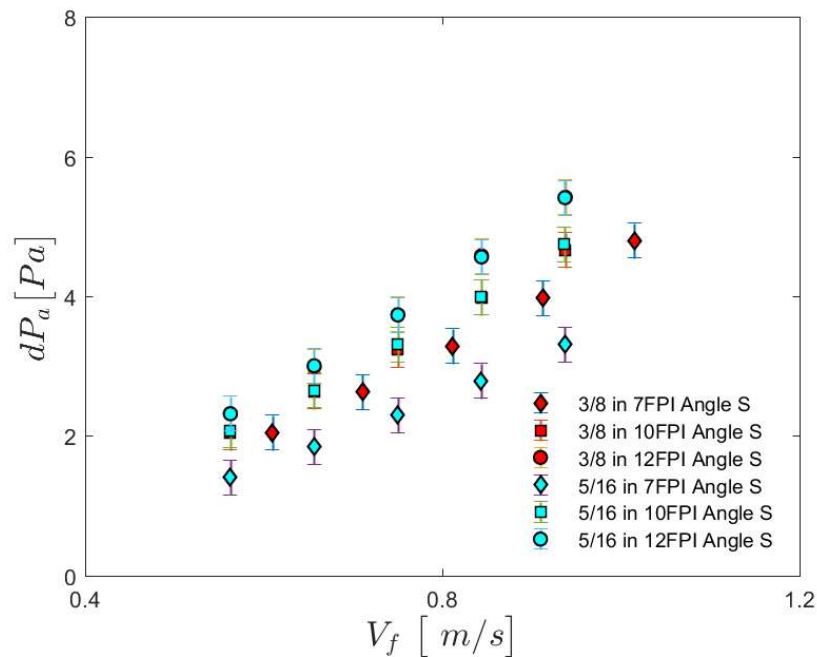
In the angled bank configuration the 5/16 in tubes continue to dominate. However, unlike in the parallel configurations the air-side heat transfer coefficient for the 7 fpi, 5/16 in tube samples is higher than the 10 fpi, 5/16 in tube samples, see Figure 39.

In the case of the 3/8 in tube samples, the 7 fpi heat exchanger is significantly better than the 10 fpi and 12 fpi heat exchangers. The 7 fpi, 3/8 in samples are from the machine that applied a hem to the fin reducing the fin height by 0.91mm. Therefore, the gap between tubes at the apex of the coil and the face area on this coil is smaller and air flow velocities higher.

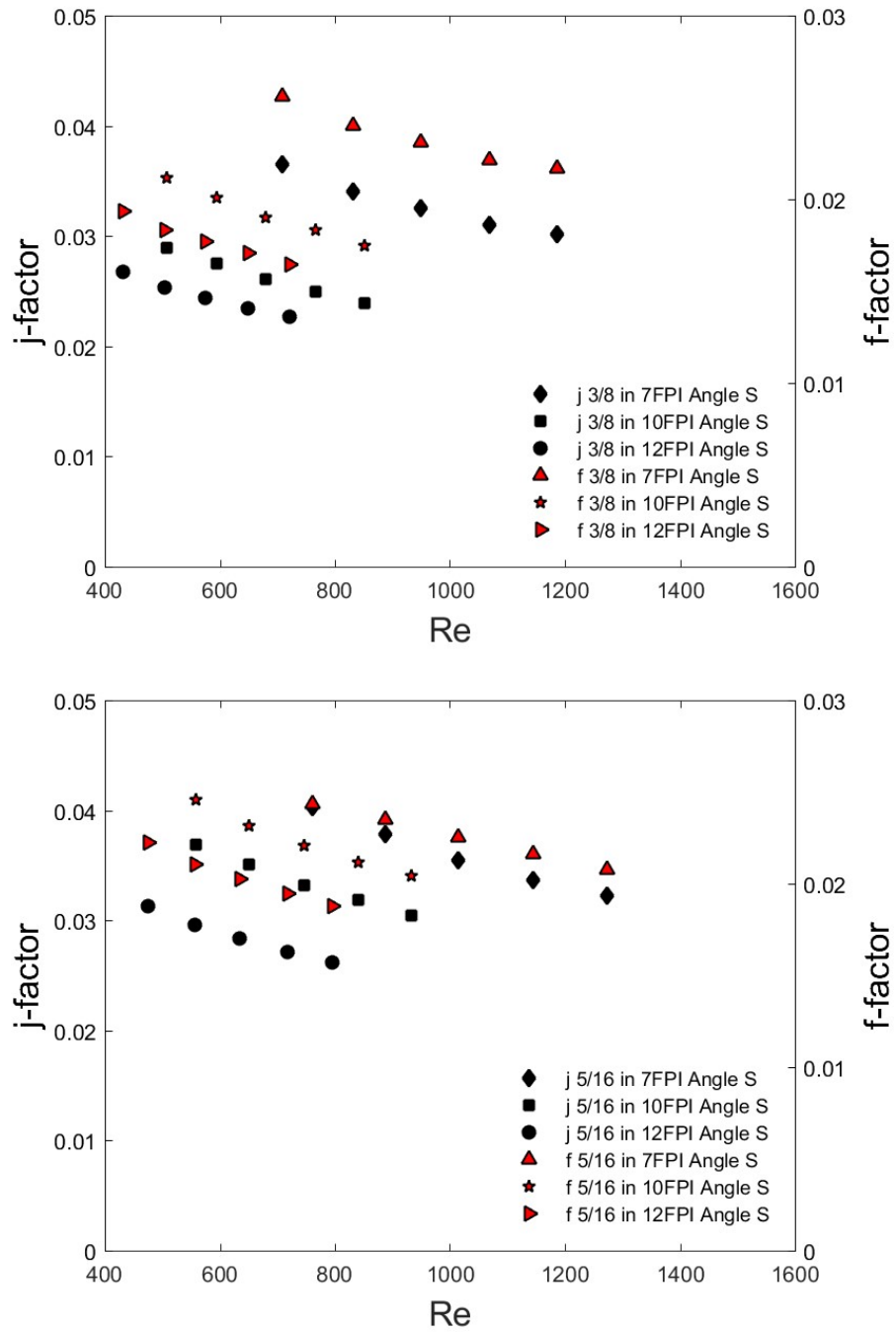


**Figure 39: AHTC, angled banks, short fin**

In terms of pressure drop there is a direct correlation between fin density and pressure drop as seen in Figure 40. The 12 fpi and 10 fpi samples in 3/8 in and 5/16 in tube diameters have the exact same pressure drop. This makes sense because the bulk of the pressure drop would be at the apex of the heat exchanger. In this part of the heat exchanger the free flow area between tubes at the apex would be the same regardless of tube diameter. This does not hold for the 7 fpi samples because the 3/8 in tube samples have shorter fins as explained before and this reduces free flow area. The trends are as expected in Figure 41.



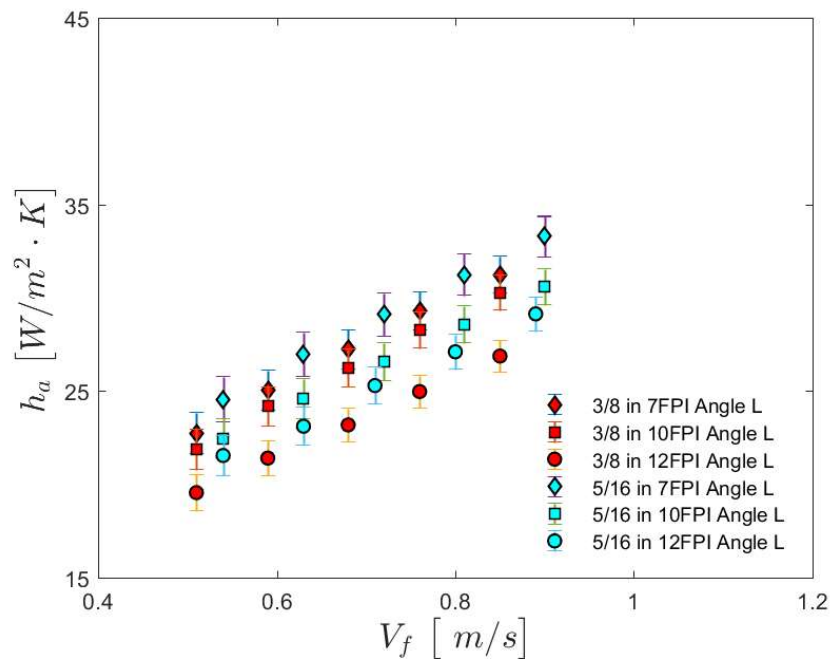
**Figure 40: Pressure drop, angled banks, short fin**



**Figure 41:  $j$ -factor and  $f$ -factor 3/8 in (top) and 5/16 in (bottom) tube, short fin, angled**

#### 4.1.4. Angled configuration long fin

The same heat transfer performance trends found with the short fin are seen with the long fin but with a more clear lead of the 7 fpi over the 10 fpi and 12 fpi in 5/16 in tube samples, see Figure 42. The trends on the 3/8 in tube samples are very similar to the trends on the parallel configuration. The 7 fpi tubes show small dependence on tube diameter over the range of flows tested. 10 fpi samples show even less dependence and almost matched performance at the lowest flows. 12 fpi shows dependence on tube diameter.

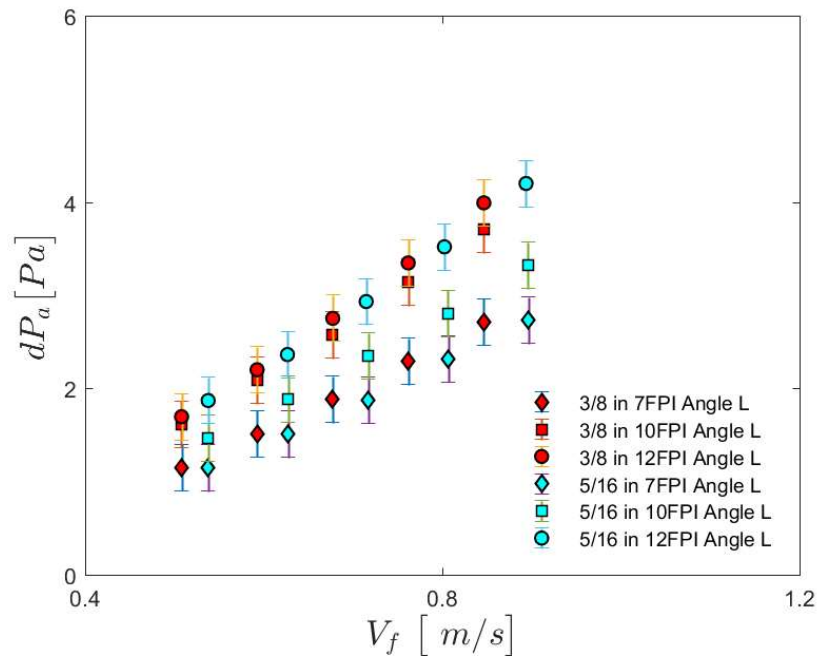


**Figure 42: AHTC, angled banks, long fin**

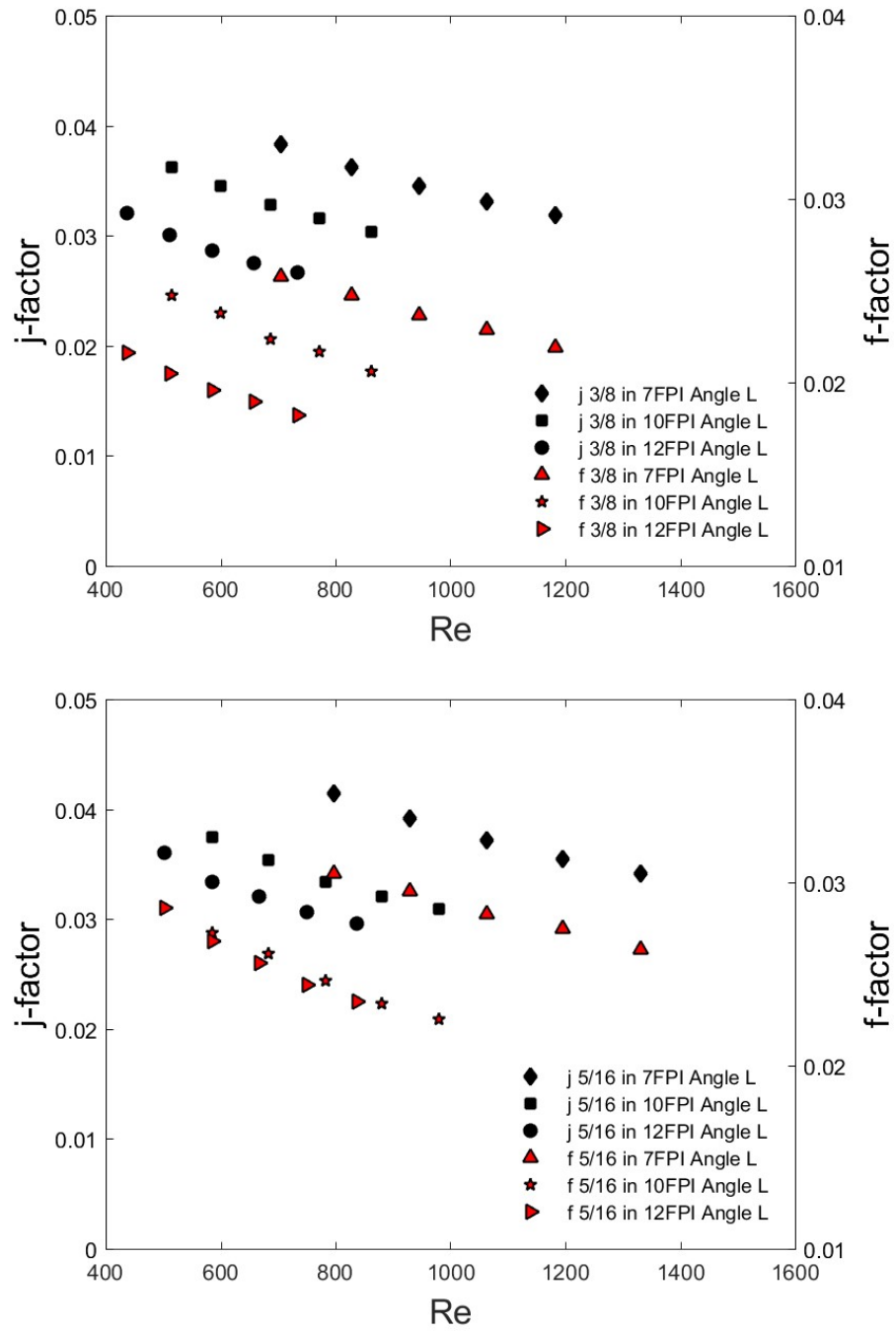
In terms of pressure drop (Figure 43), 7 fpi shows small dependence on tube diameter. Higher pressure drop, as expected, is seen on the 7 fpi 3/8in configuration heat exchanger. The 10 fpi showed the highest level of



dependence on tube diameter. The 10 fpi, 3/8 in sample has a pressure drop almost on par with the 12 fpi, 3/8 in sample. This is not the case with the 10 fpi and 12 fpi, 5/16 in samples, probably due to a larger than normal apex gap on the 10 fpi, 5/16 in heat exchanger. 12 fpi shows no dependence on tube diameter in terms of air-side pressure drop at the range of flows tested. Figure 44 shows the same performance trends seen in AHTC and pressure drop but in terms of  $j$ -factor and  $f$ -factor.



**Figure 43: Pressure drop, angled banks, long fin**

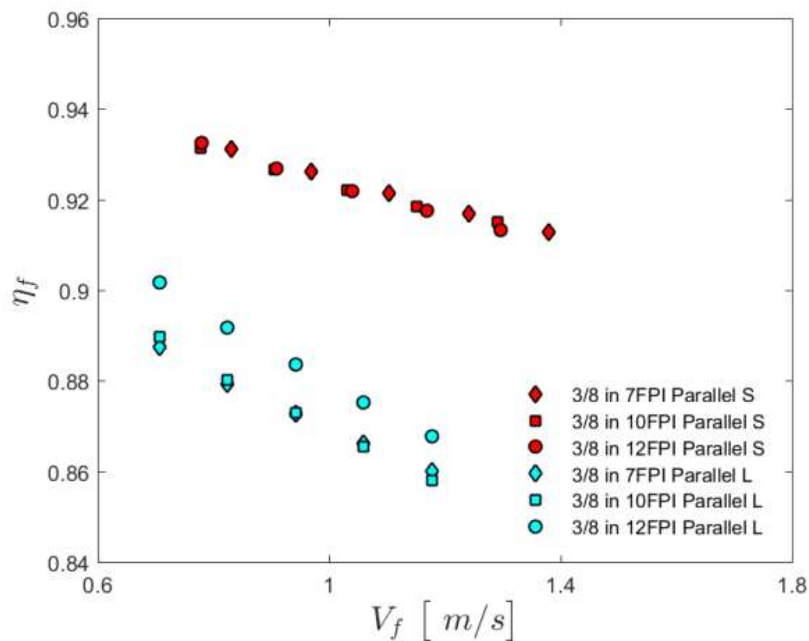


**Figure 44:  $j$ -factor and  $f$ -factor 3/8 in (top) and 5/16 in (bottom) tube, long fin, angled**

## 4.2. Fin Length Dependence

### 4.2.1. 3/8 inch diameter tube, parallel configuration

As expected fin efficiency is inversely proportional to fin length as shown in Figure 45. Heat transfer performance is dominated by the 7 fpi, short fin heat exchangers. 10 fpi samples' dependence on fin height is high throughout the flow ranges tested. There is little dependence on fin length at 12 fpi at the lower flows. See Figure 46. Air-side pressure drop is directly proportional to fin density and highest for the shorter fin. It shows however, no dependence on fin length at 10 fpi. The highest pressure drop, as expected is on the highest density material Figure 47. Figure 48 shows the same performance trends.



**Figure 45: Fin efficiency short Versus Long fin, parallel configuration**

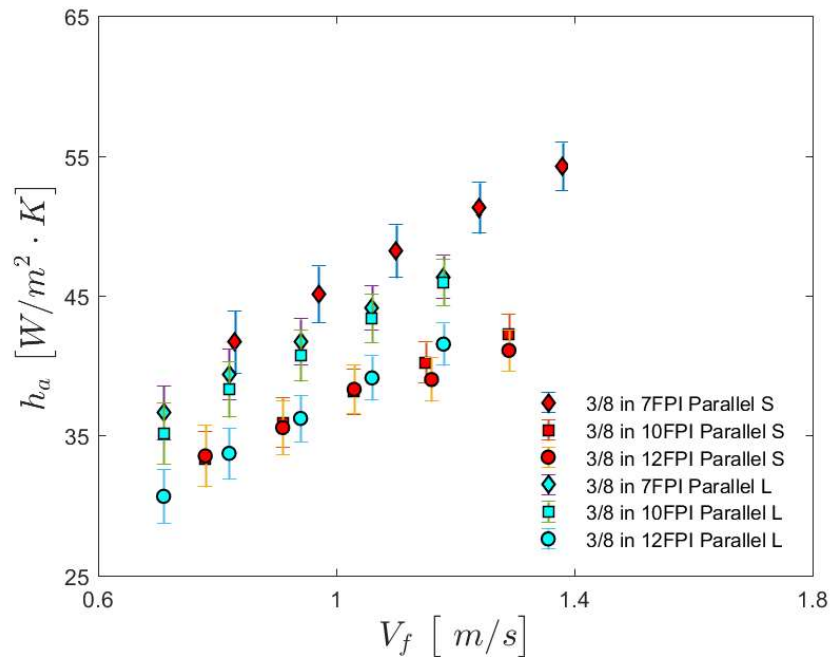


Figure 46: AHTC, parallel banks, short and long fin, 3/8 in

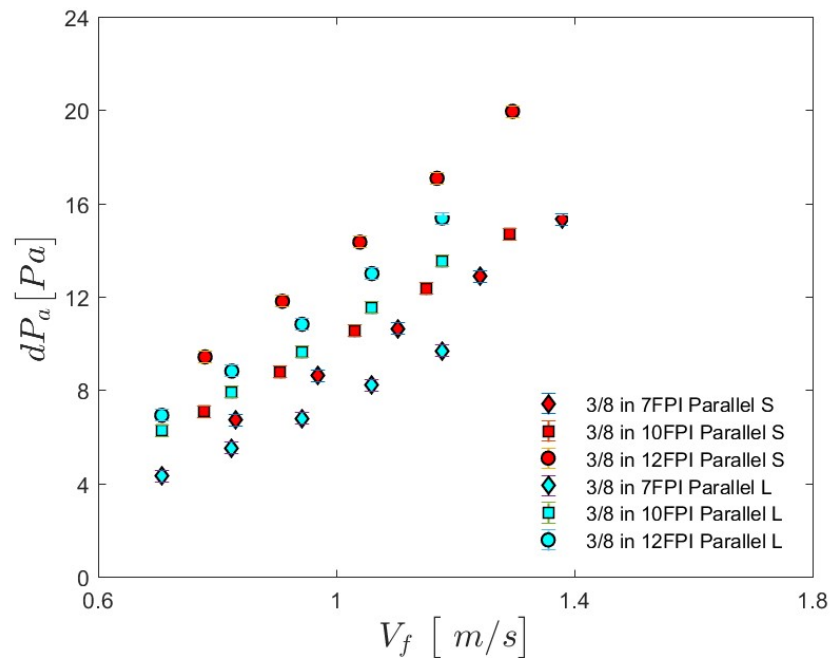
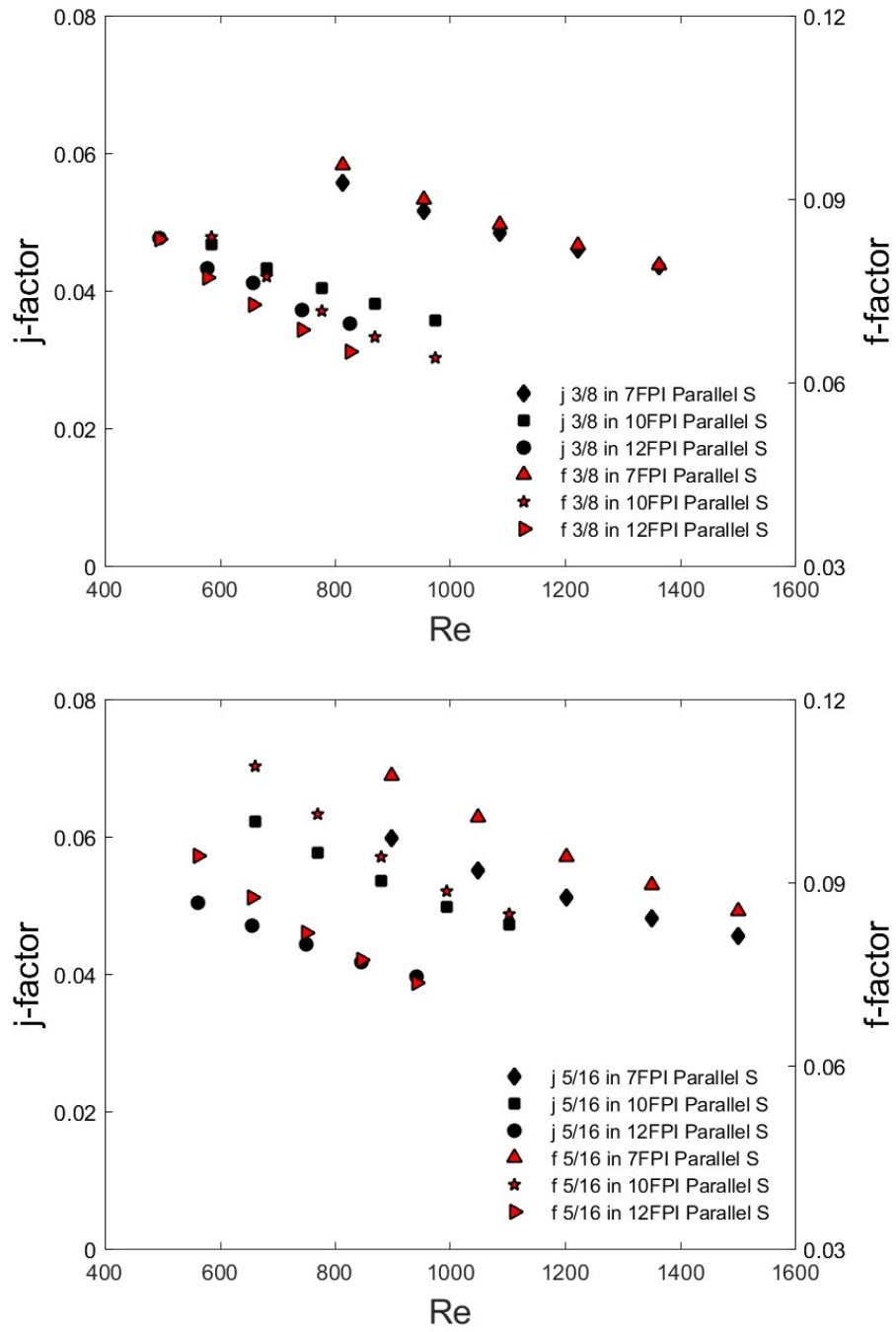


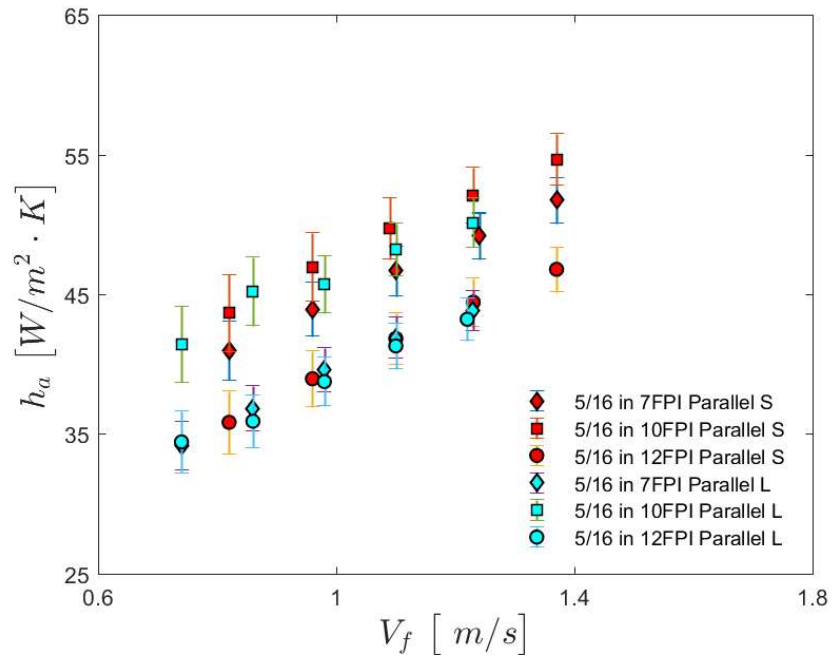
Figure 47: Pressure drop, parallel banks, short and long fin, 3/8 in



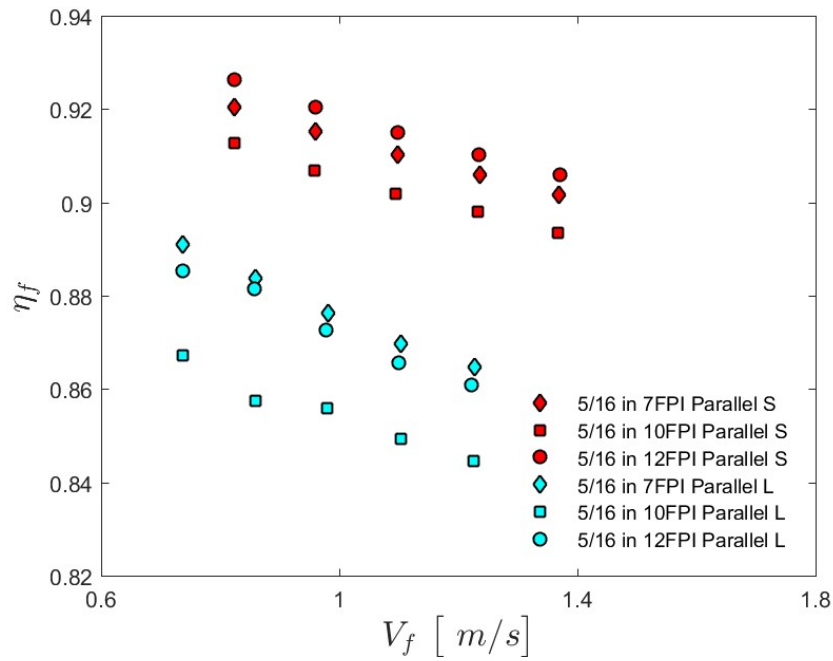
**Figure 48:  $j$ -factor and  $f$ -factor 3/8 in short (top) and long (bottom) fin, parallel**

#### 4.2.2. 5/16 inch diameter tube, parallel configuration

Short fin dominates heat transfer performance, see Figure 49. The 10 fpi samples perform significantly better than their 7 fpi and 12 fpi counterparts. Fin efficiency is highest for the shorter fin material as seen in Figure 50.

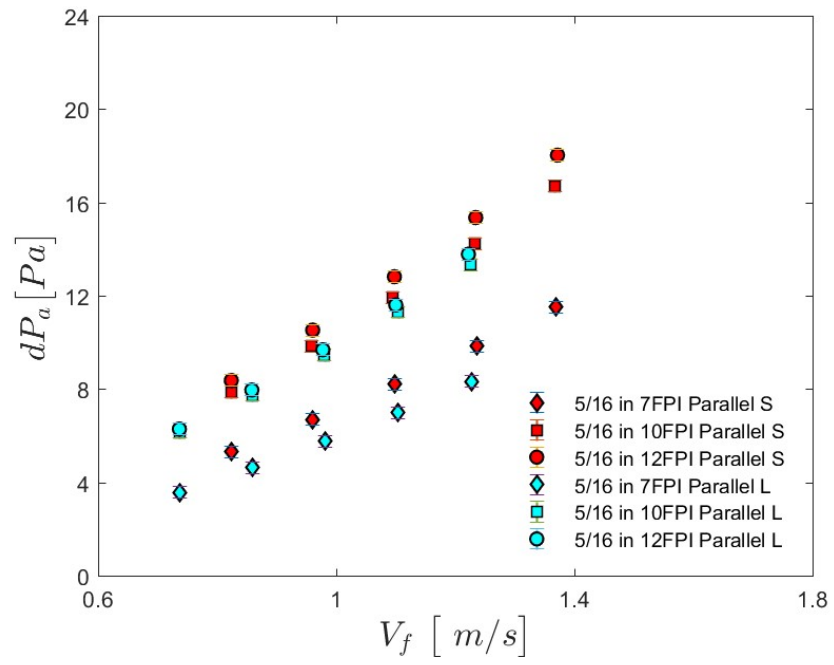


**Figure 49: AHTC, parallel banks, short and long fin, 5/16 in**



**Figure 50: Fin efficiency short Versus Long fin, parallel configuration**

Pressure drop shows very small dependence on fin length for 10 fpi samples. 12 fpi samples are more dependent on tube diameter and the dependence increases with increasing flows. Pressure drop is significantly lower for 7 fpi samples but there is small dependence on fin height. As expected, 7 fpi short fin material has higher pressure drop than 7 fpi, long fin material, see Figure 51. As mentioned before, Figure 52 (bottom) shows the indistinguishable behavior on the 5/16 in, long fin samples in 7 fpi and 10 fpi in terms of  $j$ -factor and  $f$ -factor.



**Figure 51: Pressure drop, parallel banks, short and long fin, 5/16 in**



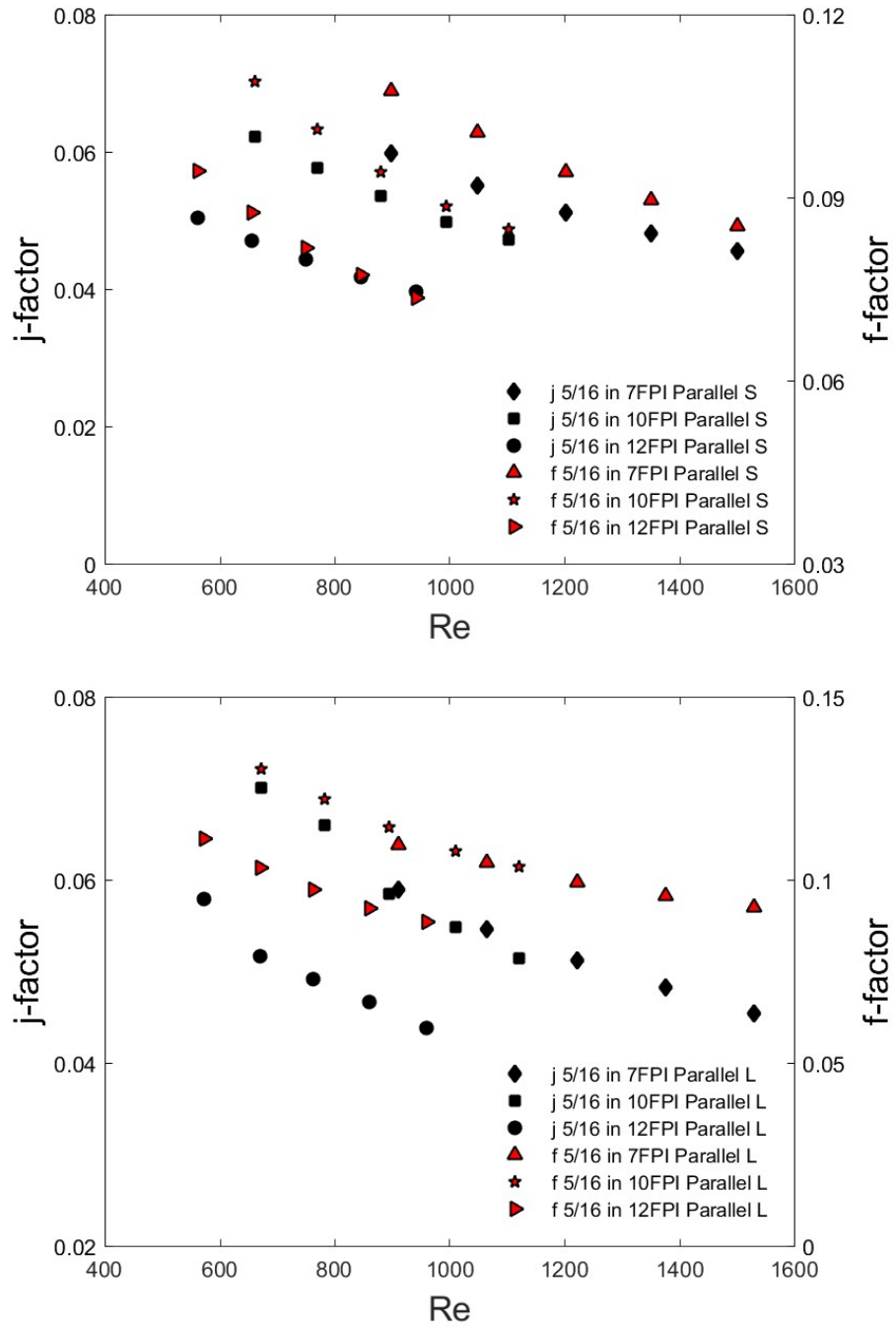
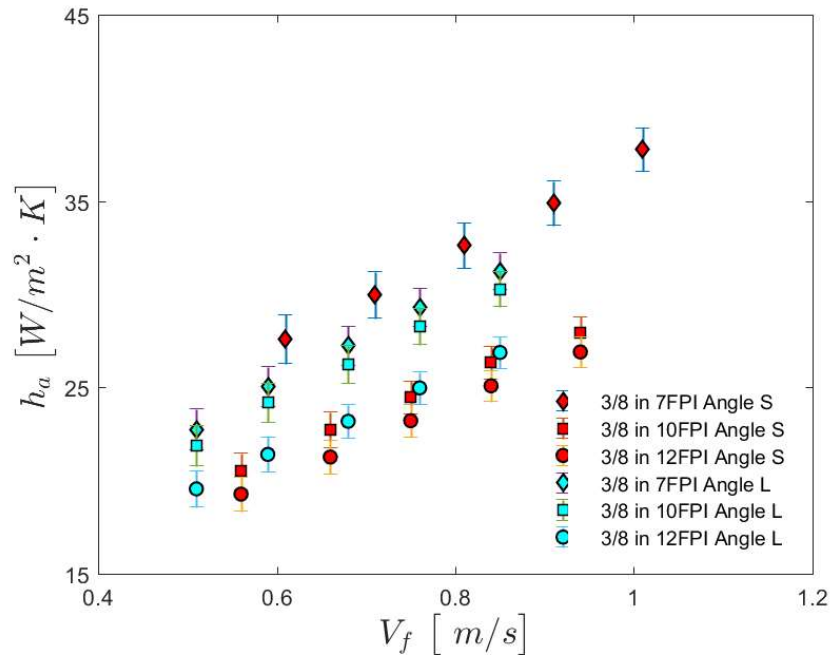


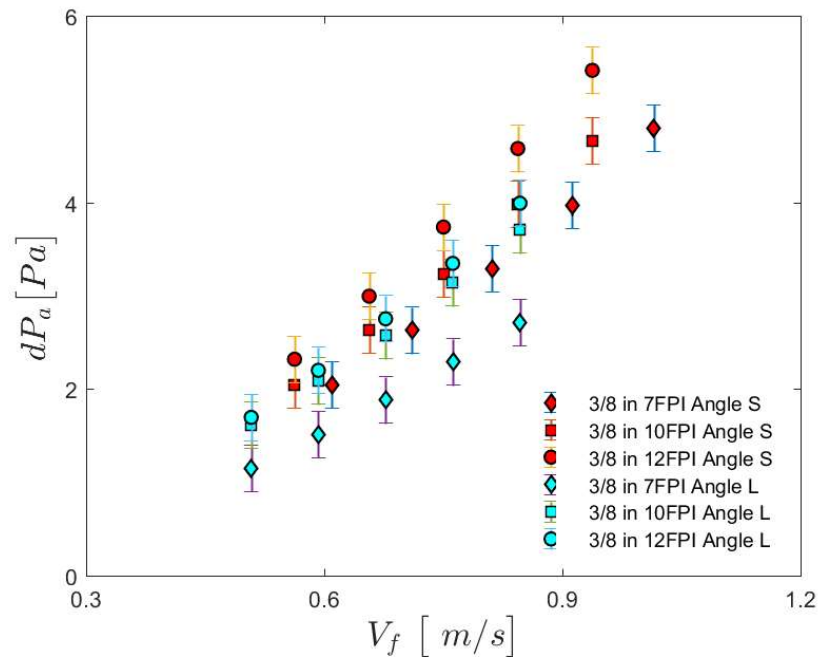
Figure 52:  $j$ -factor and  $f$ -factor 5/16 in short (top) and long (bottom) fin, parallel

#### 4.2.3. 3/8 inch diameter tube, angled configuration



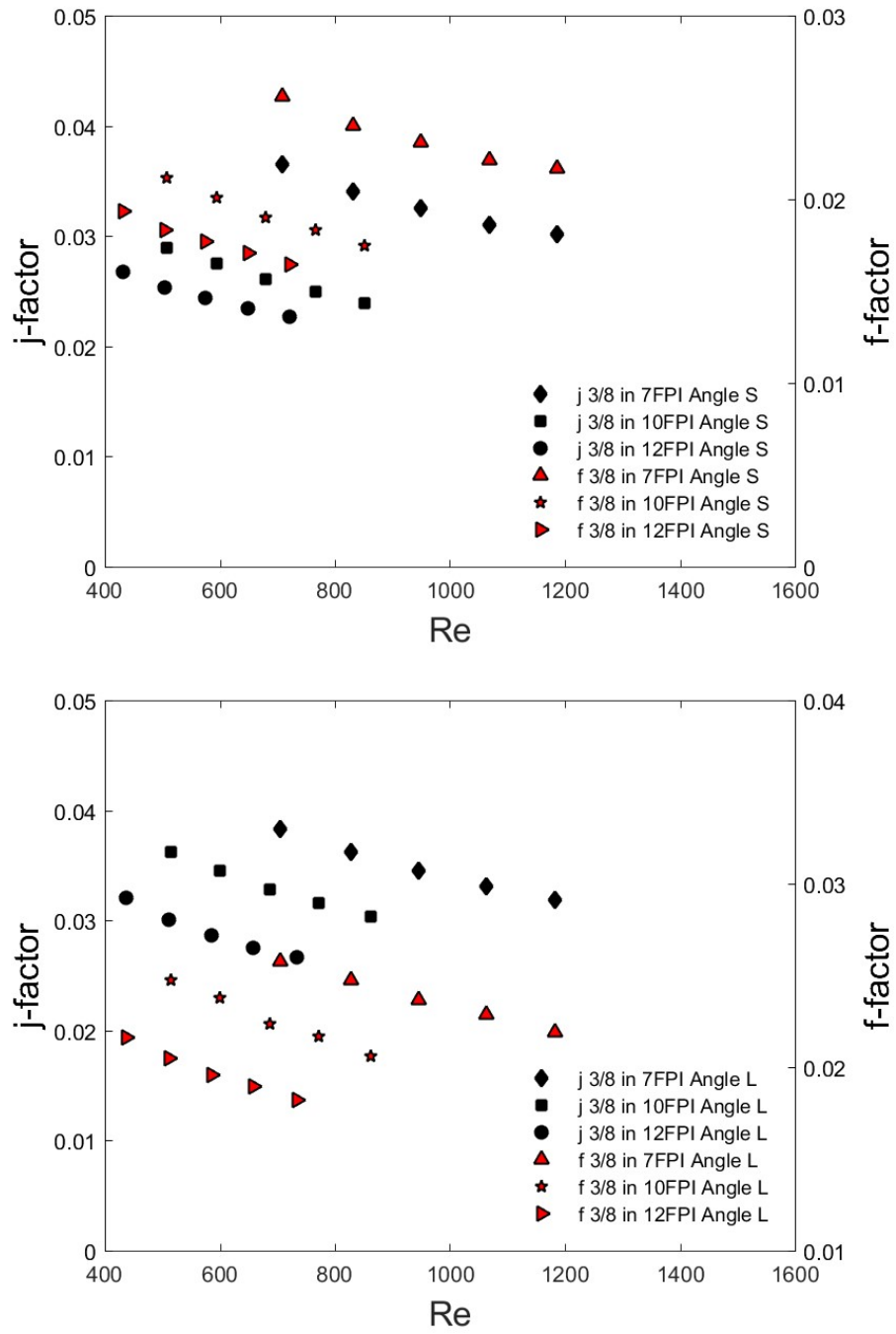
**Figure 53: AHTC, angled banks, short and long fin, 3/8 in**

In terms of heat transfer performance, the same trends observed for the parallel configuration apply to the angled configuration while the dependence on fin height for 7 fpi is lower. The dependence of 10 fpi on fin height is significant; performance is notably higher for the long fin a trend that is not seen in the 3/8 in samples. At 12 fpi there is very small dependence on fin height and it decreases with increasing flow.



**Figure 54: Pressure drop, angled banks, short and long fin, 3/8 in**

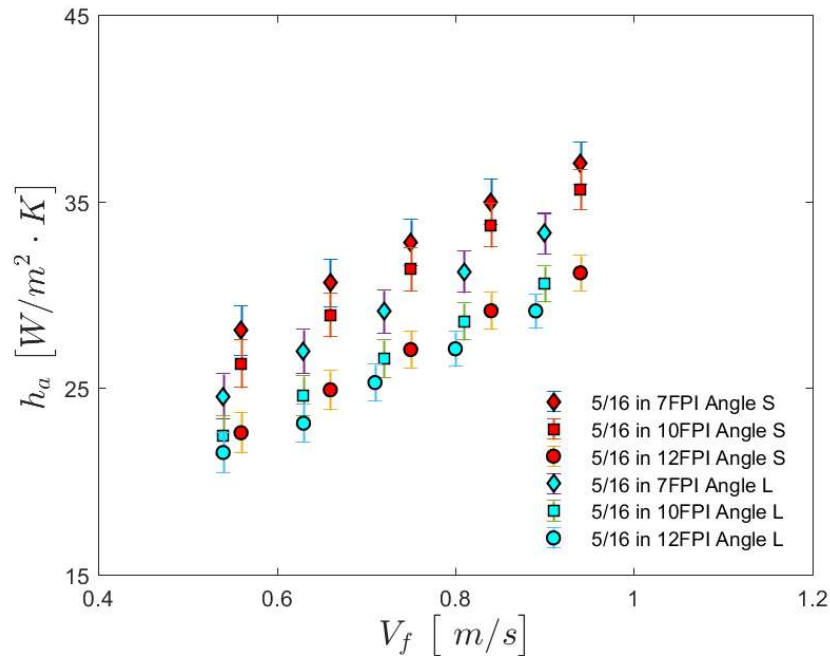
In terms of pressure drop; the 10 fpi samples show no dependence on fin height at the lower flows but the curves diverge at higher flows. The 12 fpi is dependent on fin height and that dependence increases as face velocity increases. The same applies to 7 fpi and to a higher extent.



**Figure 55:  $j$ -factor and  $f$ -factor 3/8 in short (top) and long (bottom) fin, angled**

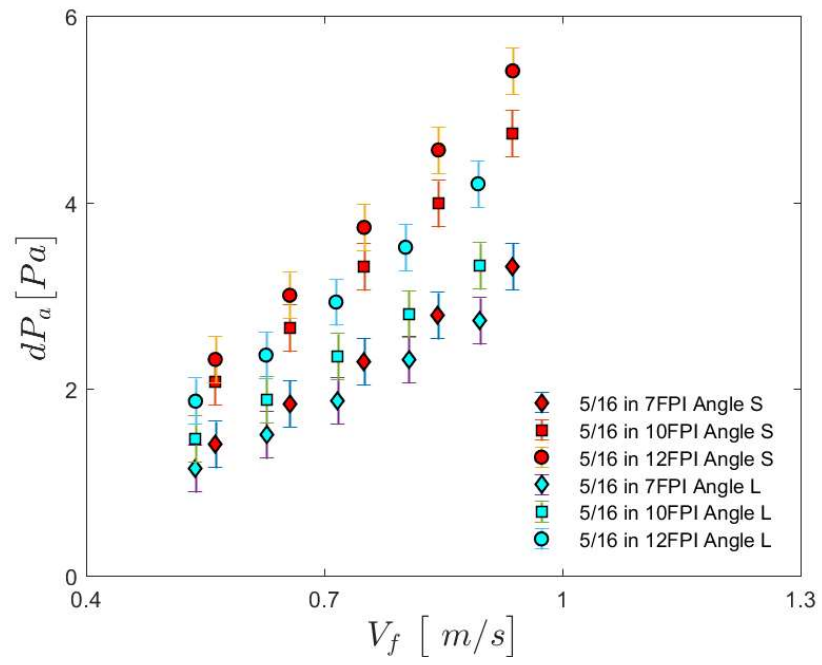
#### 4.2.4. 5/16 inch diameter tube, angled configuration

Heat transfer is dominated by the shorter fin. There is a dependence on fin height at all flows tested but the dependence is highest for 10 fpi and lowest for 12 fpi. 7 fpi's dependence is somewhere in between. See Figure 56.

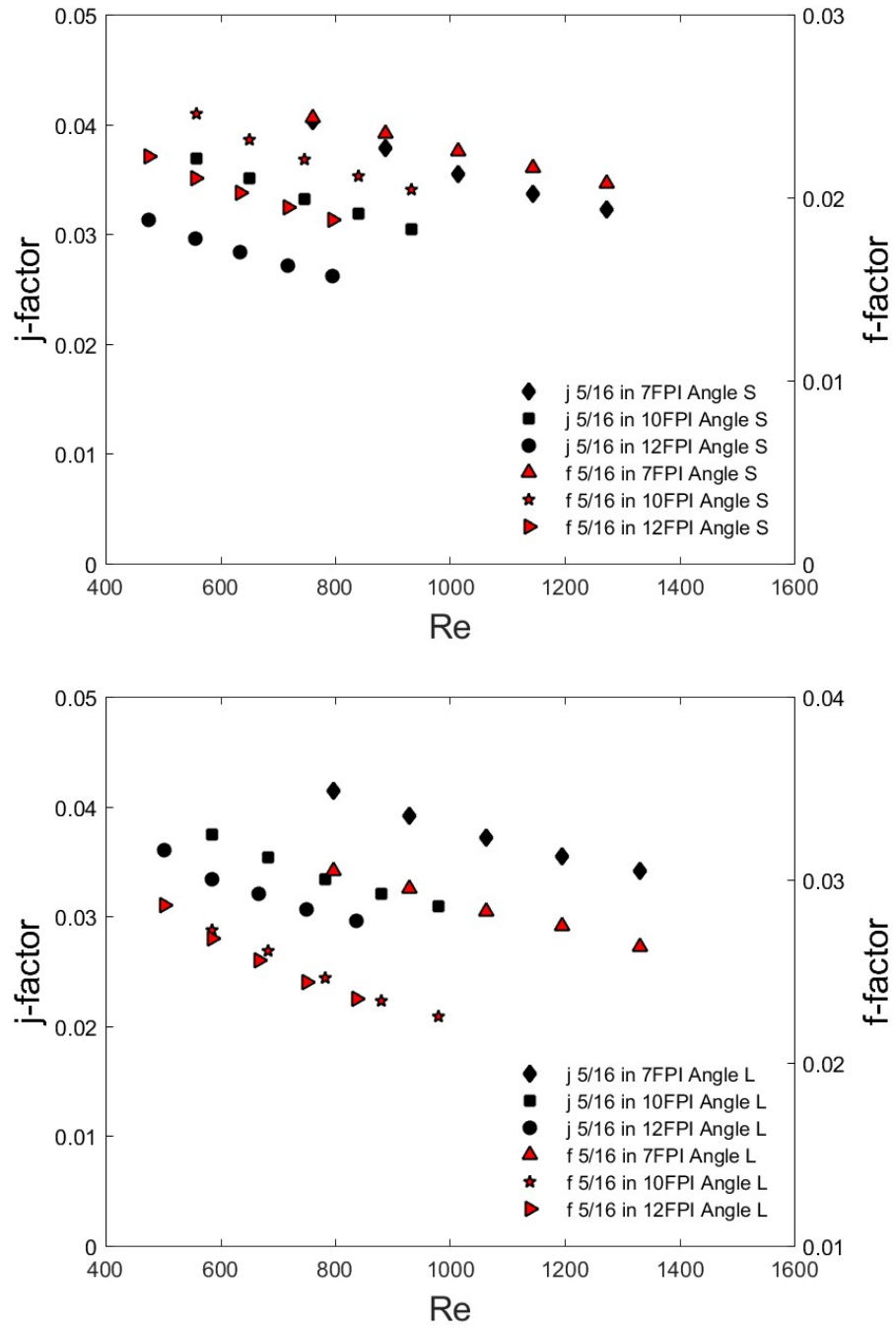


**Figure 56: AHTC, parallel banks, short and long fin, 5/16 in**

In terms of pressure drop, there is dependence at all flows tested as seen in Figure 57. 10 fpi shows the highest dependence with an increasing trend as face velocity increases. 7 fpi shows the same trend but the dependence is small. The same trend can be observed for 12 fpi.



**Figure 57: Pressure drop, parallel banks, short and long fin, 5/16 in**



**Figure 58:  $j$ -factor and  $f$ -factor 5/16 in short (top) and long (bottom) fin, angled**

### 4.3. Overall Performance

#### 4.3.1. 7 fpi

In general, in terms of AHTC parallel configurations are better performers than angled configurations as seen in Figure 59. Face velocities are higher at a given airflow rate. Not surprisingly, air-side pressure drop is significantly higher for these heat exchangers, see Figure 60.

Performance is led by the parallel 5/16 in and 3/8 in heat exchangers; the 3/8 in performance appears to be superior at higher flows but this comes at the expense of much higher air-side pressure drop. The 5/16 in angled sample is very competitive and at the mid-range of flows tested it matches the performance of the 5/16 in parallel heat exchanger which has a higher air-side pressure drop.

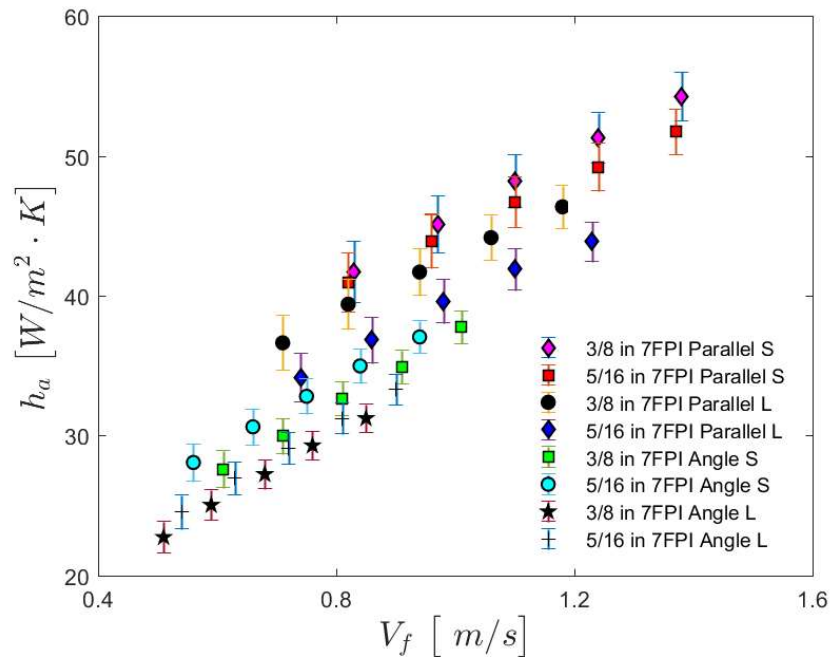
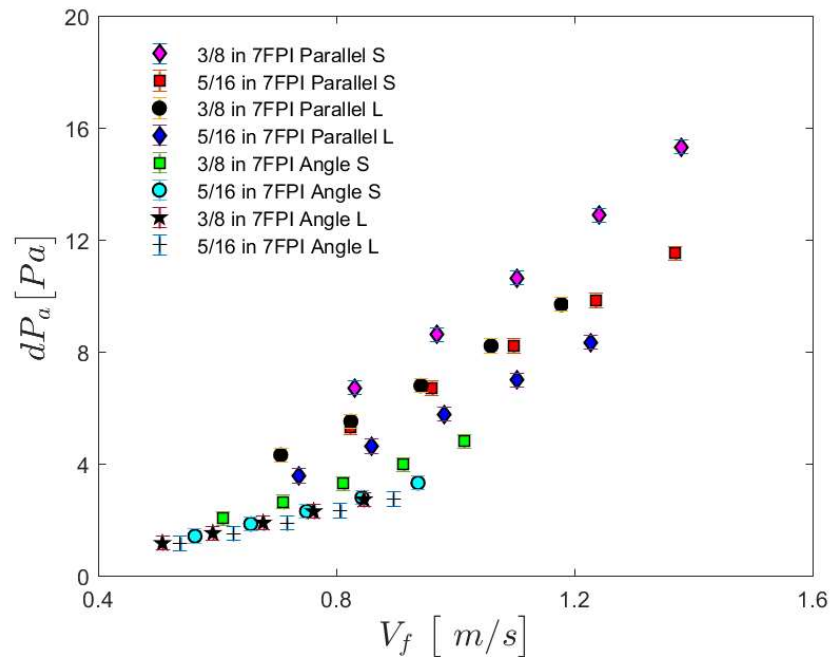


Figure 59: AHTC, 7 fpi





**Figure 60: Pressure drop, 7 fpi**

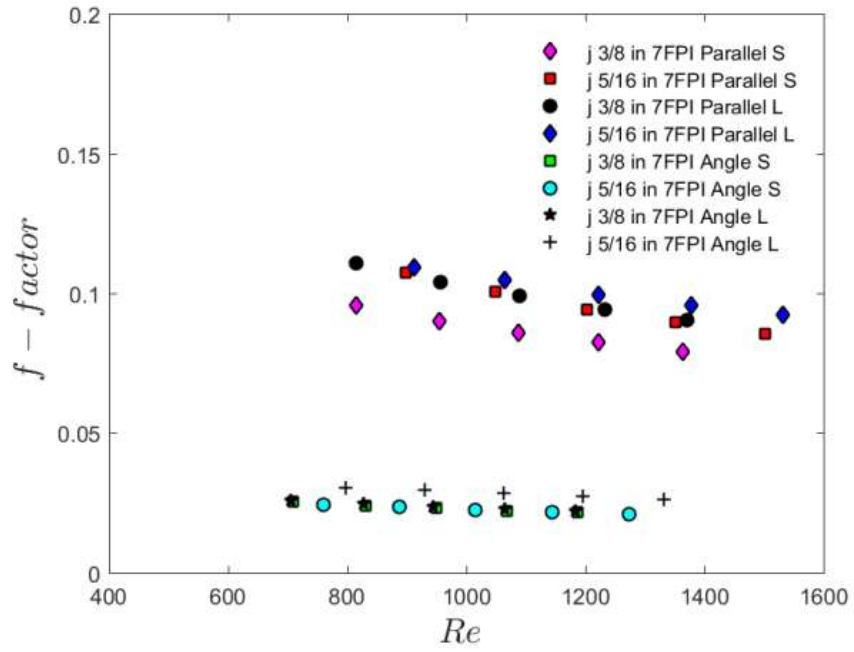
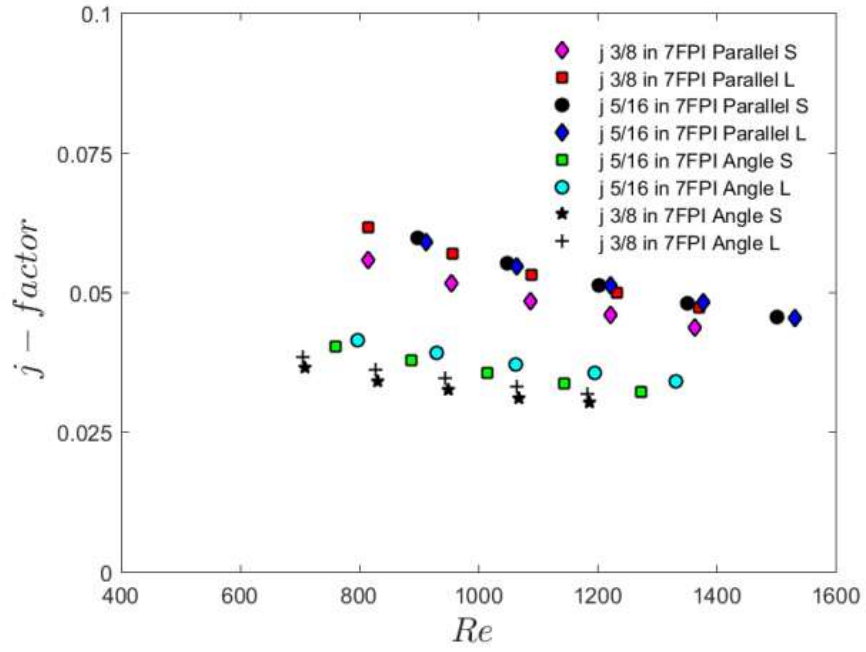


Figure 61: 7 fpi  $j$ -factor (top) and  $f$ -factor (bottom)

#### 4.3.2. 10 fpi

For heat transfer performance 5/16 in, short fin leads all heat exchangers with 5/16 in, long fin following closely, see Figure 62. The 3/8 in, long fin leads the 3/8 in samples evenly through the range of flows tested. There is virtually no difference between the 3/8 in and 5/16 in, angled configurations with short and long fins. This is dramatically different when comparing the same tube diameters in the parallel configuration. In those cases the 5/16 in, parallel configuration with long fin is a better performer. As with the 7 fpi heat exchangers, parallel configurations are better performers than angled configurations because face velocities are higher. Air-side pressure drop is significantly higher for these heat exchangers. 5/16 in, short fin configurations are also superior to their 3/8 in counterparts.

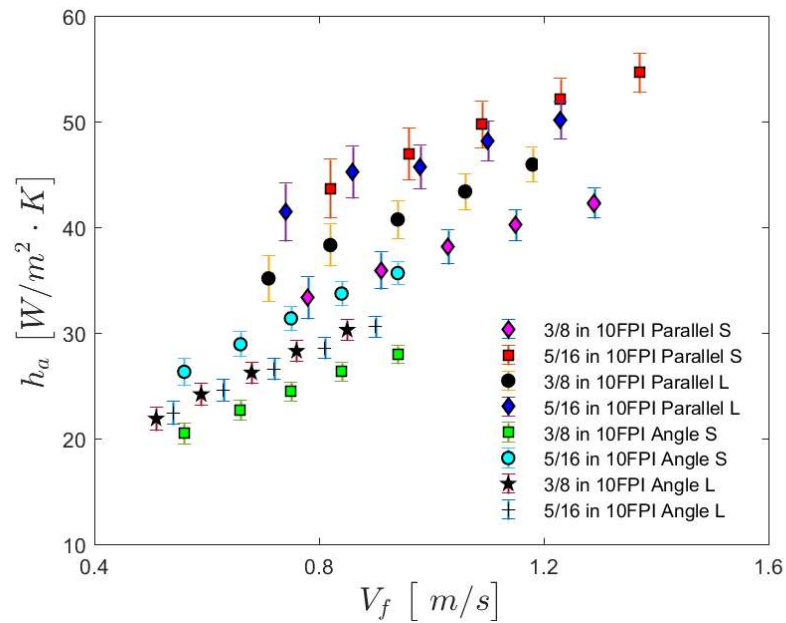
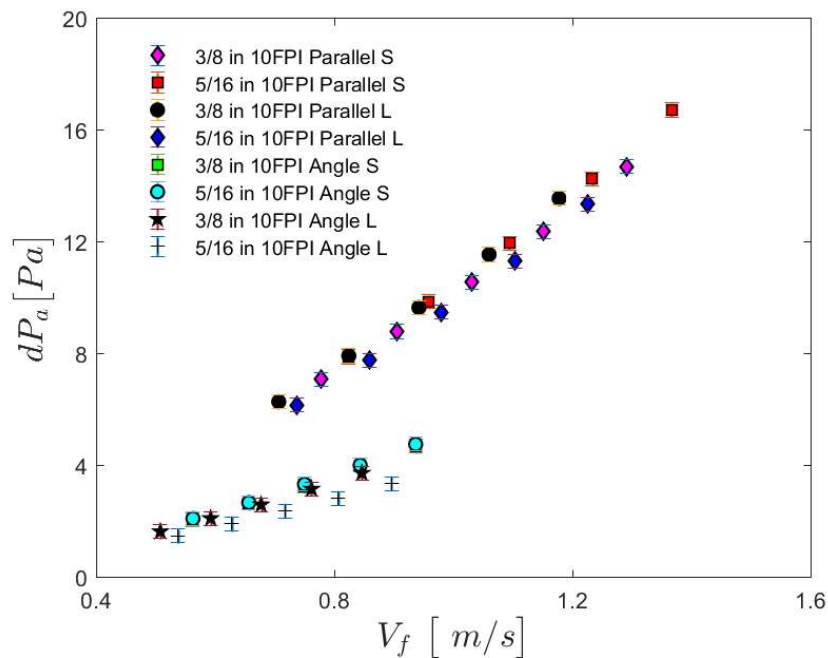


Figure 62: AHTC, 10 fpi

The 5/16 in, angled configuration with short fins matches the performance of the 3/8 in, parallel configuration with short fins.

In terms of air-side pressure drop selection is easy. Parallel configuration heat exchangers have nearly identical performance. The same can be said of the angled configuration heat exchangers. Their pressure drop is significantly lower. The 5/16 in angled configuration shows the lowest air-side pressure drop and the trend indicates that the difference might be more noticeable at higher face velocities. These trends are presented in Figure 63. The plot of  $j$ -factor and  $f$ -factor in Figure 64 shows the same trends discussed but with more granularity in terms of friction.



**Figure 63: Pressure drop, 10 fpi**

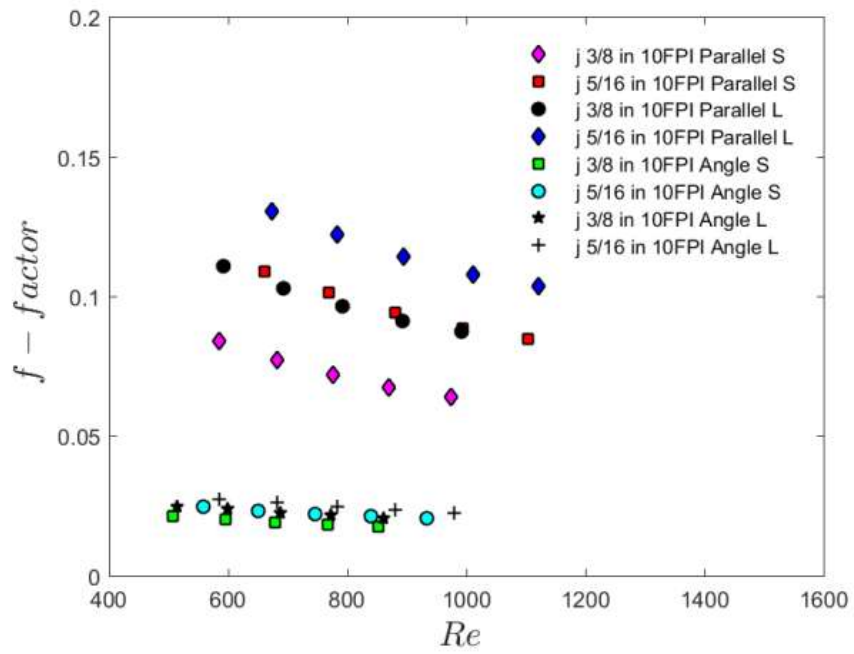
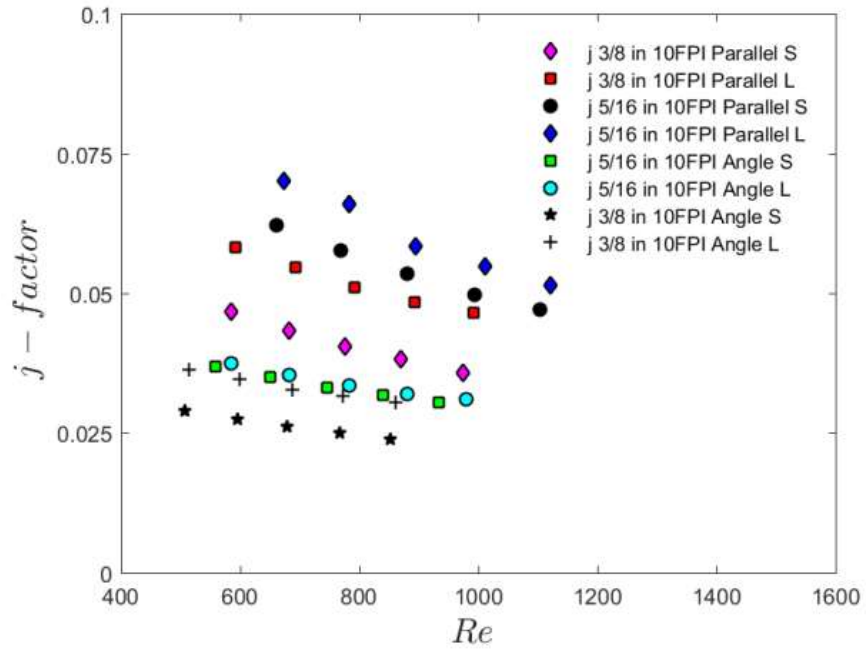
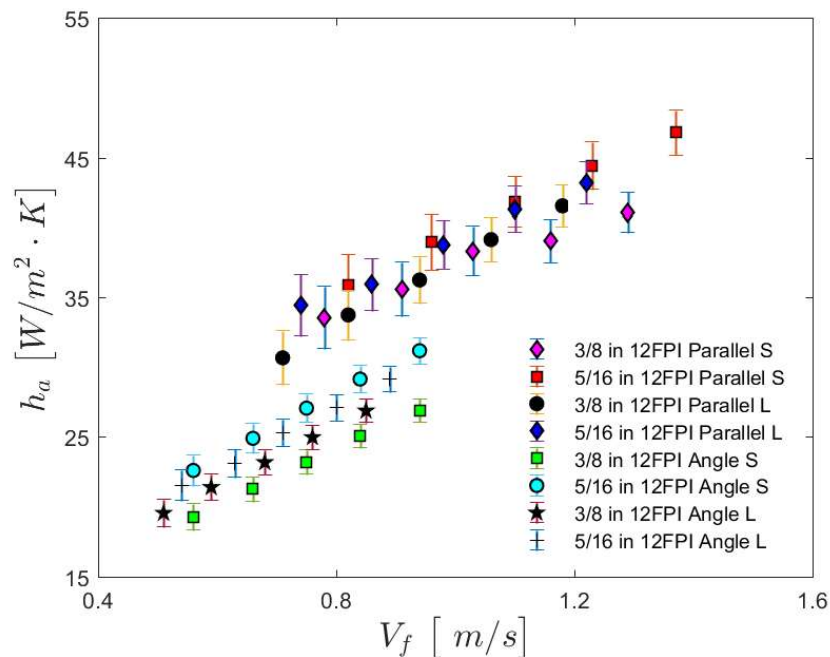


Figure 64: 10 fpi  $j$ -factor (top) and  $f$ -factor (bottom)

#### 4.3.3. 12 fpi

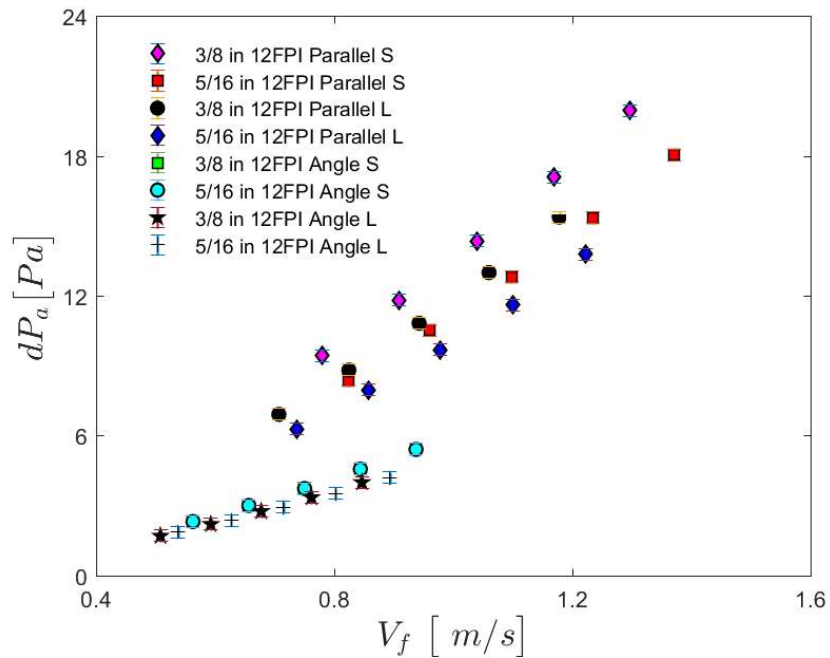
Heat transfer coefficient trends are very similar to the 10 fpi samples. However, the performance of the 3/8 in, parallel configuration with short fins and long fins are nearly identical to the 5/16 in, parallel configuration with long fins. See Figure 65. As with the 7 fpi and 10 fpi heat exchangers, parallel configurations are better performers than angled configurations.



**Figure 65: AHTC, 12 fpi**

In terms of pressure drop there is some distinction between the parallel configurations. Samples with 3/8 in tubes in short and long fin heights having higher pressure drop than their 5/16 in counterparts. The trend shows that the distinction will disappear at lower flows. See Figure 66.

The angled configurations show identical pressure drop with the exception, perhaps, of the 5/16 in, long fin sample. Like its 10 fpi counterpart it has lower air-side pressure drop and the difference seems to increase as flows get larger. Figure 67 shows the same trends discussed. There is more performance differentiation with the parallel configuration samples



**Figure 66: Pressure drop, 12 fpi**

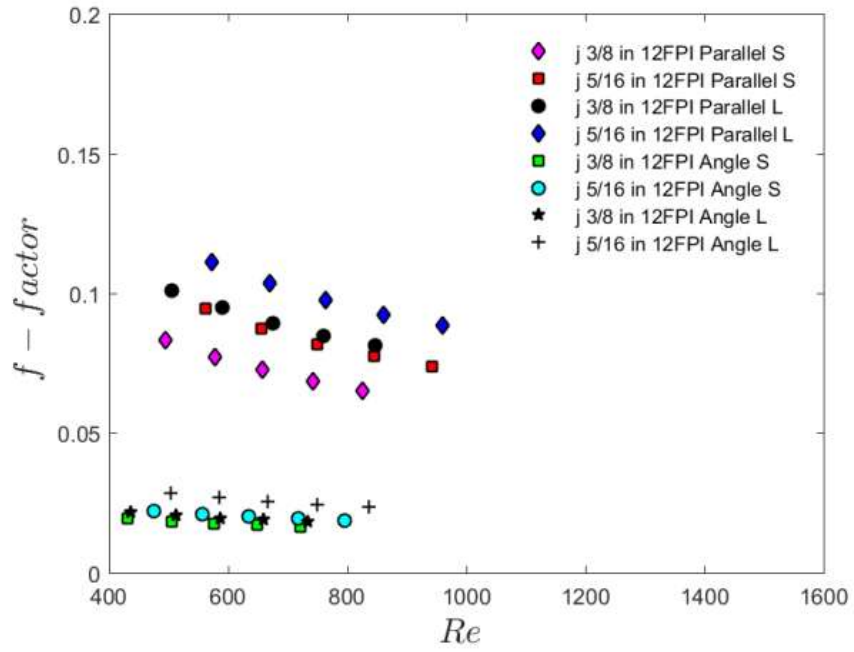
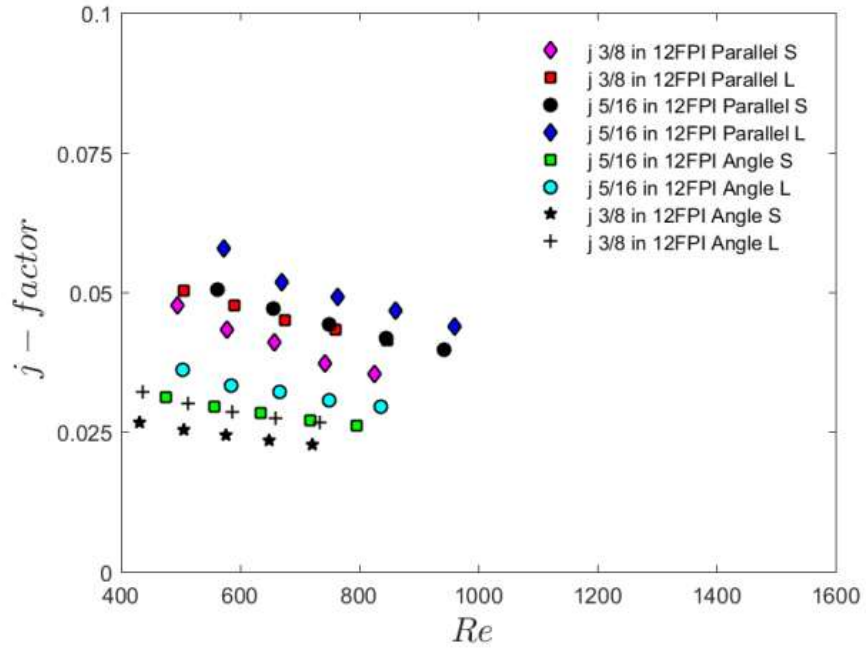


Figure 67: 12 fpi  $j$ -factor (top) and  $f$ -factor (bottom)



## 5. Performance Correlations

The data has been correlated using a multiple linear regression method. The general form of the equations initially used for heat transfer performance and pressure drop are shown in equations (38) and (39).

$$j = C_1 Re^{C_2} \left( \frac{D_f}{F_p} \right)^{C_3} \quad (38)$$

$$f = C_4 Re^{C_5} \left( \frac{D_f}{F_p} \right)^{C_6} \quad (39)$$

Where  $D_f$  and  $F_p$  are finned diameter and fin density respectively. These correlation forms were able to capture the variation of the data with R-squared, R-squared adjusted and R-squared predicted values of above 90% for all tested cases with the exception of the 5/16 in parallel heat exchangers in short and long fin configurations. Detailed examination of these cases shows, that unlike most test data, these tests had very low inlet air relative humidity values. It is then necessary to capture the increased air density for these test cases. The correlation equations were updated as shown in equations (40) and (41):

$$j = C_1 Re^{C_2} \left( \frac{D_f}{F_p} \right)^{C_3} \left( \frac{\rho_{in}}{\rho_{avg}} \right)^{C_4} \quad (40)$$

$$f = C_5 Re^{C_6} \left( \frac{D_f}{F_p} \right)^{C_7} \left( \frac{\rho_{in}}{\rho_{avg}} \right)^{C_8} \quad (41)$$

Where  $\rho_{in}$  and  $\rho_{avg}$  are density of moist air at the inlet temperature and at the average temperature respectively both with respect to the heat exchanger air inlet and outlet.

The resulting correlations were able to predict the heat transfer and pressure drop performance of the different coils as show in Table 11 and Table 12.

**Table 11: Regression summary, parallel coils**

	3/8 in, Short Fin		5/16 in, Short Fin	
	R-sq	R-sq (adj)	R-sq	R-sq (adj)
<i>j-factor</i>	98%	98%	96%	96%
<i>f-factor</i>	97%	97%	96%	96%
	3/8 in, Long Fin		5/16 in, Long Fin	
	R-sq	R-sq (adj)	R-sq	R-sq (adj)
<i>j-factor</i>	97%	97%	89%	88%
<i>f-factor</i>	98%	98%	94%	94%

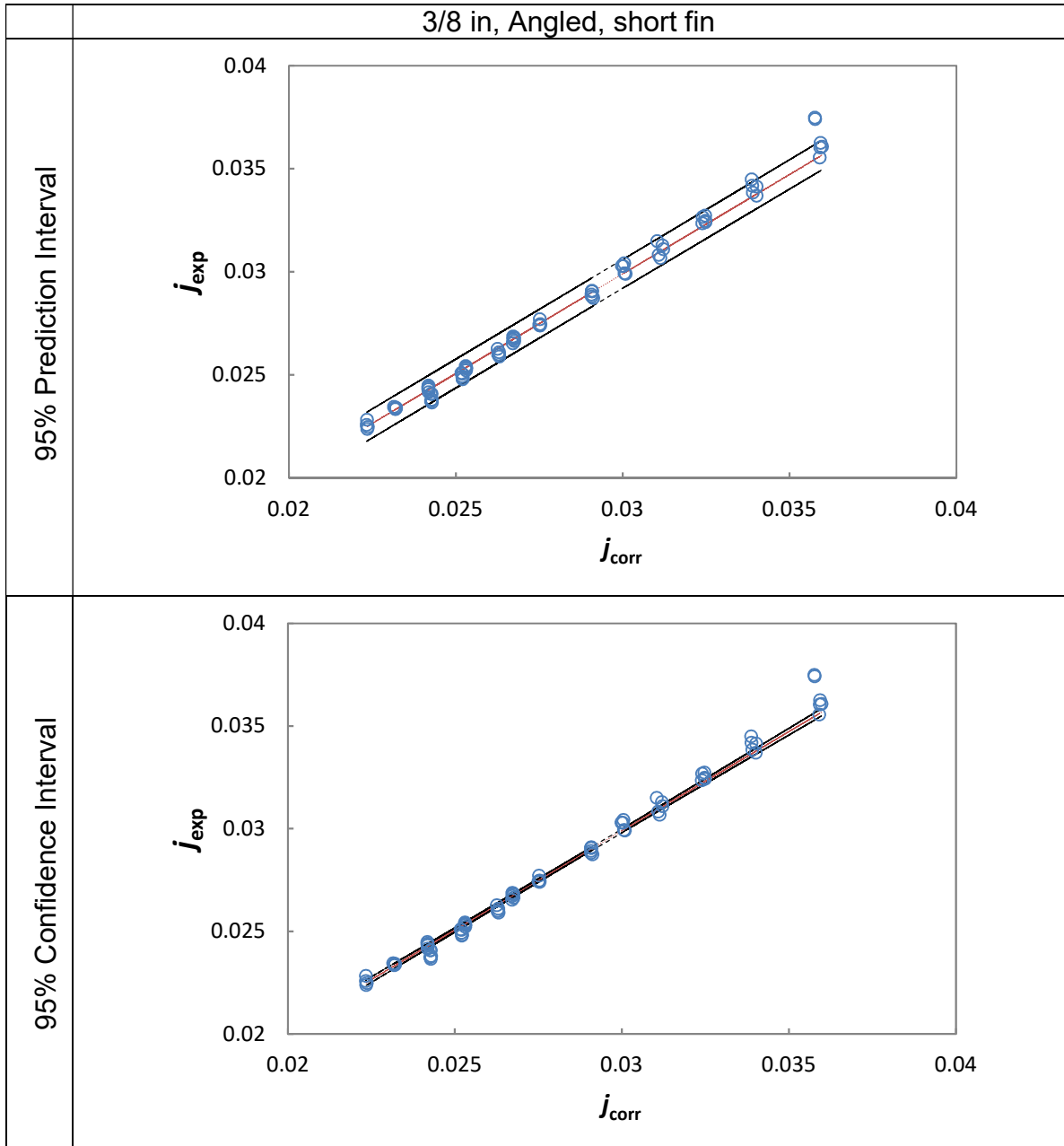
**Table 12: Regression summary, angled coils**

	3/8 in, Short Fin		5/16 in, Short Fin	
	R-sq	R-sq (adj)	R-sq	R-sq (adj)
<i>j-factor</i>	99.6%	99.5%	99%	99%
<i>f-factor</i>	99.5%	99.4%	98%	98%
	3/8 in, Long Fin		5/16 in, Long Fin	
	R-sq	R-sq (adj)	R-sq	R-sq (adj)
<i>j-factor</i>	96%	96%	99.3%	99.3%
<i>f-factor</i>	96%	96%	95%	94%

Below are plots of prediction and confidence intervals (95%) for the best and worst cases in Table 11 and Table 12.

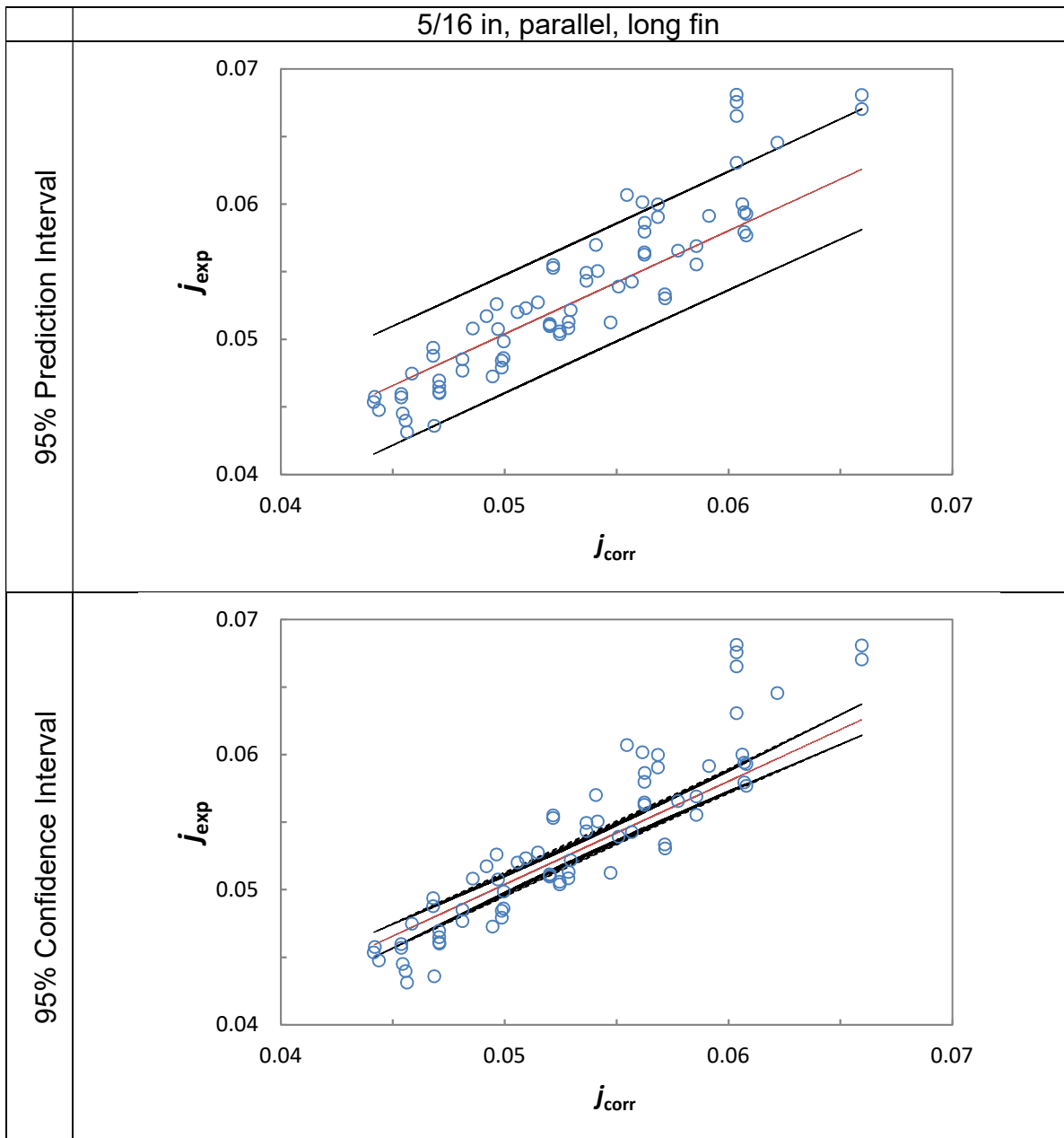
Table 13 shows the tight tolerances on both the prediction and confidence interval for the 3/8 in, angled, short fin heat exchanger.

**Table 13: Best fit, regression**



In contrast, Table 14 shows the 5/16 in, parallel configuration, long fin heat exchanger both the prediction and confidence intervals are noticeably more spread than the 3/8 in, angled, short fin heat exchanger.

**Table 14: Worst fit, regression**



## 5.1. Correlation Coefficient Summary

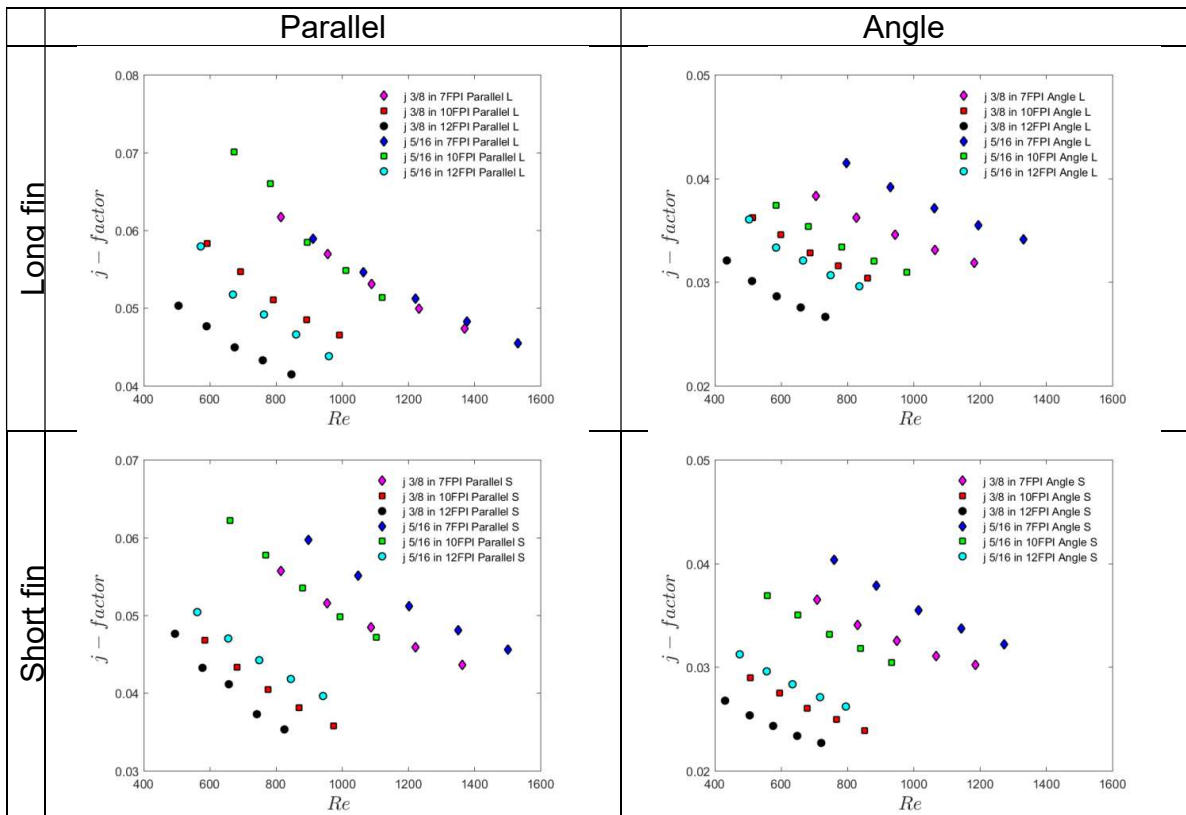
Table 15 presents a summary of the coefficients for the  $j$ -factor and  $f$ -factor correlations as specified in equations (40) and (41).

**Table 15: Coefficient summary**

Coeff.	3/8 in Parallel Short	3/8 in Angled Short	3/8 in Parallel Long	3/8 in Angled Long	5/16 in Parallel Short	5/16 in Angled Short	5/16 in Parallel Long	5/16 in Angled Long
$C_1$	0.2911	0.3705	-3.3078	-4.9873	-4.3691	-2.9801	-2.8113	0.5963
$C_2$	-0.3443	-0.3310	0.0536	0.1406	0.1529	0.0283	-0.0284	-0.4351
$C_3$	-0.7985	-0.7788	-0.7033	-0.8626	-1.0193	-0.9008	-0.7340	-0.6594
$C_4$	12.9426	1.2855	26.9867	36.0338	46.5012	29.1260	32.6594	-4.4091
$C_5$	-0.3301	-0.0748	-1.1706	-6.2558	-1.8929	-3.1231	-3.0325	3.3237
$C_6$	-0.2308	-0.3269	-0.1209	0.2404	-0.0377	-0.0536	0.0710	-0.7220
$C_7$	-0.7347	-0.7295	-0.5617	-0.8583	-0.8957	-0.5723	-0.6895	-0.4427
$C_8$	17.7805	0.8084	16.3558	40.4053	31.6868	19.5704	34.6791	-32.6720

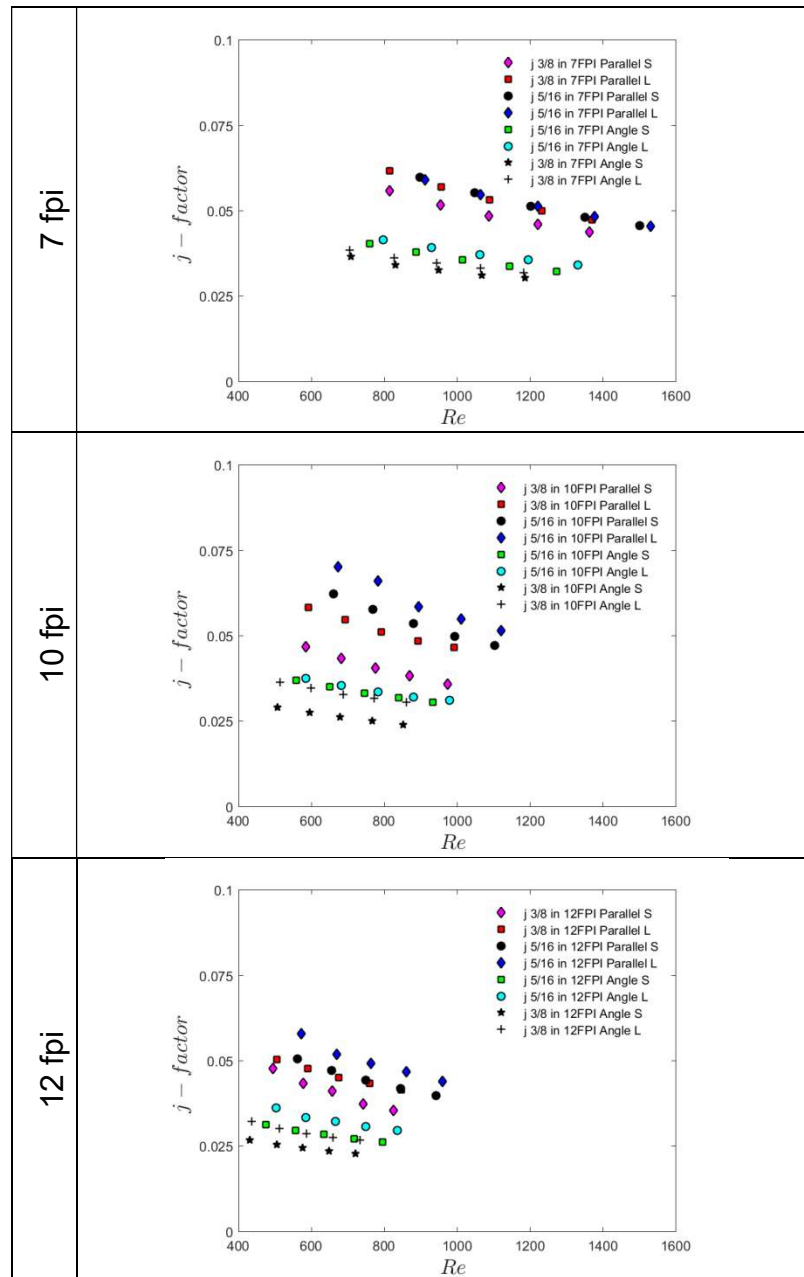
## 6. Summary

As seen in Figure 68, tube diameter has a very strong influence on the Colburn  $j$ -factor. The heat transfer performance favors the lower fin densities and the smaller tube diameter as explained in section 4.1. There is one exception on the 7 fpi, parallel, long fin configuration the performance is very close between the 5/16 in and the 3/8 in samples but still favoring the smaller tube diameter. This is not seen in any other configurations.



**Figure 68: Colburn  $j$ -factor summary based on fin length and bank orientation**

Fin length has little effect on Colburn  $j$ -factor at the lowest fin density. If there is a sample where one could claim there is some noticeable difference it would be the 7 fpi sample. However, this sample had an unusually short fin as explained previously.



**Figure 69: Colburn  $j$ -factor summary by fin density**

As seen in Figure 69, bank-to-bank angle has an impact on Colburn *j-factor* that decreases with increasing fin density. The data also shows that the 10 fpi is an ideal density with the highest heat transfer values. Fin length has an impact on Colburn *j-factor* at the 10 fpi and 12 fpi fin densities. At these densities the longer fins produce the highest heat transfer.

Based on these results one would be hard pressed to not select the 5/16 in finned tube in application. The higher thermal performance and lower cost due to material savings make it an ideal candidate. The only argument that could be made against it, would be the increase in refrigerant side pressure drop that would necessarily accompany a reduction in tube diameter. However, these small vapor compression cycles operate on very low pressure drops through the evaporator and the impact of the smaller tube diameter on pressure drop should have a manageable energy impact. An additional benefit of the smaller tube diameter is the reduction of system charge which will have a positive cost impact and in the case of organic flammable refrigerants a lower charge is an additional benefit.



## **7. Conclusions and Future Work**

### **7.1. Conclusions**

In this study the thermal and hydraulic performance of spine fin-tube heat exchangers was experimentally investigated. Unlike most other heat exchanger geometries, spine fin heat exchangers' air-side heat transfer coefficient is inversely proportional to fin density. While increases in fin density bring about an increase in air-side pressure drop, the increase in velocity does not imply an increase in AHTC. This observation agrees with data from Naess (2010). While the fins in Naess (2010) study were steel and welded to the tube, the geometry was very similar to the geometry of spine-fins used in this study. The reason for this odd behavior is attributed to excessive friction close to the tube. This friction forces an air leakage condition.

AHTC is also inversely proportional to tube diameter a condition that is also atypical in heat exchangers. Reduced leakage on the smaller tube diameters is also thought to be the reason behind this phenomenon. This is explained in detail in section 4.1.

### **7.2. Future Work**

Future work can include the upgrade of the calorimeter system to have a refrigerant instead of water as the working fluid. The addition of this capability would allow for the test to reflect real operating temperatures and as in practice in a refrigerator, little to no temperature drop across the heat exchanger (only enthalpy change). Active humidity control would also allow for frost build-up on

the heat exchanger. Thermal and pressure performance under different icing conditions would also be very valuable to the design engineer.

Due to material availability only two tube diameters were tested in the present study, it would be very valuable to include smaller tube diameters, for example 1/4 in or 7mm OD.

As presented in this work, AHTC is inversely proportional to fin density. Additional testing to find the fin density at which this trend reverses would be beneficial.

Additional samples for 5/16 in parallel configuration testing would also clarify lingering questions regarding the 7 fpi and 10 fpi shifted results.

## 8. References

- [1] M. Holtzapple, "Heat transfer and pressure drop of spined pipe in cross flow, PartII: Heat Transfer Studies," *ASHRAE Transactions*, pp. 130-135, 1990.
- [2] V. Gnielinski, "Gnielinski Single-Phase Heat Transfer Coefficient Correlation," *International Chemical Engineering*, pp. 359-368, 1976.
- [3] ASHRAE, HVAC Systems and Equipment, Atlanta: ASHRAE, 2008.
- [4] M. Kedzierski and M. Kim, "Single-Phase Heat Transfer and Pressure Drop Characteristics of an Integral-Spine-Fin Within an Annulus," U.S. Department of Commerce, Washington, DC, 1994.
- [5] T. Lee, "Comparison of air-side heat transfer coefficients of several types of evaporators of household freezer/refrigerators," International Refrigeration and Air Conditioning Conference, West Lafayette, IN, 2002.
- [6] E. Naess, "Experimental Investigation of heat transfer and pressure drop in serrated-fin tube bundles with staggered tube layouts," *Applied Thermal Engineering*, pp. 1531-1537, 2010.
- [7] L. Mooyeon, "Air-side heat transfer characteristics of spiral-type circular fin-tube heat exchangers," *International Journal of Refrigeration*, pp. 313-320, 2010.

- [8] R. Shah and D. Sekulic, Fundamentals of heat exchanger design, Hoboken: John Wiley & Sons., 2003.
- [9] D. Cooper, "About: Control Guru," 2006. [Online]. Available: <http://www.controlguru.com>. [Accessed January 2013].
- [10] G. Nellis and S. Klein, Heat Transfer, New York: Cambridge University Press, 2009.
- [11] H. Coleman and W. Glenn Steele, Experimentation, validation, and uncertainty analysis for engineers, Hoboken, NJ: John Wiley & Sons, Inc., 2009.
- [12] M. Davis, A. Jacobi and P. Hrnjak, "Evaporator Calorimeter: The Study of Overall Heat Transfer Performance," ACRC, Urbana, 1996.
- [13] W. Kays and A. London, Compact heat exchangers, Malabar: Krieger Publishing Company, 1984.
- [14] C. Wang, L. Lee, C. Chang and S. Lin, "Heat transfer and friction correlation for compact fin-and-tube heat exchangers," *International Journal of Heat and Mass Transfer*, vol. 42, no. 11, pp. 1945-1956, 1998.
- [15] ASHRAE, Standard methods for laboratory airflow measurement. ASHRAE STD41.2, Atlanta: ASHRAE, 1992.

- [16] ASHRAE, Method of testing forced circulation air cooling and air heating coils. ASHRAE STD 33, Atlanta: ASHRAE, 2001.
- [17] ANSI/AMCA/ASHRAE, "Laboratory methods of testing fans for certified aerodynamic performance rating. AMCA 210," AMCA/ASHRAE, Arlington Heights/Atlanta, 2008.
- [18] K. Kawaguchi, K. Okui, T. Asai and Y. Hasegawa, "Heat Transfer and Pressure Drop Characteristics of Finned Tube Banks in Forced Convection (Comparison of the Heat Transfer Characteristics between Spiral Fin and Serrated Fin)," *Heat Transfer - Asian Research*, 2005.
- [19] A. Rivera, "Performance of ammonia condenser plate type heat exchanger, MS Thesis.," UMD, College Park, MD, 2016.
- [20] H. Jiang, V. Aute and R. Radermacher, "CoilDesigner: a general-purpose simulation and design tool for air-to-refrigerant heat exchangers," *International Journal of Refrigeration*, vol. 29, no. 4, pp. 601-610, 2006.